

American University in Cairo

AUC Knowledge Fountain

Theses and Dissertations

Student Research

Winter 1-31-2022

Atomistic Simulation of Na⁺ and Cl⁻ Ions Binding Mechanisms to Tobermorite 14Å as a Model for Alkali Activated Cements

Ahmed Abdelkawy

The American University in Cairo AUC, ahmedabdelkawy@aucegypt.edu

Follow this and additional works at: <https://fount.aucegypt.edu/etds>



Part of the [Atomic, Molecular and Optical Physics Commons](#), [Fluid Dynamics Commons](#), [Materials Chemistry Commons](#), [Numerical Analysis and Scientific Computing Commons](#), and the [Sustainability Commons](#)

Recommended Citation

APA Citation

Abdelkawy, A. (2022). *Atomistic Simulation of Na⁺ and Cl⁻ Ions Binding Mechanisms to Tobermorite 14Å as a Model for Alkali Activated Cements* [Master's Thesis, the American University in Cairo]. AUC Knowledge Fountain.

<https://fount.aucegypt.edu/etds/1729>

MLA Citation

Abdelkawy, Ahmed. *Atomistic Simulation of Na⁺ and Cl⁻ Ions Binding Mechanisms to Tobermorite 14Å as a Model for Alkali Activated Cements*. 2022. American University in Cairo, Master's Thesis. AUC Knowledge Fountain.

<https://fount.aucegypt.edu/etds/1729>

This Master's Thesis is brought to you for free and open access by the Student Research at AUC Knowledge Fountain. It has been accepted for inclusion in Theses and Dissertations by an authorized administrator of AUC Knowledge Fountain. For more information, please contact thesisadmin@aucegypt.edu.

Atomistic Simulation of Na⁺ and Cl⁻ Ions Binding Mechanisms to Tobermorite 14Å as a Model for Alkali Activated Cements

By

Ahmed Abdelkawy

B.Sc. Materials Science and Engineering, GUC

A thesis submitted in partial fulfillment of the requirements for the degree of
Master of Science in Nanotechnology

Advisor

Dr. Mostafa Youssef

Assistant Professor of Computational Materials Science and Engineering
Department of Mechanical Engineering,
The American University in Cairo

Co-Advisor

Dr. Claire E. White

Associate Professor of Civil and Environmental Engineering
and the Andlinger Center for Energy and the Environment
Princeton University

Acknowledgments

The work was made possible by the funding from the Bartlett Family Fund from the AUC. Most of the calculations in this work are done using the Princeton Research Computing resources at Princeton University.

I would like to express my extreme gratitude to Dr. Mostafa Youssef for the help, guidance, encouragement, and support throughout the past three years to finish this work. Dr. Mostafa Youssef has been a true mentor and has guided me through this academic journey. Our discussions have been very enriching to my knowledge and research experience. I am truly grateful for all the knowledge I have acquired from you through our numerous meetings. The skill I have been taught will help me immensely during my next academic steps.

I would also like to thank Dr. Claire White for her continuous support throughout the work. The group meetings and the very enriching discussions have been very insightful to this research. Moreover, the additional allocated computational resources have been of utmost importance to accelerate the final calculations.

Finally, none of this work would have been possible without my family. Most of all, I would like to thank my parents, Abdelkawy and Rania, for their unlimited support, for their high expectations of me, and for everything they have endured so that I can get to this point. Words cannot express my gratitude. To Noha, thank you for always being there. Your unconditional support is why I was able to finally make it. To my sincere friends, Basem, Souidan, Mahmoud, and Farah, thank you very much for your support throughout the journey.

Abstract

The production of ordinary Portland cement (OPC) is responsible for ~8% of all man-made CO₂ emissions. Unfortunately, due to the continuous increase in the number of construction projects, and since virtually all projects depend on hardened cement from the hydration of OPC as the main binding material, the production of OPC is not expected to decrease. Alkali-activated cement produced from the alkaline activation of byproducts of industries, such as iron and coal industries, or processed clays represents a potential substitute for OPC. However, the interaction of the reaction products of AAC with corrosive ions from the environment, such as Cl⁻, remains largely unexamined.

In this study, we present the details of preparing undoped and 5% Na-doped tobermorite 14Å structures as molecular models for the disordered alkali-doped calcium-alumino-silicate-hydrate (C-(N)-A-S-H, where N represents sodium and A represents aluminum) structure, which is the main reaction product in Ca-rich AAC. Moreover, we examined the ability of these structures to hinder the ingress of solvated Na⁺ and Cl⁻ ions using molecular dynamics simulations. We adopted a core-shell model for these simulations to represent the polarizability of oxygen ions and a flexible model to represent water molecules. The combined interatomic interactions adopted in this work accurately predicted lattice parameters and basic mechanical properties similar to those obtained from different experimental and computational studies for the tobermorite 14Å structure. Moreover, these interactions could predict lattice parameters similar to those predicted by the ClayFF force field, a widely used force field to describe cementitious materials.

By examining the structural, energetic, and dynamic properties of interfacial water molecules and solvated Na⁺ and Cl⁻ ions, we showed that introducing Na⁺ ions as dopants to the bulk tobermorite 14Å structure had a positive impact on enhancing the adsorption of solvated Cl⁻ ions. This positive impact is twofold; first, new and stable adsorption sites have been introduced on the surface of the 5% Na-doped system because of the charge balancing mechanism taking place while substituting Ca²⁺ ions with Na⁺ ions. Second, introducing the 5% Na⁺ ions led to slower dynamics for all species in this system. The slow dynamics originated from the excess Na⁺ ions in this system, and that NaCl is a structure-making salt. These results suggest that the presence of Na in Ca-rich AAC results in more resistance to chloride-induced corrosion due to an increased ability to hinder the movement of Cl⁻ ions. In addition to the effectiveness of these types of cement to resist Cl⁻ ions diffusivity, these results from molecular-scale simulations also encourage the usage of sustainable AACs, which directly reduce the immense volume of greenhouse emissions produced annually from the OPC industry.

Table of Contents

Acknowledgments	2
Abstract	3
List of Figures	6
List of Tables	9
Chapter 1. Introduction, Background, and Objective	10
Chapter 2. Literature Review of Cementitious Materials	16
2.1. The Hydration of Ordinary Portland Cement to Produce Concrete	16
2.1.1. Ordinary Portland Cement Raw Materials and the Hydration Process	16
2.1.2. The Properties of the Calcium-Silicate-Hydrates (C-S-H) Structure.....	17
2.1.3. Confined Water Molecules in the C-S-H Structure	18
2.2. Parameters used to Build Representative Models for the Calcium-Silicate-Hydrates (C-S-H) Structure.....	19
2.2.1. Developing Descriptive Molecular Models for Computational Calculations	20
2.3. Alkali-Activated Cements (AAC).....	22
2.3.1. Developing Molecular Models for C-S-H Produced by the Formation of AACs.....	23
2.4. Computational Studies of Water and Ions Adsorption on OPC Hydration Products.....	24
2.4.1. Water characteristics at the surface of the C-S-H structure	25
2.4.2. Ions' adsorption characteristics at the surfaces of the C-S-H structure	27
2.5. Molecular Dynamics and Empirical Force fields.....	28
Chapter 3. Computational Methods	31
3.1. Molecular Model.....	31
3.1.1. Fixing Half Occupied Sites	32
3.1.2. Duplicating the structure into a (6 x 4 x 1) supercell and doping Na ⁺ ions	34
3.1.3. Distributing Interlayer Ions Upon Cleaving the (001) Surface	36
3.1.4. Hydrating the cleaved surfaces and inserting Na ⁺ and Cl ⁻ ions	40
3.2. Force Field	43
3.2.1. Core-Shell distance analysis	44
3.2.2. Force Field Parameters.....	47
3.2.3. ClayFF Parameters.....	51
3.3. Simulation Details.....	56
3.3.1. Energy Minimization at 0K.....	56
3.3.2. Finite Temperature Molecular Structure Equilibration.....	60
3.3.3. Production Simulations	64

3.4.	Postprocessing Tools	67
3.4.1.	Density profiles & Contour plots	67
3.4.2.	Adsorption Free-Energy calculations.....	68
3.4.3.	Mean Square Displacement & Diffusion Coefficient	69
3.4.4.	Velocity Autocorrelation Function (VAF) and Vibrational Density of States (VDOS)	70
3.4.4.	Residence Time Correlation Function	71
Chapter 4.	Results and Discussion.....	73
4.1.	Structural Properties.....	73
4.1.1.	Water Molecules and Solvated Ions 1-D Density Profiles.....	73
4.1.2.	2-D Contour Plots	77
4.2.	Adsorption Energetics of Solvated Na ⁺ and Cl ⁻ ions	82
4.3	Dynamic Properties.....	87
4.3.1.	Diffusion Coefficient	87
4.3.1.1.	Diffusion Coefficient of Water Molecules in Interfacial Systems	88
4.3.1.2.	Diffusion Coefficient of Water Molecules in Bulk Systems.....	91
4.3.1.2.	Diffusion Coefficient of Na ⁺ and Cl ⁻ ions.....	91
4.3.1.3.	The Effect of Doping Tobermorite 14Å with 5% Na on the System Dynamics.....	93
4.3.2.	Vibrational Density of States of Water Molecules.....	95
4.3.3.	Ions' residence time	99
Chapter 5.	Conclusions and Future Work.....	101
5.1.	Conclusions.....	101
5.1.1.	Force field Benchmarking Studies	101
5.1.2.	Characteristics of Interfacial Water Molecules.....	102
5.1.3.	Characteristics of Adsorbed Na ⁺ and Cl ⁻ Ions.....	104
5.2.	Recommendations and Future Work.....	105
References.....	108	
Appendix A: GULP Input File.....	119	
Appendix B: DLPOLY 4 Input Files.....	128	
Appendix C: C++ Code for Output Processing.....	133	

List of Figures

Figure 1. Greenhouse gas (GHG) emissions from different industries in the UK, with the cement industry contributing ~ 8% of all the man-made CO₂ emissions.³ 10

Figure 2. The structure of Calcium-Silicate-Hydrate (C-S-H) nanoclusters, originally depicted in **Reference 8**. The calcium-silicate solid layers are shown in red. Shown are also the two types of water molecules embedded between the solid layers (blues dots within the red clusters) and adsorbed at the interfaces of the solid layers in dark blue. 18

Figure 3. Fixing the half-occupied sites in the unit cell of tobermorite 14Å.³⁷ Left visualization shows a single unit cell with only Ca ions shown. Solid blue spheres represent Ca ions with full occupancy, while half-blue half-white spheres represent Ca ions with half occupancy. Also shown are the four symmetry operations of the crystal structure exemplified on the half-occupied Ca sites (Ca₂). See the text for the description of these sites. Right visualization represents two-unit cells after duplication along the a-axis. Lower and upper interlayer spaces are for the same interlayer because of the periodic boundary conditions. 33

Figure 4. (a) and (b) illustrate duplicating pristine tobermorite 2-unit cells into a 6 x 4 x 1 supercell. (c) Shows the charge balancing mechanism for replacing one Ca²⁺ ion and a whole water molecule with an Na⁺ ion, a proton that forms a hydroxyl group, and a dissociated water molecule that formed another two hydroxyl groups according to **Reference 11**. (d) 5% Na doped tobermorite 6 x 4 x 1 supercell (titled to show substituted Na⁺ ions behind Ca²⁺ ions). 35

Figure 5. In the left visualization, the original 5% Na-doped tobermorite 14Å (6 x 4 x 1) supercell before any bulk relaxation or cleaving the (001) surface. On the right, the 5% Na-doped tobermorite 14Å (6 x 4 x 1) supercell after, relaxing the bulk structure, then cleaving the (001) surface and increasing the c-axis, and distributing Ca²⁺ and Na⁺ ions that originally existed in the interlayer space on the two newly created surfaces. Solid blue spheres represent Ca ions, while solid orange spheres represent Na ions. Red and green notation represent rows of atoms originally located in the same interlayer space in the bulk structure and then shifted to be on the upper and lower created surfaces, respectively. Note that in the bulk structure (left), periodic boundary conditions set the rows R1 – R8 in the same interlayer space. 38

Figure 6. Adjusting the location of the bridging silicates hydroxyl groups and the free ones resulted from the charge balancing mechanism on the newly created (001) surfaces. The procedure depends on the location of the considered Na⁺ ion, whether on the top or bottom surfaces. Top visualization shows Na⁺ ions before surface cleavage and after positioning on the upper surface, while bottom visualization shows Na⁺ ions before surface cleavage and after positioning on the lower surface. Before cleaving, each Na⁺ ion is coordinated by 3 hydroxyl groups; 2 belonging to the bridging silicates and a free one. Upon cleaving the (001) surfaces, each Na⁺ ion becomes coordinated by two hydroxyl groups only; one free and one belonging to the bridging silicate. Solid green spheres represent Si ions, solid orange spheres represent Na ions, solid red spheres represent oxygen ions, and solid white spheres represent hydrogen ions. 39

Figure 7. Different water volumes above the surface of the undoped tobermorite 14Å (6 x 4 x 1) supercell. From left to right, shown is the visualization of 500, 1000, 1500, and 2000 water molecules. The color legend is shown on the far right. 41

Figure 8. The 1st and 2nd two visualizations represent the undoped tobermorite 14Å before and after inserting the 0.5 mol/L NaCl concentration in the 1500 interfacial water molecules. The 3rd and 4th visualizations are those for the 5% Na-doped tobermorite 14Å. The initial 2.5Å clearance left between water and the solid substrate can be seen before equilibrating the two systems in the 1st and 3rd visualizations..... 42

Figure 9. The visualizations of the final two molecular models as examined in this work. On the left visualization, shown is the undoped tobermorite 14Å + 0.5 mol/L NaCl in the pore. The right visualization shows the 5 % Na-doped tobermorite 14Å + 0.5 mol/L NaCl in the pore. The color legend is shown on the far right. 42

Figure 10. Silicates’ oxygens polarization analysis using CS model. This analysis was only done to the bulk solid undoped tobermorite 14 Å (6 x 4 x 1) supercell. (a) The normalized distribution for a given CS distance was calculated from a 2 ns MD simulation. Os D1 and Os D2 are the ranges of the two peaks of the CS distribution. (b) 2-d contour plots corresponding to the two CS distance peaks visualized in the bc-plane of tobermorite based on 2 ns simulation. (c) tobermorite bc-plane atomic visualization for the last snapshot of the 2ns simulation. Shown in the top right is the color legend for different atomic species. Arrows between (b) and (c) match the positions of the oxygen ions with smaller and larger polarization values from the contour plots and the atomic visualization. Oxygen ions with smaller polarization are those confined between two silicon ions. In comparison, those with the larger polarization are attached to one silicon ion from one side and a calcium ion from the other. 46

Figure 11. 1-D density profiles for the undoped and the 5% Na-doped interfacial systems. 1-D mass density profiles of water (red) on the left y-axes and number density profiles of Ca (blue), Na (orange) & Cl (black) on the right y-axes. Vertical dashed and dotted lines in (a) & (b) are the upper boundaries of the channel layers (represented by thick tilted black lines) and surface layers (represented by light tilted black lines), respectively. The bulk layer is represented by solid blue color..... 74

Figure 12. 2-D contours plots for the undoped and the 5% Na-doped interfacial. (a) and (b) 2-D contour plots of the lower and upper surfaces of the undoped system, respectively. (c) and (d) 2-D contour plots of the lower and upper surfaces of the 5% Na-doped system, respectively. Below the contour plots are the atomistic visualizations for different adsorption sites: AS1-6. In each plot, Ca²⁺ is represented by solid blue lines, Si⁴⁺ is represented by solid green lines, Na⁺ is represented by solid orange lines, Cl⁻ is represented by solid black lines, and H⁺ of OH is represented by solid red lines. Arrows from the atomistic visualizations to the contour plots represent the Cl⁻ ions adsorbed (thick circular black lines). (e) Natural surface pores with channel water represented by the dashed thick black lines and the effect of the charge balancing mechanism on the bridging silicates exposed to the surface and the hydrogenation of dangling oxygens are shown. (f) Color legend for different atomic species. All atomic snapshots are for the cleaved upper surface (water is below and around the shown solid species but removed for figure clarity). 79

Figure 13. Adsorption free-energy profiles for solvated Na⁺ (dash-dotted orange lines) and Cl⁻ (solid black lines) ions on the surface of the (a) undoped and (b) the 5% Na-doped systems. For illustration, the adsorption free-energy gain for Cl⁻ ions on the surface of the undoped system is the difference between the energy levels marked by red dashed arrows in (a). The desorption barrier for Cl⁻ ions on the 5% Na-doped system is the difference between the energy levels marked by blue dashed arrows in (b). For further illustration, the reader is referred back to the text in section 4.2. 83

Figure 14. (a) The diffusion coefficients of different species on the surfaces of the undoped (red x markers) and the 5% Na-doped (green x markers) systems. Error bars shown represent the standard deviation calculated from averaging the diffusion coefficient over all simulations. The diffusion coefficients of water molecules at different distances from the surface: the interlayer space (volume represented by solid black color), the channel layers (volume represented by thick and titled black lines), the surface layers (volume represented by light and tilted black lines), and the bulk layer (volume represented by solid blue color) are shown. Moreover, the diffusion coefficients of Na⁺ and Cl ions in the whole pore volume are also shown. (b) Atomistic visualization of the different examined water layers above and between the solid substrate. 88

Figure 15. Vibrational Density of States (VDOS) of water molecules, calculated from the hydrogen atoms, at different distances from the surface: a) Interlayer water layer between two solid silicate layers, b) Channel water layer that is confined from one side by surface species, c) Surface water layer at a further distance from the surface, and d) Bulk water layer, which is midway between the two surfaces. VDOS of water in the undoped system (solid red lines) and 5% Na-doped system (solid green lines). For reference, it is also showing VDOS of water in bulk solid tobermorite without any artificial interfaces (dashed black line) and in bulk water without any solid (dotted black line). 96

Figure 16. (a), (b), (c), and (d) represent the mean square displacement plots (red curves) for the interlayer water, channel water, surface water, and bulk water layers, respectively. These results are for the undoped tobermorite pore system, specifically, the 1st 4 ns production simulation, where trajectories are recorded only for the last 3 ns. Shown also straight fitted black lines used to calculate the diffusion coefficient from the Einstein equation. 143

Figure 17. (a), (b), (c), and (d) represent the mean square displacement plots (red curves) for the interlayer water, channel water, surface water, and bulk water layers, respectively. These results are for the 5% Na-doped tobermorite pore system, specifically, the 1st 4 ns production simulation, where trajectories are recorded only for the last 3 ns. Shown also straight fitted black lines used to calculate the diffusion coefficient from the Einstein equation. 144

List of Tables

Table 1. Charges and masses for cores and shells.....	48
Table 2. Species' charges and masses.....	48
Table 3. Lorentz-Berthelot combining rules. ⁹⁰	48
Table 4. Intermolecular interactions.....	49
Table 5. Intermolecular interactions - continued.....	50
Table 6. Intramolecular (bonded) interactions.....	51
Table 7. ClayFF species' charges and masses.....	52
Table 8. ClayFF intermolecular interactions ^{(a),(b)}	53
Table 9. ClayFF intermolecular interactions - Continued ^{(a),(b)}	54
Table 10. ClayFF intramolecular (bonded) interactions.....	55
Table 11. Lattice vectors for the (2 x 1 x 1) undoped tobermorite 14Å supercell compared to that reported in the original paper. ³⁷	59
Table 12. Mechanical properties obtained from GULP for the undoped tobermorite 14Å compared to that found in the literature.....	59
Table 13. undoped tobermorite 14Å lattice parameters from 3.1 ns relaxation: our combined interatomic potentials vs. ClayFF and original structure.....	63
Table 14. 5% Na doped tobermorite 14Å lattice parameters from the 3.1 ns relaxation MD: our combined interatomic potentials vs. ClayFF.....	63
Table 15. Adsorption energy gain and desorption energy barrier for solvated Na & Cl ions in both the 0% Na & 5% Na systems.....	83

Chapter 1. Introduction, Background, and Objective

The increasing concern of global warming and all the associated detrimental environmental impacts forces the scientific community to investigate the root practices behind the problem and find solutions and alternatives. Ordinary Portland Cement (OPC) production is one of these industrial practices responsible for ~8% of all human-made CO₂ emissions.^{1,2} The huge volume of cement produced annually, with all the associated emissions, is not expected to decrease because of the ever-expanding urban communities. The importance of this industry comes from the fact that hydration of OPC clinker is used to produce hardened cement, which is the basic binding material in virtually all construction projects. **Figure 1** represents the contributions of different industries to the UK CO₂ emissions.³

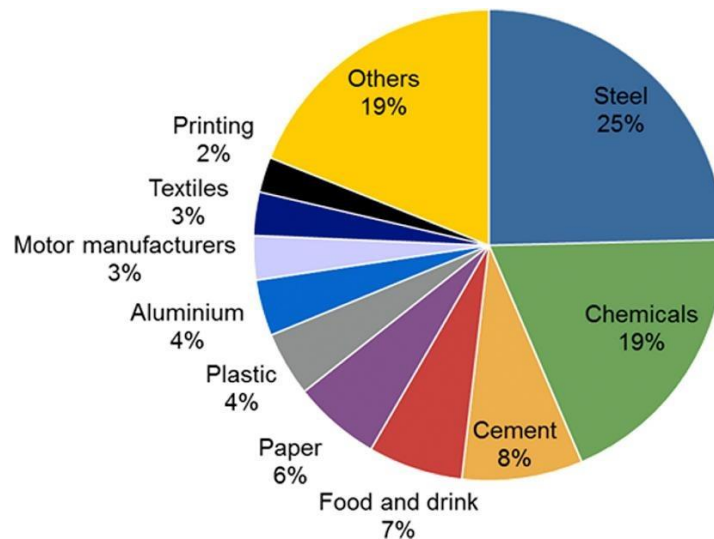


Figure 1. Greenhouse gas (GHG) emissions from different industries in the UK, with the cement industry contributing ~ 8% of all the man-made CO₂ emissions.³

One solution for this problem is by using the byproducts of other industries such as iron and coal industries to produce a new class of material known as Alkali-Activated Cements (AACs).^{4,5} Manufacturing the AACs is based on the alkaline activation (using sodium silicate (Na₂SiO₃) or sodium hydroxide (NaOH) as an activator) of the mentioned byproducts, where

calcium and aluminosilicate-rich raw materials such as blast furnace slag and fly ash are used. This process of substituting OPC with AACs cuts down the produced greenhouse emissions by around 55-80%.^{6,7} The products of the Ca-rich AACs hardened cement include a gel with a similar molecular structure, albeit with a different chemical composition compared to the hydration of the OPC. The strength-giving phases that result from the formation of Ca-rich AACs and OPC are layered, and disordered phases collectively known as Calcium-Silicate-Hydrate (C-S-H). The C-S-H is the most important phase produced because of its large volume and because it is the source of the strength and durability of the hardened cement.⁸⁻¹⁰ On the other hand, one key difference between the C-S-H produced from the hydration of OPC, and the formation of Ca-rich AACs is that in the case of the AACs, the C-S-H phase contains alkali and aluminum atoms that are found in the solid layers to produce a C-N-A-S-H structure (N and A represent Na and Al atoms, respectively). The inclusion of Na atoms is because of the alkaline activation step used in the production of AACs. The charge balancing mechanism, the thermodynamic stability, and the effect of alkaline inclusion on the physiochemical properties of the bulk C-S-H structure have been recently studied.¹¹⁻¹⁴

On the other hand, C-S-H (or C-N-A-S-H in the formation of AACs) forms a complex microstructure made of C-S-H gel particles separated with porosity filled with an aqueous solution. These pores have sizes that range from 0.5 to 10 nm and are interconnected.¹⁵ Water in these pores is the transport medium of any aggressive ions that exist in the surrounding environment. If these ions are not hindered by getting adsorbed onto the surface of the solid substrate of the solid hydration products, they will diffuse deep into the structure. If these ions arrive at the reinforcing steel bars, in the case of concrete structures, they will accelerate the corrosion process. In that case, these ions will compromise the structural integrity and safety of these construction projects. This

danger is specifically more prominent in chloride-rich environments, such as coastal regions and near to seashores. Therefore, it is important to understand, on an atomistic level, the physiochemical interactions of these ions with water and with the solid surfaces of C-N-A-S-H in ultra-confined environments mimicking the gel pores.

Researchers have been able to use experimental techniques to deduce basic and important properties of the solid C-S-H structure such as the density,⁸ the Ca/Si (C/S) ratio,¹⁰ and the characteristic length of the silicate chains (Q^2 silicate tetrahedra) and their decomposition into smaller groups (Q^1 and Q^0) for the case of increasing the alkaline concentration to mimic the alkaline activators.^{16,17} Moreover, scientists have calculated the characteristic Ca-O and Si-O coordination number and bond lengths in different environments.¹⁸ These properties were used to build more accurate representative molecular models of the true C-S-H structure, which are widely used in computational studies.¹⁹ However, traditional experimental techniques are very tedious, require complex preparation, and cannot easily probe the nature of ion capture and ion exchange processes that happen very rapidly (on the order of picoseconds) on a very small and localized (atomistic) length scale during the adsorption process. With the continuously growing computational power, numerical-based methods, such as Molecular Dynamics (MD), represent a powerful tool complementary to the traditional experiments. MD offers detailed insight into the atomic trajectories for the examined time span, enabling a very elaborate inspection of the surface adsorption process.

Multiple researchers examined the effect of different hydration products of OPC, such as crystalline analogs for the C-S-H²⁰⁻²⁹ structure, portlandite, ettringite, Friedel's salt, and calcium aluminate mono (AFm) and trisulfate (AFt) hydrates^{20,27,30-33} on the adsorption characteristics of solvated ions near the interface. For the C-S-H disordered structure, researchers use tobermorite

9Å,³⁴ 11Å,^{35,36} and 14Å,³⁷ clinotobermorite,³⁸ and jennite³⁹ as their molecular models to computationally study the adsorption properties near the surface of C-S-H nanoclusters. The three types of tobermorite differ based on the degree of hydration and, subsequently, the separation between the solid calcium-silicate layers. The difference between tobermorite and clinotobermorite is that the silicate layers are crosslinked in the direction perpendicular to the separation between the solid calcium-silicate layers in the case of the clinotobermorite. On the other hand, all 3 tobermorite structures have a lower C/S ratio than jennite.

Moreover, researchers studied the adsorption of Cl⁻ ions specifically on pristine^{20-22,25,27} and structurally defective tobermorite surfaces.^{23,29} In these studies, all C-S-H representatives that are mentioned earlier show a low binding capacity to the solvated Cl⁻ ions on their surfaces. This low binding capacity is because these structures have an overall negative charge on their surfaces, coming from the outermost oxygen ions attached to the outermost bridging silicates. However, Zhou et al.²³ and Liu et al.²⁹ not only studied the effect of pristine molecular models but also studied the effect of changing the C/S ratio of the tobermorite 11Å substrate on the adsorption of solvated Cl⁻ ions. They both concluded that increasing the C/S ratio (by removing silicate tetrahedra from the infinite silicate chains) positively impacted the chloride adsorption capability of these solid substrates by increasing the available adsorption sites on the surface (Ca²⁺ ions). These types of studies introduced the potential and the motivation to examine further the effect of chemically and structurally modifying solid substrates, which are representative of cement hydration products, on the adsorption of aggressive ions such as Cl⁻. By this, we can introduce molecular models that are structurally and chemically more representative of the true nature of the disordered C-S-H structure. Moreover, we can also investigate the effect of introducing dopants to develop or enhance specific properties.

In this work, we study the effect of substituting interlayer Ca^{2+} ions by Na^+ ions versus pristine tobermorite 14Å on the adsorption characteristics of solvated Na^+ and Cl^- ions. We also examine the structural, energetic, and dynamic properties of solvated ions and water molecules near the interface. The choice of tobermorite 14Å as our representative molecular model is based on the fact it has a similar C/S ratio to the C-N-A-S-H structure from the activation of the ground granulated blast furnace slag.⁴⁰⁻⁴² Note that aluminum has been excluded from this study to examine and isolate the influence of sodium on the sorption characteristics of C-S-H. Thus, future work building on this thesis should focus on determining aluminum's role in this process.

This work shows that introducing Na^+ ions as a dopant in the pristine tobermorite 14Å increased its surface binding capacity and affinity to adsorb solvated Cl^- ions. This improved ability to hinder the ingress of the aggressive ions is mainly attributed to the newly introduced and energetically stable adsorption sites for Cl^- ions on the Na-doped tobermorite surface. In addition to this, we show that doping bulk solid tobermorite 14Å with 5% Na^+ ions slowed down the overall dynamics for both the water molecules and the solvated ions (Na^+ and Cl^-) in the 45Å pore. This induced cage-like effect by the introduced sodium ions originates from the structure-making effect from the extra Na^+ ions.^{43,44} Additionally, in the two systems: pristine and Na-modified tobermorite 14Å, we show that the strength of the hydrogen bond network among water molecules is enhanced as we move closer to the surface. This is known as the hard wall effect and has already been discussed in previous works.^{21,45}

The upcoming sections are classified as follows: in the literature review section, we first introduce the C-S-H structure, its properties, and the previous work done to build its representative molecular models. We also briefly present studies that examined the physiochemical interactions between these representatives with the interfacial water and solvated ions. Secondly, in the

methods section, we first describe the procedures used to build the molecular model and the charge balancing mechanism used to substitute calcium with sodium. We then describe the force field used to represent the different interatomic interactions. We also discuss the simulations' protocol used in the benchmarking studies done to test the accuracy of the force field and the molecular model used. This is followed by explaining the postprocessing tool used in the analysis of the simulations. Finally, in the results and discussion section, we discuss structural, energetic, and dynamic properties of water and solvated Na^+ and Cl^- ions at different distances from the interfaces using spatial and time correlation functions. This is then followed by the concluding remarks.

Chapter 2. Literature Review of Cementitious Materials

2.1. The Hydration of Ordinary Portland Cement to Produce Concrete

Hardened cement is a continuous, solid, and porous structure produced from the hydration of Ordinary Portland Cement (OPC). If sand and gravel are introduced to the mixture during hydration, the resultant is the well-known concrete structure. Concrete is the main material used in most construction projects, and its function is to bind, support, isolate and protect the embedded reinforcing steel bars when they exist in these projects. These bars are the backbone and the support of the entire structure carrying most of the applied tensile stresses, which is because concrete has an excellent compression strength and relatively weak tensile one. Therefore, maintaining the structural integrity of the bars and protecting them from corrosion caused by surrounding aggressing ions is of utmost importance.

On the other hand, concrete can be classified based on the reactivity of its constituents into the inert sand and gravel and the more chemically active hydration products. These products undergo continuous chemical reactions that can either be very fast and last a few minutes or very slow and persist for several years. The final products of these reactions discussed earlier in the introduction section are responsible for the physiochemical interactions with any ions or molecules from the surrounding environment. Therefore, one function of these hydration products is to protect the embedded steel bars.

2.1.1. Ordinary Portland Cement Raw Materials and the Hydration Process

Depending on the final application and the initial raw materials used to produce it, cement can be of different types. The most widely used cement is the Ordinary Portland Cement (OPC), and its production is a two-step process. The first step is to produce the cement clinker, composed

of four main phases: alite, belite, calcium aluminate, and an iron-containing phase.⁴⁶ This is done by mixing and heating a CaO source, which is limestone (CaCO_3), with an aluminum silicates source, which is usually clay. This clinker is then ground and mixed with gypsum ($\text{CaSO}_4 \cdot 2\text{H}_2\text{O}$) in a second step to produce OPC. The calcium oxide in the cement clinker phases is obtained from the thermal decomposition of limestone (CaCO_3) in a very energy-demanding chemical reaction.⁴ In addition to the chemical composition of the raw materials used to produce OPC, the usage of supplementary materials such as iron slag and fly ash, the reaction temperature (known as curing temperature), and the percentage of water used in the reaction also dictate the nature of the hydration products.⁴⁷

2.1.2. The Properties of the Calcium-Silicate-Hydrates (C-S-H) Structure

The C-S-H structure, which is shown in **Figure 2**,⁸ is a highly disordered and repeated layered structure of CaO (C), SiO_2 (S), and water (H) and constitutes more than 50% of the OPC hydration products.²⁷ In addition to this, calcium ions are embedded between the solid layers. Hydroxyl groups also exist at the interface between the silicate chains and the water molecules. These silicate chains in the C-S-H structure are made of finite repeating units of silicate tetrahedra known as dreierketten structure. These repeating units are composed of two silicate tetrahedra, known as the pair tetrahedra, followed by a third tetrahedron protruding to the interlayer region known as the bridging tetrahedron.

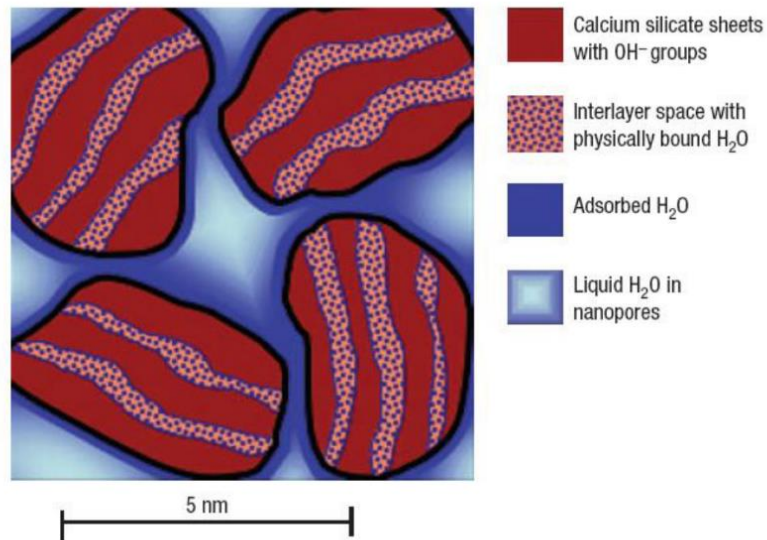


Figure 2. The structure of Calcium-Silicate-Hydrate (C-S-H) nanoclusters, originally depicted in **Reference 8**. The calcium-silicate solid layers are shown in red. Shown are also the two types of water molecules embedded between the solid layers (blue dots within the red clusters) and adsorbed at the interfaces of the solid layers in dark blue.

On the other hand, another important property used to characterize the structure of the calcium silicate layers is the calcium-to-silicon ratio (C/S), equal to 1.7 in standard OPC concrete.^{8,19} For example, the increase in the C/S ratio can change the structure of the nanoclusters and increase the degree of depolymerization of the silicate chains.^{19,48} The C/S ratio also depends on the water content used in the hydration process, also known as the water to cement ratio (W/C).¹⁰ Finally, the density of the C-S-H clusters was also calculated to be equal to 2.604 g/cm³.⁸

2.1.3. Confined Water Molecules in the C-S-H Structure

On the other hand, Water constitutes an important component in the C-S-H structure since it is responsible for the transport of various ions, including aggressive ones from the surrounding environment, through the hardened cement porous network. Water exists within and around the C-S-H clusters, forming a larger and interconnected porous network known as the gel pore network.

The former type of water is ultra-confined between the solid layers in very narrow channels whose thicknesses are in the range of a few angstroms. The dynamics of this glass-like water are very slow because of the hydrophilicity of the surrounding calcium silicate substrate and the strong hydrogen bond network that is developed between them.⁴⁵ On the other hand, water between separate C-S-H clusters is allowed to move faster because of the relatively bigger pores, in the order of a few nanometers, and the relatively weaker hydrogen bond network.

2.2. Parameters used to Build Representative Models for the Calcium-Silicate-Hydrates (C-S-H) Structure

As mentioned in the introduction section, even though the structure of the true C-S-H is very complex, it can be described in terms of the nearest nature crystalline analogs: tobermorite 9Å,³⁴ 11Å,^{35,36} and 14Å,³⁷ clinotobermorite,³⁸ and jennite.³⁹ The main difference between these crystalline rare minerals and the true C-S-H structure is that the silicate chains in these structures are infinite, while they are finite in the more defected C-S-H clusters. In addition to this, the C/S ratios of these structures are well below the true C/S ratio of C-S-H. Moreover, and in addition to the length of the silicate chains and the C/S ratio, there are additional parameters to be considered when building a molecular model representative to the true C-S-H structure, such as the concentration of Si-OH and Ca-OH groups in the solid structure, the Ca-O coordination number, and the interlayer distance separating between the solid layers.⁴⁹

Experimental results show that according to the distribution of hydroxyl groups, the true C-S-H structure is similar to the mineral jennite, where hydroxyl groups are almost entirely attached to Ca ions and not to Si ions as in the case of Tobermorite.^{50,51} However, according to the structural properties probed by XRD analysis and Raman spectroscopy, C-S-H is more similar to the Tobermorite mineral.^{52,53} Moreover, experiments show that the Ca-O coordination number is

dependent on the C/S ratio; as such, it decreases from 7.1 to 6 as the C/S ratio increases from 0.6 to 1.75.¹⁸ Finally, the interlayer distance in C-S-H clusters is measured to be around 11-12 Å. For the three tobermorite structures, the interlayer spacing is categorized based on the degree of hydration into 9 Å (least hydrated), 11 Å, and 14 Å (most hydrated).³⁴⁻³⁷ All these parameters must be properly considered while developing a descriptive atomistic model representing and reproducing the true physiochemical characteristics of the C-S-H nanoclusters.

2.2.1. Developing Descriptive Molecular Models for Computational Calculations

Guided by all the previously mentioned structural and chemical characteristics of the true C-S-H structure, researchers modified the crystalline analogs to develop molecular models that can be used in their computational calculations. Firstly, Pellenq et al. started from Hamid's version of the tobermorite 11 Å³⁵ and randomly removed the silicate groups from the structure to increase the C/S ratio to 1.65, which is almost identical to the true value (1.7) of the C-S-H.⁵⁴ However, the resultant structure was free from any OH groups as they were intentionally removed. The existence of OH groups is an important feature in the true C-S-H structure. Moreover, this model failed to reproduce the actual Ca-O distance and the actual density of C-S-H clusters (2.34 g/cm³ vs. the true 2.6 g/cm³). It also predicted the existence of Q⁰ (isolated monomers) groups, which are not found in the true C-S-H samples.

In a later work, Abdolhosseini Qomi et al. tried to fix these limitations using the ReaxFF force field to dissociate water molecules into OH⁻ and H⁺ ions.⁹ These dissociated ions are then free to bind to any of the surface species. The ReaxFF force field enables chemical reactions to spontaneously take place, which enables the dissociation and the creating of different chemical bonds.⁵⁵ However, the produced H⁺ ions were bonded to Si-O groups and formed Si-OH groups instead of forming the desired Ca-OH. Si-OH groups are very scarce in true C-S-H clusters.^{48,51}

On the other hand, Kovačević et al. worked on developing a molecular model for the C-S-H structure starting from Merlino's version of the tobermorite 11Å.^{19,36} To increase the C/S ratio of the structure, they modified the tobermorite 11Å using three different approaches. The first approach is removing the bridging silicate tetrahedra and the addition of Ca²⁺ ions, which are then charge-balanced by additional OH⁻ groups. The second approach they adopted is the removal of both the connected bridging and pair silicate tetrahedra. Finally, their third approach was a random removal of the silicate groups. Out of these three approaches, the authors concluded that the first model was the most energetically stable. They also emphasized that the approach of building the molecular model has a great influence on the energy and the characteristics of the C-S-H model structure. They were also able to compute a density (2.42 g/cm³) more similar to the true density of the C-S-H structure (2.6 g/cm³).

Finally, Mohamed et al.⁴⁹ developed a more detailed bottom-up approach to build a realistic C-S-H structure from basic building blocks based on the Tobermorite 14Å.³⁷ While this promising model could reproduce the low Si-OH concentration mentioned earlier and the realistic silicate chain length that agree with the experiment, lower water content and larger interlayer separation were observed.

In conclusion, building a molecular model that agrees with different observations from experiments is not an easy task. This difficulty is mainly attributed to the absence of long-range order and the variable stoichiometry within the same C-S-H cluster. It is also because of the multivariable nature of producing C-S-H structures in terms of the chemical composition of the raw material, the degree of hydration, and the reaction temperature.

2.3. Alkali-Activated Cements (AAC)

As mentioned earlier in the introduction section, the step of CaO production from the limestone (CaCO_3), shown in **Equation 1**, to produce OPC results in an immense volume of greenhouse emissions. These emissions are either produced directly from the chemical reaction or indirectly in the tremendous heat energy required (around $1400\text{-}1500^\circ\text{C}$) to initiate this reaction and form the alite phase, usually obtained from burning fossil fuels.⁵⁶ Since the cement industry is the enabling technology for all structural projects, the amount of CO_2 emissions produced annually is also gigantic because every ton produced from cement is responsible for the emission of one ton of CO_2 .^{4,5} The already existing environmental crisis of global warming is the motive behind the extensive research being done in the field of cementitious materials to find green alternatives to the well-established cement industry.



Equation 1. The decomposition of CaCO_3 at high temperature to produce CaO and CO_2 gas

Researchers are considering other alternatives for cement production to minimize and eliminate these immense harmful emissions. As introduced earlier, researchers have chemically modified the byproducts of other industries (iron and coal) to produce AACs.^{4,5} The cement produced from the alkaline activation of iron slag or the byproducts of the coal industry are known as alkali-activated slag and fly ash cement, respectively. The choice of these particular industries is based on the similarity, especially for the high-Ca sources such as iron slag, between the chemical composition of their byproducts and the raw materials used to manufacture OPC. The calcium-silicate hydrate (C-S-H) structure produced from the formation of high-Ca alkali-activated cement (AAC) is chemically similar to the C-S-H obtained from OPC hydration.

However, it has a lower C/S ratio.^{40,57} Moreover, in the C-S-H structure produced from the formation of AACs, Na⁺ ions can replace some of the Ca²⁺ ions in the interlayer region, and tetrahedral Al³⁺ ions exist in the bridging sites of the C-S-H layers.⁴ The source of these Na⁺ ions is the alkaline activators, which are usually NaOH or water glass (SiO₂ and Na₂O or SiO₂ and K₂O). The substitution of the Ca²⁺ ions also explains the lower Ca/Si ratio of the C-S-H structure produced from the hydration of AACs.

This methodology of using AACs looks very promising because it eliminates a huge volume of the produced emissions and makes the best use of the waste of other industries. The major emissions associated with AACs are produced from the manufacturing of the alkaline activators. However, to use these relatively new materials as a reliable alternative for OPC and their reaction products as the main binding and structural materials, work must be done to understand and assess their physical and chemical properties thoroughly. Moreover, it is also crucial to determine the performance and durability of these products in aggressive environments, such as in coastal areas, where corrosive ions might exist in abundance.

2.3.1. Developing Molecular Models for C-S-H Produced by the Formation of AACs

Developing molecular models representing the reaction products of AACs is more complex than building representative models for the C-S-H produced from the hydration of OPC. This is because of the additional variables introduced from the more complex raw materials and alkaline activators. Özçelik and White studied the stability of replacing interlayer Ca²⁺ ions with alkaline substitutes (K⁺ and Na⁺) and replacing the bridging silicates with aluminum in the tobermorite 14Å molecular model.^{11,37} They concluded that the most energetically favorable systems are the tobermorite 14Å with the Na⁺ and Al³⁺ ions substitution along with the introduction of two H⁺ ions

for charge balancing, followed by the pristine tobermorite 14Å. The least two energetically favorable systems were the Na-modified and the K-modified tobermorite 14Å. The methodology of Özçelik and White and their molecular model are described in the methods section.

Moreover, Özçelik et al. studied the effect of increasing Na⁺ ions concentration in clinotobermorite as their molecular model.^{12,38} they noticed a monotonic decrease in the basal spacing, both computationally and experimentally, with the increase of Na/Ca percentage. They attributed this to the lower diffusion barrier the Na⁺ ions have compared to the high diffusion barrier of the original Ca²⁺ ions. This enables sodium to diffuse more freely and to adjust into more favorable locations inside the solid structure.

2.4. Computational Studies of Water and Ions Adsorption on OPC Hydration Products

Previous subsections discussed the bulk properties of the calcium-silicate-hydrate structure C-S-H either experimentally or computationally using one of its crystalline analogs. It is also important to study the properties of water and solvated ions at the interface of the hydration products of OPC, including the individual C-S-H cluster, in the interconnected porous network. The difference between water in these larger pores and water between the solid layers of the C-S-H is that these larger pores allow for relatively faster diffusion of ions and water. These relatively faster ions' dynamics will allow for the transport of any ions from the surrounding environment deep into the structure of the hardened cement. Therefore, corrosive ions such as Cl⁻ and SO₄⁻ must be adsorbed on the solid surface of the network not to compromise the safety and the integrity of the structure. The parameters that control the diffusion and adsorption of ions at the interface of OPC hydration products are the pore size, the strength of the hydrogen bond network of the interfacial water, the ion type and concentration, and the structural and the chemical properties of the solid surface.

The adsorption mechanisms of ions on a surface can be categorized based on whether they are directly adsorbed on one of the surface species or are separated from the surface by multiple water molecules, where they are only associated because of the long-range electrostatics between them. The former type is known as Contact Ion Pair (CIP), while the latter is known as solvent separated ions pair (SSIP). Moreover, adsorption can be classified based on the bonding between the solvated ions and a surface. For example, if the adsorbed ions, which are known as adsorbates, are chemically bonded to the surface, which is known as adsorbent, this is known as chemisorption. However, if the adsorption mechanism is based only on the physical interactions, such as hydrogen bonding, this is known as physisorption.

Computationally, it is an elaborate task to model chemisorption because it requires expensive first principal ab initio calculations or classical modeling that allows for the breakage and the formation of bonds. Moreover, ions' diffusion and adsorption require a relatively long time to occur, which is in the order of nanoseconds and is beyond the available computational power. Classical molecular dynamics simulations (MD), on the other hand, represent an approximation and a compromise to model physisorption for multiple nanoseconds already using available computational resources. In the next two subsections, we first review the computational and experimental results describing water molecules near the interface of the C-S-H structure. Then we describe the properties of different solvated ions at the interface.

2.4.1. Water characteristics at the surface of the C-S-H structure

To understand the adsorption mechanism and the behavior of solvated ions, it is important first to understand the structural and dynamic properties of its surrounding medium, which is water molecules. In contrast to the ultra-confined water molecules in the interlayer region of C-S-H clusters,⁴⁵ larger pores allow for the gradual evolution of water properties from that directly at the

interface to bulk-like water properties away from the surface. The extent of the surface effect on the water molecules depends on the size of the pore.

Moreover, and as mentioned earlier, the chemistry and the structure of the solid surface dictate the properties of water near the solid surface. For example, if hydrogen donors and acceptors dominate the solid surface of the C-S-H structure, this will enhance the hydrogen bond network formed between the solid species water molecules. A stronger hydrogen bond network near the surface will decrease the diffusion of water and any ions in this region.⁵⁸ Moreover, this hydrophilic surface will affect properties such as the dielectric constant of water, making it more anisotropic.⁵⁹⁻⁶¹ This directionality of water properties is based on whether water molecules can rotate freely in some directions (parallel to the surface) while being constrained in others (perpendicular to the surface).^{59,60}

The hydrophilic surface of tobermorite 11Å changed water properties up to 10-15Å from the surface into a denser and ordered water structure, decreasing the diffusion coefficient of water molecules near the surface.²² Moreover, Kalinichev et al.²¹ also found this decrease in the diffusion coefficient of water from 6×10^{-6} cm²/s above the interface to 5×10^{-7} cm²/s deep in the silicate channels of the tobermorite 9Å. Regarding experimental calculations, Bordallo et al.⁶² calculated the diffusion coefficient of water using quasi-elastic neutron scattering (QENS) to be around 10^{-6} cm²/s for the more bound gel pore water and around 10^{-5} cm²/s for the unbound water molecules in larger pores.

On the other hand, the absence of the mentioned donors and acceptors creates a more hydrophobic surface. This hydrophobicity will shift most of the hydrogen bonds to be predominantly concentrated among the water molecules, resulting in the directionality of water

properties and slowing down the different species' dynamics. However, this is different from slow dynamics resulting at the hydrophilic surfaces due to the strong hydrogen bond network formed between water and the solid surface.^{63,64}

2.4.2. Ions' adsorption characteristics at the surfaces of the C-S-H structure

This section presents the literature that examines the adsorption characteristics of solvated ions on the surface of the C-S-H structure. Experimentally, Yoon et al.⁶⁵ studied the adsorption of Na⁺ and Cl⁻ ions on the surface of the C-S-H structure. Using X-ray diffraction (XRD), scanning transmission X-ray microscopy (STXM), and X-ray absorption near edge structure (XANES), It was noticed that Na⁺ ions prefer to get adsorbed into C-S-H samples with a lower C/S ratio (0.66), where there is an overall negative residual charge. Moreover, it was found that these samples (with a lower C/S ratio) tend to get depolymerized more because of the interaction with the Na⁺ ions. On the other hand, It was discovered that Cl⁻ ions tend to get adsorbed into C-S-H samples with a higher ratio (1.6), with an overall positive charge.

For the computational calculations using MD simulations, the group of Hou et al. did extensive research on the interfacial characteristics of the crystalline representatives of the true C-S-H structure such the tobermorite 11Å,^{22,23,25} ettringite crystal structure,³¹ and the tri-calcium silicate structure.³³ For the tobermorite 11Å, they studied the effect of increasing the solid substrate's C/S ratio (from 0.66 to 1.5) on the adsorption mechanism of Cl⁻ ions.²³ They concluded that the increase in the C/S ratio improves the adsorption of Cl⁻ ions for two reasons: firstly, this increase provides more Ca²⁺ ions on the surface, which directly attracts more Cl⁻ ions. Secondly, the increase in the C/S ratio results in more defective silicate chains, which exposes more oxygen ions. These exposed negative ions will attract more Ca²⁺ ions, which will then attract more Cl⁻ ions.

In another work, researchers studied the influence of different solvated cations (Na^+ , K^+ , and Cs^+) on the adsorption mechanism of solvated Cl^- ions.²⁵ They found that the cations can form two types of adsorption. Firstly, a strong and stable CIP adsorption (inner-sphere adsorption as described in the paper), where ions are directly bonded to the oxygens of the bridging and pair tetrahedra. The second type of adsorption is the less stable and weaker SSIP adsorption (outer-sphere adsorption as described in the paper), where the cations are separated from the oxygens of the bridging tetrahedra by water molecules.

Moreover, they also examined the size effect of the adsorbed cations on their adsorption characteristics. They deduced that the smaller the atomic size of the cation, the stronger and more stable their adsorption (Na^+ ions are strongly adsorbed while Cs^+ ions are weakly adsorbed). They attributed this to the better ability of the smaller cations to diffuse into more energetically stable adsorption sites. Finally, they describe the surface of the tobermorite 11Å as an overall negatively charged surface because of the abundant oxygen ions on the surface that are bonded to the bridging and pair silicates tetrahedra. They also found that Cl^- ions have a low binding capacity to the surface of the tobermorite 11Å because of the repulsion from this overall negative charge on the surface. This low binding capacity of solvated Cl^- ions to the tobermorite structures have also been observed by other researchers.^{21,27}

2.5. Molecular Dynamics and Empirical Force fields

Classical MD simulations utilize empirical models to describe the energy landscape and Van Der Waals interactions between different examined species. This classical representation allows MD to simulate bigger systems for longer times (hundreds of nanoseconds) than those examined using DFT calculations. For adsorption studies specifically, MD calculations accurately described the different controlling parameters that influence the adsorption phenomena.^{21,25,49}

Rigid partial charge models such as ClayFF force field⁶⁶ and the CSH-FF force field⁶⁷ have been widely used in the computational studies of cementitious materials. However, the values of these partial charges are fitted using DFT calculations based on bulk solid materials. The shortcomings of this representation to model interfaces will be discussed thoroughly in the Core-Shell (CS) analysis in the methods section.

By employing classical MD, Galmarini examined different bulk solid and interfacial structures using the ClayFF force field.⁶⁸ For the solid structures, an overestimated structural flexibility and an underestimated lattice energy were noted. These led to an inaccurate description of the bulk solid surface cleavage energies. Moreover, the study emphasized that the fitted partial charges of the examined ions are parametrized for bulk solid and bulk liquid separately. However, charges for ions at the interface between the two phases are somewhere between these two values. Moreover, the researchers also criticized the water model implement in the core-shell model by Lewis and Catlow.⁶⁹ This is because this water model predicts larger bulk liquid density and overestimates the structural stability of the water molecules.

Finally, a modified version of the core-shell force field was used in this study.⁶⁸ Specifically, the rigid water model TIP4P/2005 was implemented,⁷⁰ and the shells were removed from the anions. While this water model is excellent in predicting bulk water properties, this rigidity is expected to be very artificial when simulating interfaces because of the less conformational degrees of freedom. Moreover, removing the polarizability from the oxygen ions resulted in an artificial straightening to the Si-O-Si angle. In this work, we utilize the original core-shell model to represent the anions. Moreover, we use a flexible water model for a better description of the interactions between water molecules and solid species at the interface.^{71,72} More details about the force field used in this work are discussed in detail in the methods section.

In addition to the traditional MD and the more expensive DFT calculations, MD simulations based on machine learning potential (MLP) represent a promising and powerful tool to compute properties with a DFT calculation accuracy. In a recent study, MD simulations based on MLPs calculated lattice parameters and reproduced basic mechanical properties for different tobermorite structures with very high accuracy.⁷³ However, these types of calculations have the advantage and the ability to expand the examined systems' sizes beyond MD capabilities.

Chapter 3. Computational Methods

In section 3.1., we describe in detail the work done to build the molecular model used to represent the C-S-H structure. A full description then follows this for doping the solid structure with the Na^+ ions and cleaving the surface to create the interfacial structures. This section is followed by a detailed description of the adopted force field used to describe interatomic interactions between the different species in section 3.2. Moreover, we present the different benchmarking studies used to validate the adopted force field and the simulation details in this study in section 3.3. Finally, in section 3.4., we described the statistical mechanics methods used in the postprocessing analysis for the simulations that were run.

3.1. Molecular Model

The main reaction product for either the Ordinary Portland Cement (OPC) or the alkali-activated slag is the layered and disordered C-S-H-type structure: $\text{CaO} - \text{SiO}_2 - \text{H}_2\text{O}$. The nearest crystalline analog to the C-S-H structure used extensively in different theoretical studies is a rare mineral known as tobermorite. This mineral exists in 3 different types depending on the degree of spacing between the solid layers: Tobermorite 9Å, Tobermorite 11Å, and Tobermorite 14Å. This characteristic length is known as basal spacing, and it is the separation between the repeated calcium layers. The main difference between the crystalline tobermorite and the true C-S-H structure is that the length of the silicate chains is infinite in tobermorite and finite in length in C-S-H.^{74,75} The length of silicate chains in the true C-S-H depends on multiple factors such as the raw materials and curing temperature.^{76,77} In this study, we started from the tobermorite 14Å, with the chemical formula $\text{Ca}_5\text{Si}_6\text{O}_{16}(\text{OH})_2 \cdot 7\text{H}_2\text{O}$,³⁷ as a representative molecular model for the C-S-H structure. The choice of this specific tobermorite is based on the fact it has a C/S ratio of

0.83, which is near to the C/S ratio (0.9-1.0) of the C-N-A-S-H structure obtained from the hydration of alkali-activated blast furnace slag using NaOH or water glass.⁴⁰⁻⁴²

In the next 4 subsections, and to build the molecular model used in this study, we present the steps of eliminating half-occupied sites in the original unit cell. We then describe the procedure of duplicating and cleaving the structure in the (001) direction. Moreover, we also discuss doping the bulk solid tobermorite with 5% Na⁺ ions and the charge balancing mechanism done due to replacing Ca²⁺ ions with Na⁺ ions. Finally, we show the steps of building and hydrating the final interfacial structure.

3.1.1. Fixing Half Occupied Sites

The starting unit cell obtained from the crystallography database³⁷ contains twice the chemical formula mentioned above. In addition to this, some ions have an occupancy of one while others have an occupancy of half. For example, using the same notation used in the original paper³⁷ of the tobermorite 14Å and the associated .cif file,⁷⁸ there are 3 Ca²⁺ ions, namely Ca1, Ca2, and Ca3. Ca1 and Ca3 have full occupancy, whereas, Ca2 has half occupancy. Similarly, there are 3 water molecules in the interlayer space that have half occupancy, which are Wat2, Wat3, and Wat4. All of these ions with half-occupied sites exist in the interlayer space of the tobermorite 14Å. When it comes to generating a supercell, it is easy to treat the fully occupied sites in the unit cell. However, sites with half occupancy require special treatment. This is because it is important to maintain the same overall number of ions while taking into consideration all possible sites for the them.

Here, we describe this treatment on Ca2 ion in detail, and a similar one was performed for the three water molecules. In **Figure 3**, we show the duplication of the unit cell along the a-axis as a

first step to eliminate the half occupancy issue for Ca₂ ion. These Ca₂ ions exist in 4 symmetric sites. Each two of the four sites exist in one of the two interlayer spaces in the unit cell. For instance, the two symmetry positions: (x, y, z) & $(x, y+1/2, -z)$ exist in one interlayer space, and the other two: $(x+1/2, y, z+1/2)$ & $(x+1/2, y+1/2, -z+1/2)$ exists in the other interlayer space as shown in **Figure 3**. It is worth noting that the interlayer space separates between the calcium-silicates layers in the family of tobermorites and usually contains water molecules and Ca²⁺ ions. All atomistic visualizations in this thesis were generated using the software VESTA.⁷⁹

After duplicating the cell in the direction of the a-axis (the smallest dimension of the unit cell), we placed in each cell a fully occupied ion in each one of the interlayer spaces (without repeating the sites in the two-unit cells). Finally, in the two-unit cells, we have in total 4 Ca₂ ions, and all of the symmetry-related sites are now represented without repetition. For example, the (x, y, z) site is fully occupied in one unit cell but is empty in the other one.

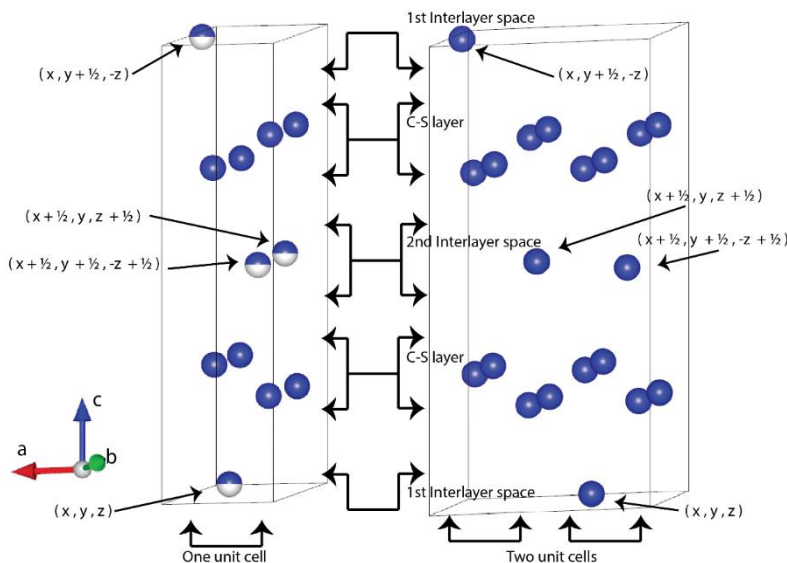


Figure 3. Fixing the half-occupied sites in the unit cell of tobermorite 14Å.³⁷ Left visualization shows a single unit cell with only Ca ions shown. Solid blue spheres represent Ca ions with full occupancy, while half-blue half-white spheres represent Ca ions with half occupancy. Also shown are the four symmetry operations of the crystal structure exemplified on the half-occupied Ca sites (Ca₂). See the text for the description of these sites. Right visualization represents two-unit cells after duplication along the a-axis. Lower and upper interlayer spaces are for the same interlayer because of the periodic boundary conditions.

3.1.2. Duplicating the structure into a (6 x 4 x 1) supercell and doping Na⁺ ions

Fixing the half occupancy problem is then followed by duplicating the cell again, which has been already duplicated once, to produce a 6 x 4 x 1 supercell, shown in **Figure 4b**. The reason behind this second duplication is twofold; first, to minimize the artificial effects from the periodic boundary conditions implemented in the MD codes, and second, to be able to use a proper interatomic potential cutoff while using minimum image convention, which is taken in this study to be 11Å. Minimum image convention is a periodic boundary condition built-in routine in the used MD codes, which controls the interaction of the particles with the nearest images of all the other particles. The next step is to introduce Na⁺ ions into the pristine tobermorite (6 x 4 x 1) supercell to produce a doped tobermorite 14Å representative for the C-N-S-H structure. This was done following the work of Özçelik et al.^{11,12} In their work, they systematically employed density functional theory (DFT) calculations to determine the charge balancing mechanism required for replacing Ca²⁺ ions with Na⁺ ions, to deduce the most favorable site for Na⁺ ions along the c-axis (either replacing the inter-layer or the intra-layer Ca²⁺ ions as in **Figure 4b**), and to delineate the energetically favorable Na⁺ ions concentration and distribution within the same layer.

The authors of Ref.¹¹ explained that for tobermorite 14Å each Na⁺ ion introduced, a proton H⁺ is also introduced to compensate the charge of the removed Ca²⁺ ion, which is shown in **Figure 4c**. This proton is then bonded to the dangling oxygen ion of one of the two nearest bridging silicates closest to the replaced Ca²⁺ ion. This created asymmetry in the local distribution of electrons in the DFT calculations and split a nearby water molecule into a free hydroxyl group and a proton. This proton is then bonded to the other nearest dangling oxygen ion of the bridging silicates. In conclusion, for each Ca²⁺ ion and an associated water molecule in the interlayer space replaced with an Na⁺ ion, the nearest two dangling oxygen ions from the silicates layer are replaced

with hydroxyl groups, and one new free hydroxyl group is introduced in the interlayer space. In addition to this, the authors of **Reference 11** explained that in tobermorite 14Å, Ca²⁺ ions are replaced with Na⁺ ions more favorably in the interlayer space.

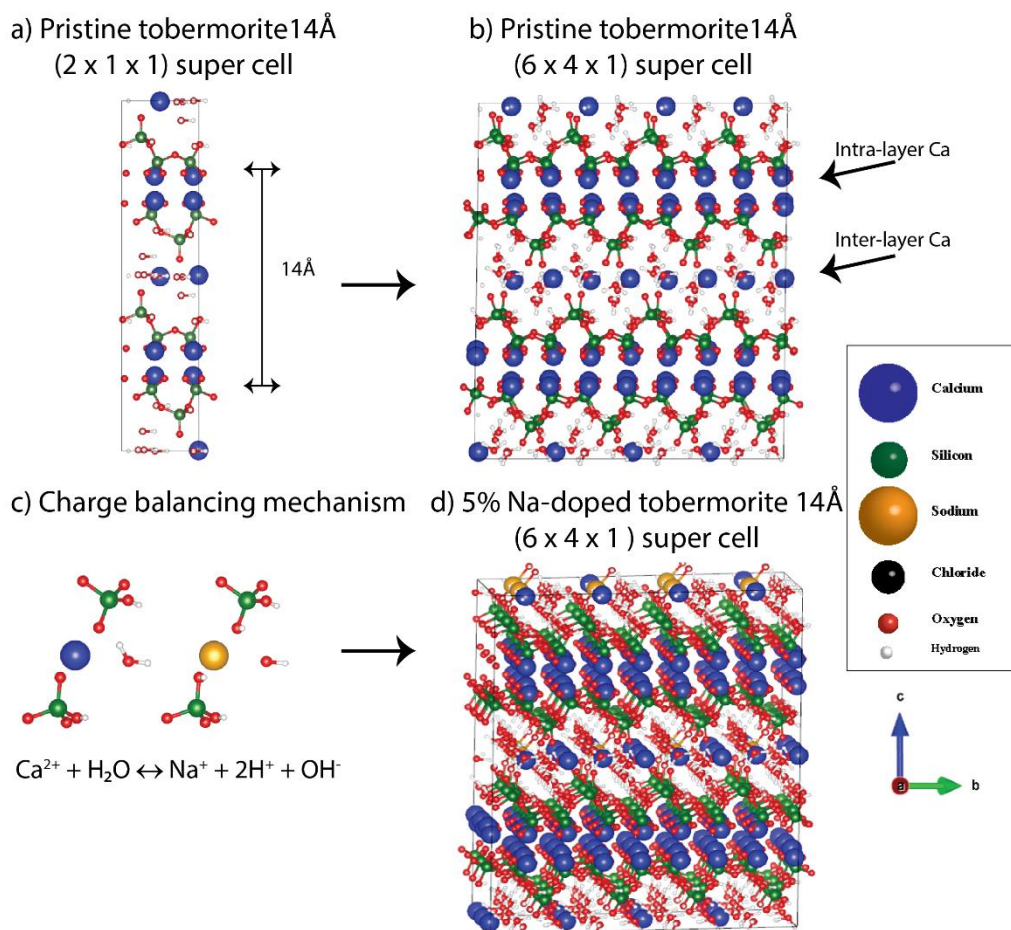


Figure 4. (a) and (b) illustrate duplicating pristine tobermorite 2-unit cells into a 6 x 4 x 1 supercell. (c) Shows the charge balancing mechanism for replacing one Ca²⁺ ion and a whole water molecule with an Na⁺ ion, a proton that forms a hydroxyl group, and a dissociated water molecule that formed another two hydroxyl groups according to **Reference 11**. (d) 5% Na doped tobermorite 6 x 4 x 1 supercell (titled to show substituted Na⁺ ions behind Ca²⁺ ions).

The next thing is to choose a percentage for the inserted Na⁺ ions and their distribution within the interlayer space. In Ref. 12, Özçelik et al. examined the stability of clinotobermorite that is doped with increasing concentration of Na⁺ ions. Clinotobermorite is a mineral that is structurally similar to tobermorite 14Å.³⁸ However, its silicate layers are crosslinked across the

interlayer space while they are not in the case of tobermorite 14Å. They examined different Na/Ca ratios starting from 0% to 25%, and they concluded that the thermodynamic stability deteriorates rapidly after increasing the Na⁺ ions content by more than 11%. This work only examines replacing 5% of Ca²⁺ ions by Na⁺ ions, which corresponds to only 12 ions out of the original 220 Ca²⁺ ions in the supercell. Every 6 Na⁺ ions are symmetrically distributed in one of the two interlayer spaces in the supercell shown in **Figure 4d**. This corresponds to a unit formula Ca_{4.75} Na_{0.25} Si₆ O_{15.5} (OH)_{2.75} · 6.75H₂O. We also tried to simulate higher Na⁺ concentrations, such as 8% and 11%. However, these simulations crashed and suffered sudden increases in system temperature. An explanation for that in literature can be that as the percentage of Na⁺ concentration increases in cement hydration products, the degree of depolymerization in the silicate layers also increases.^{17,65} This results in more defective silicate chains and the existence of more Q¹ and Q⁰ silicate tetrahedra, and less number of Q² tetrahedra. In this work, we use a non-defected tobermorite 14Å structure where all silicate groups are Q². In other words, what might cause the instability of simulations at higher Na⁺ concentrations is that the system favors breaking the silicate chains to produce more monomers and that the nature of the used classical interatomic potential cannot grasp and describe this complex chemical evolution of the system. A future solution for this problem is to examine higher Na⁺ concentrations using more defective molecular models and a classical force field or to use quantum mechanical DFT calculations to spontaneously allow this depolymerization reaction to occur, both of which are beyond the scope of this work.

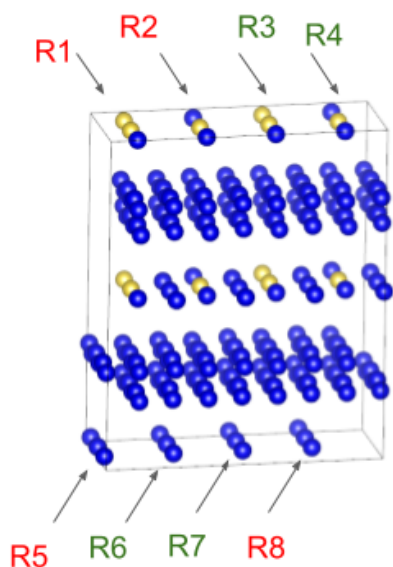
3.1.3. Distributing Interlayer Ions Upon Cleaving the (001) Surface

The next step of building the molecular model is to cleave the (001) surface in both the undoped and the 5% Na-doped structures from the interlayer region. To do so, we need to distribute the 24 interlayer Ca²⁺ ions, in the case of the undoped tobermorite, on the two new cleaved

surfaces. However, in the 5% Na-doped tobermorite, we will need to distribute 18 Ca^{2+} ions and 6 Na^+ ions that originally existed in the interlayer region. This equal distribution of ions that previously existed in the interlayer space on the two created surfaces is important as not to create a charge asymmetry between the two surfaces, an artificial dipole moment, and an artificial preference for the adsorption of a particular ion on a particular surface.

In the undoped structure, distributing the Ca^{2+} ions on the two surfaces is a straightforward symmetric division of the 24 ions into 12 on the top surface and 12 on the bottom surface. However, distributing the ions (18 Ca^{2+} ions and the 6 Na^+ ions) in the 5% Na-doped tobermorite requires more clarification. Similarly, special treatment must also be done while distributing the hydroxyl groups resulted from the charge balancing mechanism of replacing Ca^{2+} ions with Na^+ ions.¹¹ Firstly, as shown in **Figure 5**, we can see in the left visualization the distribution of Na^+ and Ca^{2+} ions (all other species are not shown for clarity) in the 5% Na-doped tobermorite 14Å before relaxing the structure. In this visualization, the upper and lower surfaces belong to the same interlayer space because of the periodic boundary conditions. After cleaving the interlayer space and increasing the length of the c-axis of the 5% Na-doped tobermorite 14Å, shown in the right visualization of **Figure 5**, the lower and upper surfaces are now distinctive ones containing 3 Na^+ and 9 Ca^{2+} ions each. The less ordered atomic sites in the right visualization, especially in the interlayer region, are because cleaving the surface and distributing the ions are done after relaxing the bulk structure in a long (3 ns) MD simulation in the NST ensemble (constant number of particles, constant stress, and constant temperature). This relaxation enabled the ions in the interlayer space to diffuse and to adjust their locations based on the surrounding environment.

Before cleaving the (001) surface



After cleaving the (001) surface

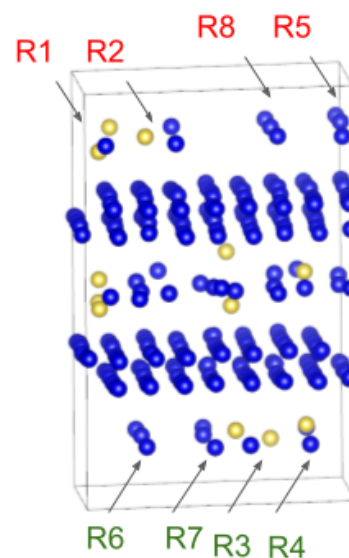


Figure 5. In the left visualization, the original 5% Na-doped tobermorite 14Å (6 x 4 x 1) supercell before any bulk relaxation or cleaving the (001) surface. On the right, the 5% Na-doped tobermorite 14Å (6 x 4 x 1) supercell after, relaxing the bulk structure, then cleaving the (001) surface and increasing the c-axis, and distributing Ca^{2+} and Na^+ ions that originally existed in the interlayer space on the two newly created surfaces. Solid blue spheres represent Ca ions, while solid orange spheres represent Na ions. Red and green notation represent rows of atoms originally located in the same interlayer space in the bulk structure and then shifted to be on the upper and lower created surfaces, respectively. Note that in the bulk structure (left), periodic boundary conditions set the rows R1 – R8 in the same interlayer space.

On the other hand, special treatment must also be done while distributing the hydroxyl groups resulted from the charge balancing mechanism of replacing Ca^{2+} ions with Na^+ ions. The goal is that the local ionic environment of the Na^+ ions moved to the cleaved (001) surfaces are consistent with the results obtained from the previous DFT calculations.¹² A solution for this, depicted in **Figure 6**, depends on whether the considered Na^+ ion is located on the upper or the lower surface. To achieve the goal, shown in the top visualization of **Figure 6**, a Na^+ ion on the upper surface must have two hydroxyl groups on the same upper surface: the lower hydroxyl groups that are attached to the nearest bridging silicate and the free hydroxyl group that previously resulted from water dissociation. The procedure for Na^+ ions located on the lower surface is exactly

the opposite and illustrated in the bottom visualization of **Figure 6**. In cleaving the (001) surface done by increasing the length of the c-vector, the location of the bridging silicates coordinating the Na^+ ions adjust automatically. However, the free hydroxyl groups are the ones that need to be manually shifted to the lower or the upper surface based on the location of the Na^+ ions. This procedure is crucial to ensure that the number of the hydroxyl groups on each surface is the same to maintain the same overall charge of the two surfaces.

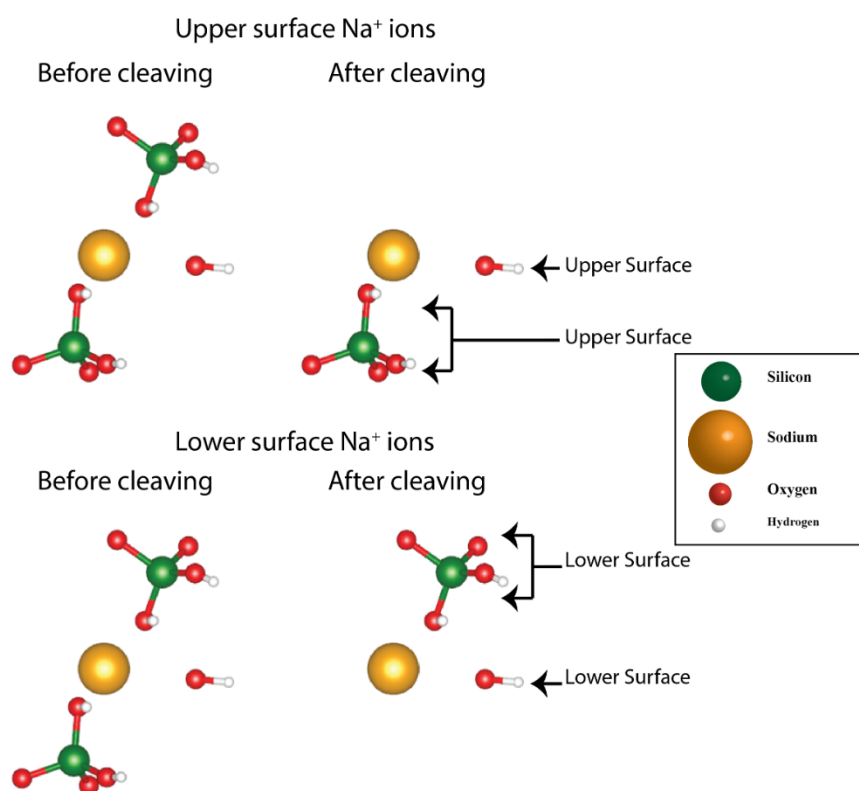


Figure 6. Adjusting the location of the bridging silicates hydroxyl groups and the free ones resulted from the charge balancing mechanism on the newly created (001) surfaces. The procedure depends on the location of the considered Na^+ ion, whether on the top or bottom surfaces. Top visualization shows Na^+ ions before surface cleavage and after positioning on the upper surface, while bottom visualization shows Na^+ ions before surface cleavage and after positioning on the lower surface. Before cleaving, each Na^+ ion is coordinated by 3 hydroxyl groups; 2 belonging to the bridging silicates and a free one. Upon cleaving the (001) surfaces, each Na^+ ion becomes coordinated by two hydroxyl groups only; one free and one belonging to the bridging silicate. Solid green spheres represent Si ions, solid orange spheres represent Na ions, solid red spheres represent oxygen ions, and solid white spheres represent hydrogen ions.

3.1.4. Hydrating the cleaved surfaces and inserting Na⁺ and Cl⁻ ions

After both the undoped and the 5% Na-doped bulk solid tobermorite 14Å systems were relaxed (more on simulations' details in the subsequent subsection) and the (001) surfaces were cleaved in both systems, the final step in building the molecular model used in this work is to hydrate these cleaved surfaces. We examined different water volumes based on different numbers of water molecules: 500, 100, 1500, and 2000 molecules, which are shown in **Figure 7**. The heights of these water volumes were calculated based on the water density (1 g/cm³), the area of the solid surfaces in the ab-plane, and the number of water molecules. This step aimed to choose a number of water molecules that are large enough to allow for water density to converge to the true bulk water density away from the influence of the solid substrate, which was achieved by calculating the 1-dimensional (1-D) density profile for water in the direction perpendicular to the surface. We concluded that 1500 water molecules are enough to show this convergence of water density at a distance midway between the two solid surfaces. This number of water molecules corresponds to a pore width of 45Å, which is in the range of pores in typical cementitious materials.⁸⁰ This test was only done to the undoped system, and the selected water volume was then applied to the 5% Na-doped system.

Moreover, and while randomly positioning interfacial water molecules, a 2.5Å clearance is initially left between the water molecules and the solid substrate, shown in the 1st and 3rd visualizations in **Figure 8**. The reason for this clearance is to avoid the accidental overlap between any of the introduced interfacial water molecules and the original species from the surface of tobermorite 14Å. The calculations of the height of the water volume include these two 2.5 Å clearances at both surfaces so that the condition of the 1 g/cm³ water density is satisfied. It is also important to mention that there are two types of water molecules: first, those that originally existed

in the interlayer space of the solid tobermorite 14\AA before cleavage the (001) surface, and second, the additional 1500 water molecules added in the created pore. However, after running simulations, the two types of water molecules will intermix and become indistinguishable.

After water molecules are positioned and equilibrated (more on simulation details will be explained in the next subsections), the next and final step is to insert Na^+ and Cl^- ions in the pore. We replaced 26 water molecules with 13 Na^+ and 13 Cl^- ions, as shown in the 2nd and 4th visualizations **Figure 8**. This number of ions corresponds to a concentration of 0.5 mol/L, which is also in the upper part of the typical range of salts' concentrations in cementitious materials.^{20,25,81} These Na^+ and Cl^- ions are initially randomly positioned at the pore center to avoid any biased initial configuration. These two final systems are shown in **Figure 9**: the undoped tobermorite 14\AA + 0.5 mol/L NaCl in the pore and 5% Na-doped tobermorite 14\AA + 0.5 mol/L NaCl in the pore, are now the final molecular structures that will be simulated and examined thoroughly in this work.

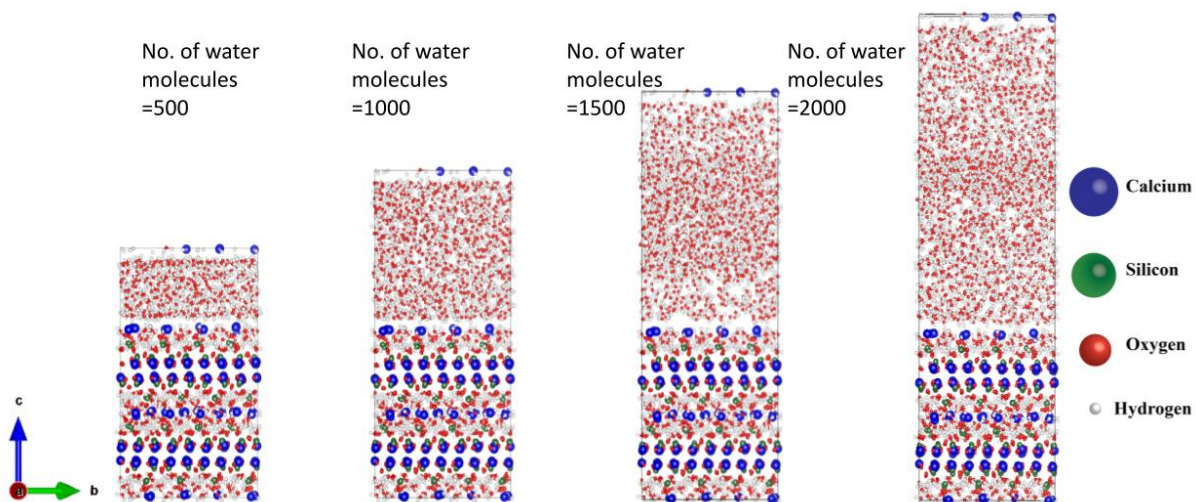


Figure 7. Different water volumes above the surface of the undoped tobermorite 14\AA ($6 \times 4 \times 1$) supercell. From left to right, shown is the visualization of 500, 1000, 1500, and 2000 water molecules. The color legend is shown on the far right.

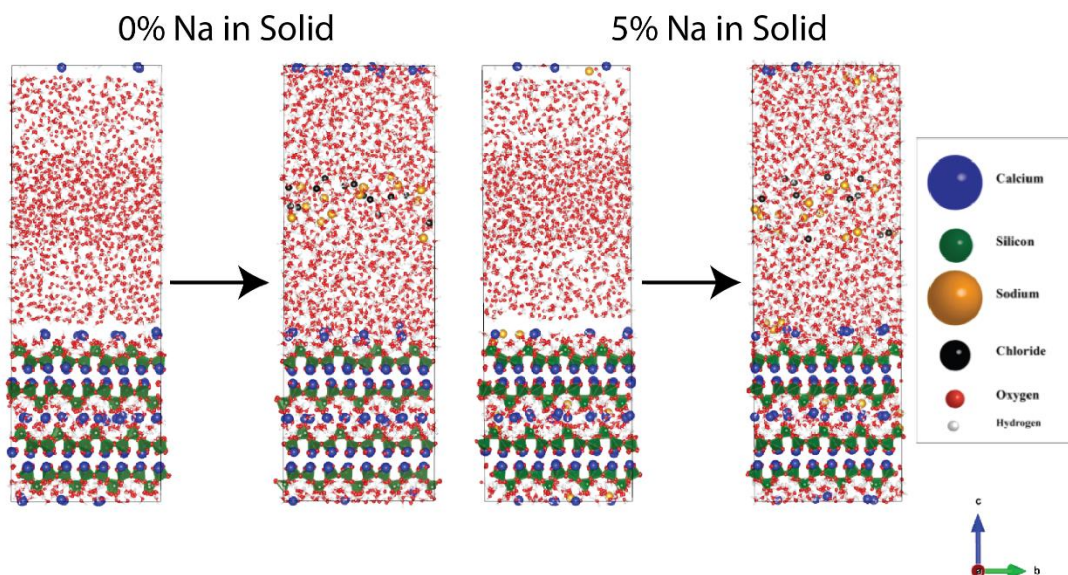


Figure 8. The 1st and 2nd two visualizations represent the undoped tobermorite 14Å before and after inserting the 0.5 mol/L NaCl concentration in the 1500 interfacial water molecules. The 3rd and 4th visualizations are those for the 5% Na-doped tobermorite 14Å. The initial 2.5Å clearance left between water and the solid substrate can be seen before equilibrating the two systems in the 1st and 3rd visualizations.

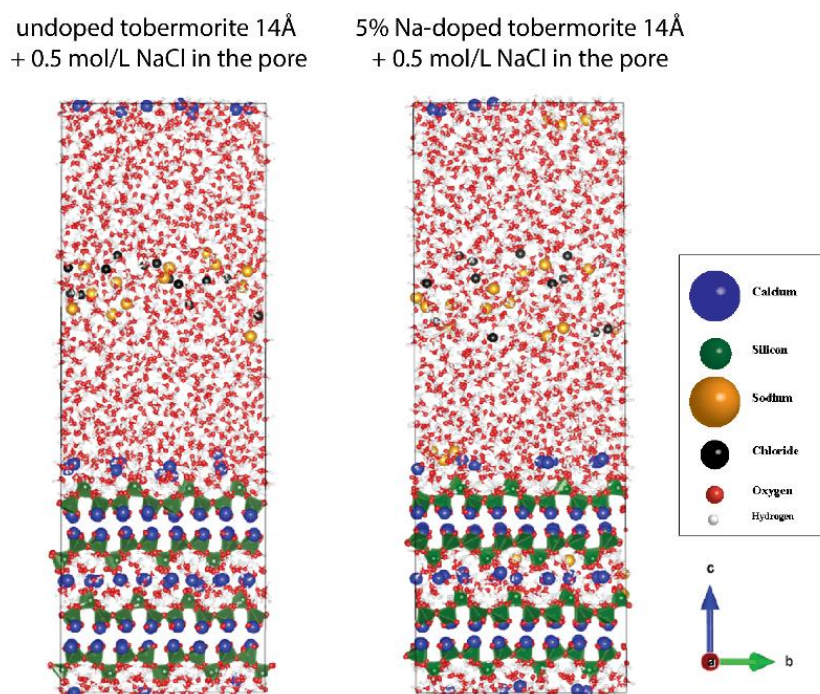


Figure 9. The visualizations of the final two molecular models as examined in this work. On the left visualization, shown is the undoped tobermorite 14Å + 0.5 mol/L NaCl in the pore. The right visualization shows the 5 % Na-doped tobermorite 14Å + 0.5 mol/L NaCl in the pore. The color legend is shown on the far right.

3.2. Force Field

The force field used in this study is composed of 3 main components: the description of the intramolecular and intermolecular interactions related to water molecules, the description of the interactions between the different species of the solid tobermorite 14Å, and the description of the interactions between solvated Na⁺ and Cl⁻ ions with the water molecules and with the solid tobermorite species. Firstly, regarding water molecules description, we believe that flexible water models are crucial in studying interfaces because of the conformational degrees of freedom that flexibility introduces. These degrees of freedom enable water molecules to adjust their atomic orientation and arrangement based on the local environment.²¹ In this work, the used water model is the flexible model known as SPC/Fw, which allows for the oscillations of both the two intramolecular OH bonds and the HOH angle.⁷²

Secondly, to describe the interactions in the calcium silicate layers of the tobermorite 14Å, we adopted a formal-charge rigid ion representation for all species (Ca, Si, and H) except for the oxygen ions. For the latter, we used the polarizable core-shell (CS) model of Dick and Overhauser⁷¹ to represent the oxygen ions (Os) and the oxygen ions in the hydroxyl groups (Oh). An ion described by the CS model is a two-particle system with a positive core and a negative shell connected with a harmonic spring. The sum of the charges of the two particles is equal to the formal charge of the oxygen ions (-2). In the adiabatic version of the CS model, the shells are assigned a small mass such that there is no transfer of energy between the oscillations of the core-shell unit and the rest of the crystal. This CS representation is very similar to the classical Drude oscillator model widely used to model organic systems.⁸² The herein adopted model for the calcium silicate layers with formal charges for the ions and a CS representation for the highly polarizable oxide ion provide a clear advantage over models that incorporate a partial charge

representation for the ions, which are usually based on fully rigid ions. This advantage manifests itself in the ability of the CS oxide ions to adapt their polarization to the local environment, as we detail in the next subsection. Moreover, the usage of the formal charge ensures a charge-neutral system whenever defects and dopants (such as Na^+ ions) are introduced.

Finally, interatomic potentials for Na^+ and Cl^- ions are based on the seminal work of Joung and Cheatham.⁸³ The interactions between these ions, water, and tobermorite 14\AA species were obtained by applying the Lorentz-Berthelot combining rules and adopted from the work of Parker et al.,⁸⁴⁻⁸⁸ Gale et al.,⁸⁹ and ClayFF.⁶⁶ The full set of species notation, their charges, and atomic masses can be found in the supporting information in **Table 1** and **Table 2**. Moreover, the full expressions for the intermolecular and intramolecular potentials, how they are calculated, and their corresponding references can be found in **Table 4**, **Table 5**, and **Table 6**.

In the next subsections, we present the analysis done on the effect of different local environments on the oxygen ion's core-shell distance (polarization). We then present in detail the inter-molecular and intra-molecular interactions used in this work. Finally, we present the ClayFF force field interatomic interactions used to validate and benchmark the performance of the force field used in this work.

3.2.1. Core-Shell distance analysis

In this subsection, we describe the analysis done to investigate different oxygen ions environments and the effect that the surrounding ions have on the polarization of oxygen ions attached to the calcium-silicates layers. This analysis is done only on the bulk solid undoped tobermorite 14\AA ($6 \times 4 \times 1$) supercell after the 3 ns of molecular dynamics equilibration in the NST ensemble (constant number of particles, constant stress, and constant temperature) and using

the subsequent 2 ns production simulation in the NVT (constant number of particles, constant volume, and constant temperature) ensemble. For the full simulation details, we refer the reader to the upcoming section 3.3.3. in the thesis.

Firstly, the number of silicates' oxygens having specific core-shell (CS) distance is calculated and averaged over the 2ns NVT simulation. Shown in **Figure 10a** is the normalized distribution of oxygen ions for each CS distance. The bimodality of the distribution is very clear, which indicates that oxygen ions attached to the calcium silicate layer are two populations based on their degree of polarization. To know exactly which oxygen ions are of which degree of polarization, mapping was performed between this distribution and the structure visualization shown in **Figure 10c**. For this purpose, the CS distance distribution is categorized into two populations: Os D1 and Os D2. The locations of the oxide ions belonging to each of these two populations are highlighted in the bc-plane of tobermorite in **Figure 10b and c**. However, while the atomic visualization is for one snapshot, the CS distance contour plot in **Figure 10b** is averaged over the 2 ns simulation.

Moreover, we notice that oxygen ions confined between two silicon ions are the ones with smaller polarization. While oxygen ions sandwiched between a silicon ion and a calcium ion have a larger polarization. This analysis can never be done using rigid charge models. It was only possible in this work because oxygen ions in the herein representation can adjust their polarization based on the surrounding environments. For our study, this is very important for oxygen ions at the interface with water molecules. This is because interfacial solid oxygen ions must have the dynamic flexibility to adjust their polarization based on the adsorbates; Na^+ , Cl^- or water. Moreover, this flexibility has a very important influence on the hydrogen bond network formed between the solid substrate and the water molecules. Additionally, it can influence the degree of

surface hydrophilicity and, subsequently, the macroscopic properties developed in the pore water, such as the electric field and the static dielectric constant.^{59–61}

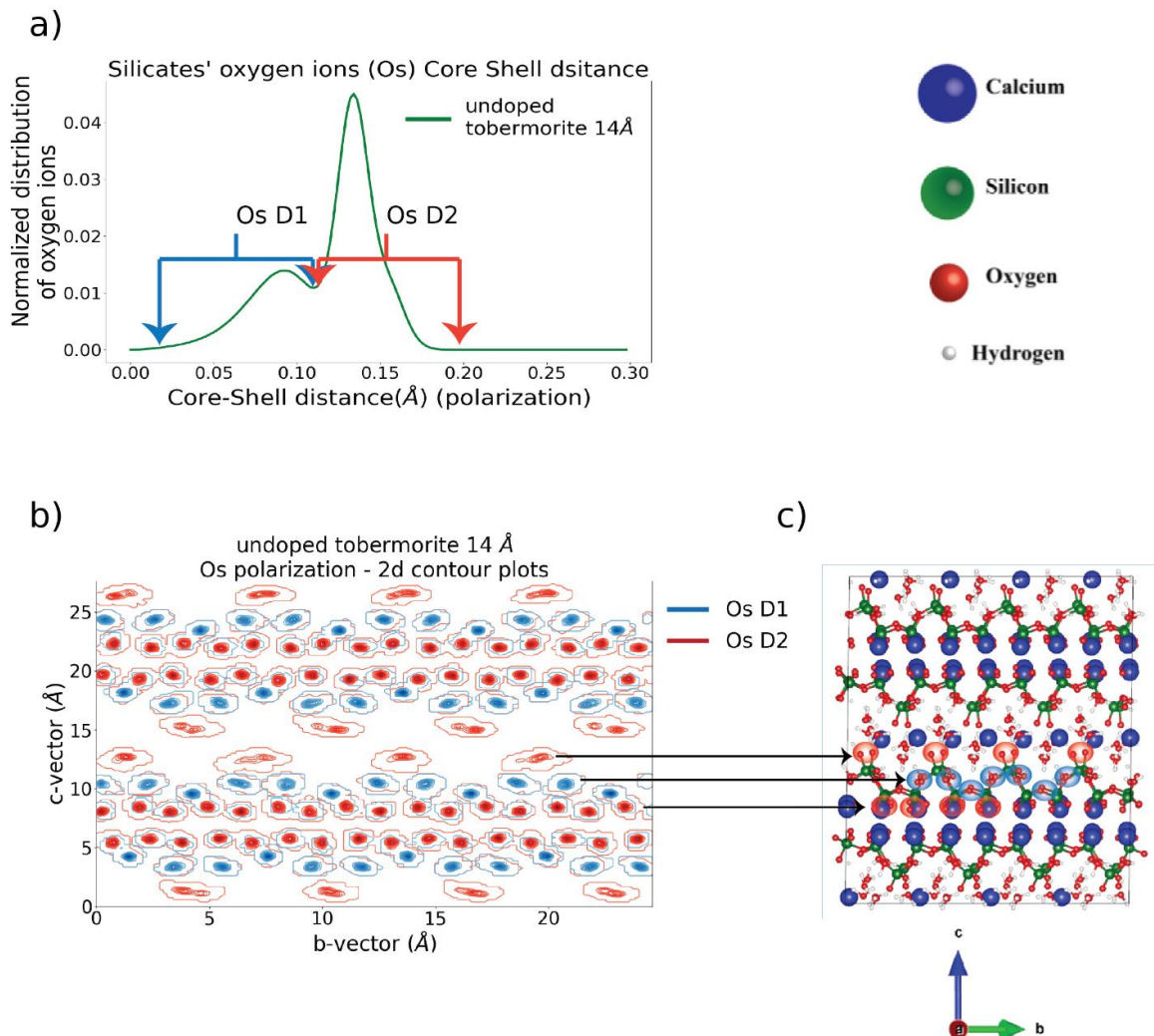


Figure 10. Silicates' oxygens polarization analysis using CS model. This analysis was only done to the bulk solid undoped tobermorite 14 Å (6 x 4 x 1) supercell. (a) The normalized distribution for a given CS distance was calculated from a 2 ns MD simulation. Os D1 and Os D2 are the ranges of the two peaks of the CS distribution. (b) 2-d contour plots corresponding to the two CS distance peaks visualized in the bc-plane of tobermorite based on 2 ns simulation. (c) tobermorite bc-plane atomic visualization for the last snapshot of the 2ns simulation. Shown in the top right is the color legend for different atomic species. Arrows between (b) and (c) match the positions of the oxygen ions with smaller and larger polarization values from the contour plots and the atomic visualization. Oxygen ions with smaller polarization are those confined between two silicon ions. In comparison, those with the larger polarization are attached to one silicon ion from one side and a calcium ion from the other.

3.2.2. Force Field Parameters

In this section, we describe in detail the force field parameters used in this work. We first describe the species' notations, charges, and masses in **Table 1** and **Table 2**. Then we present the Lorentz-Berthelot combining rules in **Table 3**. Note that the Lennard-Jones (LJ) potential used in this work can be written either in terms of A and B (**Equation 2**) or in terms of R_0 and D_0 (**Equation 3**).

$$V_{ij}(r_{ij}) = \frac{A_{ij}}{r_{ij}^{12}} - \frac{B_{ij}}{r_{ij}^6}$$

Equation 2. Lennard-Jones in the A and B notation.

$$V_{ij}(r_{ij}) = D_{o,ij} \left[\left(\frac{R_{o,ij}}{r_{ij}} \right)^{12} - 2 \left(\frac{R_{o,ij}}{r_{ij}} \right)^6 \right]$$

Equation 3. Lennard-Jones in the R_0 and D_0 notation.

The combining rules are used to calculate the R_0 and D_0 constants for some interactions, as noted in **Table 4** and **Table 5**. Then, for these specific interactions, this was followed by transforming the LJ potential into the A and B form, which is the one that is directly implemented in DLPOLY 4 code. The rest of the interactions are either in the A and B form in the original papers or directly transformed into the A and B from these original papers. Moreover, in the spirit of the ClayFF⁶⁶ force field, Ow - Hh, and Hw - Oh (full species' notations are mentioned in **Table 1** and **Table 2**) interactions were omitted. These interactions were omitted for two reasons: first, they do not exist in the ClayFF force field, and second, any attempt to include these interactions as described in the work of Kerisit et al.⁸⁴ resulted in an instability of the simulations cell with a humungous increase in the simulation temperature. It is also important to mention that within the same molecule, and we only have water and hydroxyl groups here as molecules as shown in **Table 6**, intramolecular Coulomb and Van der Waals interactions are automatically subtracted from the calculations. Similarly, no coulomb or Van der Waals interactions exist between the core-shell unit

inside the same ion. Finally, we note that all van der Waals intermolecular interactions that involve an ion represented by a core-shell model (Os and Oh) are calculated based on the coordinates of the shells, not the cores.

Species	Core Charge (e)	Core mass (a.m.u.)	Shell Charge (e)	Shell mass (a.m.u.)	$k\left(\frac{eV}{\text{\AA}^2}\right)$
Silicate Oxygen (Os)	0.848	15.8	-2.848	0.2	74.92038
Hydroxyl Oxygen (Oh)	0.900	15.8	-2.300	0.2	74.92038

Table 1. Charges and masses for cores and shells

Species	Charge (e)	mass (a.m.u.)
Water Oxygen (Ow)	-0.82	15.966
Water Hydrogen (Hw)	0.41	1.008
Hydroxyl Hydrogen (Hh)	0.40	1.008
Calcium (Ca)	2.00	40.078
Silicon (Si)	4.00	28.085
Sodium (Na)	1.00	22.989769
Chloride (Cl)	-1.00	35.453

Table 2. Species' charges and masses

Distance	$R_{o,ij} = \frac{1}{2}(R_{o,i} + R_{o,j})$
Energy	$D_{o,ij} = \sqrt{D_{o,i} * D_{o,j}}$

Table 3. Lorentz-Berthelot combining rules.⁹⁰

Species	Interaction	Parameters	Species	Interaction	Parameters
Os - Os ⁸⁶	Buckingham $V_{ij}(r_{ij}) = A_{ij} * e^{\frac{-r_{ij}}{\rho_{ij}}} - \left(\frac{C_{ij}}{r_{ij}^6}\right)$	$A_{ij}(eV)=22764$ $\rho_{ij}(\text{\AA})=0.149$ $C_{ij}(eV.\text{\AA}^6)=27.88$	Oh - Ow ^{66(a)}	Lennard-Jones $V_{ij}(r_{ij}) = \frac{A_{ij}}{r_{ij}^{12}} - \frac{B_{ij}}{r_{ij}^6}$	$A_{ij}\left(\frac{eV}{\text{\AA}^{12}}\right)=27290.8535$ $B_{ij}\left(\frac{eV}{\text{\AA}^6}\right)=27.12246$
Os - Ow ⁸⁷	Buckingham $V_{ij}(r_{ij}) = A_{ij} * e^{\frac{-r_{ij}}{\rho_{ij}}} - \left(\frac{C_{ij}}{r_{ij}^6}\right)$	$A_{ij}(eV)=22764.00$ $\rho_{ij}(\text{\AA})=0.1490$ $C_{ij}(eV.\text{\AA}^6)=15.46$	Oh - Hh ⁸⁴	Buckingham $V_{ij}(r_{ij}) = A_{ij} * e^{\frac{-r_{ij}}{\rho_{ij}}} - \left(\frac{C_{ij}}{r_{ij}^6}\right)$	$A_{ij}(eV)=436.76$ $\rho_{ij}(\text{\AA})=0.25$ $C_{ij}(eV.\text{\AA}^6)=2.5$
Os - Oh ⁸⁶	Buckingham $V_{ij}(r_{ij}) = A_{ij} * e^{\frac{-r_{ij}}{\rho_{ij}}} - \left(\frac{C_{ij}}{r_{ij}^6}\right)$	$A_{ij}(eV)=22764$ $\rho_{ij}(\text{\AA})=0.149$ $C_{ij}(eV.\text{\AA}^6)=13.94$	Ca - Os ⁹¹	Buckingham $V_{ij}(r_{ij}) = A_{ij} * e^{\frac{-r_{ij}}{\rho_{ij}}} - \left(\frac{C_{ij}}{r_{ij}^6}\right)$	$A_{ij}(eV)=1090.4$ $\rho_{ij}(\text{\AA})=0.3437$ $C_{ij}(eV.\text{\AA}^6)=0.00$
Os - Hh ⁸⁶	Buckingham $V_{ij}(r_{ij}) = A_{ij} * e^{\frac{-r_{ij}}{\rho_{ij}}} - \left(\frac{C_{ij}}{r_{ij}^6}\right)$	$A_{ij}(eV)=311.97$ $\rho_{ij}(\text{\AA})=0.25$ $C_{ij}(eV.\text{\AA}^6)=0.00$	Ca - Oh ⁹¹	Buckingham $V_{ij}(r_{ij}) = A_{ij} * e^{\frac{-r_{ij}}{\rho_{ij}}} - \left(\frac{C_{ij}}{r_{ij}^6}\right)$	$A_{ij}(eV)=2170.00$ $\rho_{ij}(\text{\AA})=0.297$ $C_{ij}(eV.\text{\AA}^6)=0.00$
Os - Hw ⁸⁴	Buckingham $V_{ij}(r_{ij}) = A_{ij} * e^{\frac{-r_{ij}}{\rho_{ij}}} - \left(\frac{C_{ij}}{r_{ij}^6}\right)$	$A_{ij}(eV)=311.97$ $\rho_{ij}(\text{\AA})=0.25$ $C_{ij}(eV.\text{\AA}^6)=0.00$	Ca - Ow ^{89(a)}	Lennard-Jones $V_{ij}(r_{ij}) = \frac{A_{ij}}{r_{ij}^{12}} - \frac{B_{ij}}{r_{ij}^6}$	$A_{ij}\left(\frac{eV}{\text{\AA}^{12}}\right)=7591.38961$ $B_{ij}\left(\frac{eV}{\text{\AA}^6}\right)=5.370966$
Oh - Oh ⁸⁶	Buckingham $V_{ij}(r_{ij}) = A_{ij} * e^{\frac{-r_{ij}}{\rho_{ij}}} - \left(\frac{C_{ij}}{r_{ij}^6}\right)$	$A_{ij}(eV)=22764$ $\rho_{ij}(\text{\AA})=0.149$ $C_{ij}(eV.\text{\AA}^6)=6.97$	Si - Os ⁸⁶	Buckingham $V_{ij}(r_{ij}) = A_{ij} * e^{\frac{-r_{ij}}{\rho_{ij}}} - \left(\frac{C_{ij}}{r_{ij}^6}\right)$	$A_{ij}(eV)=1283.907$ $\rho_{ij}(\text{\AA})=0.32052$ $C_{ij}(eV.\text{\AA}^6)=10.662$
Si - Ow ⁸⁶	Buckingham $V_{ij}(r_{ij}) = A_{ij} * e^{\frac{-r_{ij}}{\rho_{ij}}} - \left(\frac{C_{ij}}{r_{ij}^6}\right)$	$A_{ij}(eV)=1283.907$ $\rho_{ij}(\text{\AA})=0.32052$ $C_{ij}(eV.\text{\AA}^6)=10.66$	Na - Oh ⁸⁷	Buckingham $V_{ij}(r_{ij}) = A_{ij} * e^{\frac{-r_{ij}}{\rho_{ij}}} - \left(\frac{C_{ij}}{r_{ij}^6}\right)$	$A_{ij}(eV)=858.79$ $\rho_{ij}(\text{\AA})=0.3065$ $C_{ij}(eV.\text{\AA}^6)=0.0$
Si - Oh ⁸⁶	Buckingham $V_{ij}(r_{ij}) = A_{ij} * e^{\frac{-r_{ij}}{\rho_{ij}}} - \left(\frac{C_{ij}}{r_{ij}^6}\right)$	$A_{ij}(eV)=983.556$ $\rho_{ij}(\text{\AA})=0.32052$ $C_{ij}(eV.\text{\AA}^6)=10.66$	Cl - Ca ^{66(a),(b)&(c)}	Lennard-Jones $V_{ij}(r_{ij}) = \frac{A_{ij}}{r_{ij}^{12}} - \frac{B_{ij}}{r_{ij}^6}$	$A_{ij}\left(\frac{eV}{\text{\AA}^{12}}\right)=28867.6285$ $B_{ij}\left(\frac{eV}{\text{\AA}^6}\right)=1.88492$

Table 4. Intermolecular interactions

^(a)Conversion from the LJ form mentioned in paper and form used in this work must be done.

^(b)Combining rules were used to calculate parameters for LJ potential.

^(c)Octahedral Calcium was used from Ref. ⁶⁶

^(d)Values for Na & Cl are obtained from the SPC/E table in Ref.⁹², and values for Ow are obtained from Ref.⁹³

Species	Interaction	Parameters	Species	Interaction	Parameters
Na - Na ^{92(a),(d)}	Lennard-Jones $V_{ij}(r_{ij}) = \frac{A_{ij}}{r_{ij}^{12}} - \frac{B_{ij}}{r_{ij}^6}$	$A_{ij}(\frac{eV}{\text{\AA}^{12}})=629.2845$ $B_{ij}(\frac{eV}{\text{\AA}^6})=6.20414$	Cl - Si ^{66(a),(b)}	Lennard-Jones $V_{ij}(r_{ij}) = \frac{A_{ij}}{r_{ij}^{12}} - \frac{B_{ij}}{r_{ij}^6}$	$A_{ij}(\frac{eV}{\text{\AA}^{12}})=792.040526$ $B_{ij}(\frac{eV}{\text{\AA}^6})=0.242832$
Na-Cl ^{92(a),(b),(d)}	Lennard-Jones $V_{ij}(r_{ij}) = \frac{A_{ij}}{r_{ij}^{12}} - \frac{B_{ij}}{r_{ij}^6}$	$A_{ij}(\frac{eV}{\text{\AA}^{12}})=38686.44$ $B_{ij}(\frac{eV}{\text{\AA}^6})=21.22653$	Cl - Os ⁸⁷	Buckingham $V_{ij}(r_{ij}) = A_{ij} * e^{-\frac{r_{ij}}{\rho_{ij}}} - (\frac{C_{ij}}{r_{ij}^6})$	$A_{ij}(eV)=1272.25$ $\rho_{ij}(\text{\AA})=0.2352$ $C_{ij}(eV.\text{\AA}^6)=28.46$
Na-Ow ^{92,93(a),(b),(d)}	Lennard-Jones $V_{ij}(r_{ij}) = \frac{A_{ij}}{r_{ij}^{12}} - \frac{B_{ij}}{r_{ij}^6}$	$A_{ij}(\frac{eV}{\text{\AA}^{12}})=5153.6475$ $B_{ij}(\frac{eV}{\text{\AA}^6})=14.46646$	Cl - Oh ⁸⁷	Buckingham $V_{ij}(r_{ij}) = A_{ij} * e^{-\frac{r_{ij}}{\rho_{ij}}} - (\frac{C_{ij}}{r_{ij}^6})$	$A_{ij}(eV)=1272.25$ $\rho_{ij}(\text{\AA})=0.2352$ $C_{ij}(eV.\text{\AA}^6)=14.23$
Cl - Cl ^{92(a),(d)}	Lennard-Jones $V_{ij}(r_{ij}) = \frac{A_{ij}}{r_{ij}^{12}} - \frac{B_{ij}}{r_{ij}^6}$	$A_{ij}(\frac{eV}{\text{\AA}^{12}})=357879.4453$ $B_{ij}(\frac{eV}{\text{\AA}^6})=28.171481$	Cl - Hh ^{87(a)}	Lennard-Jones/nm in DLPOLY $V_{ij}(r_{ij}) = \left(\frac{E_o}{(n-m)} \left[m \left(\frac{r_o}{r_{ij}} \right)^n - n \left(\frac{r_o}{r_{ij}} \right)^m \right] \right)$	$E_o(eV) = 0.03001596$ $n = 9$ $m = 6$ $r_o(\text{\AA}) = 2.379861112$
Cl - Ow ^{92,93(a),(b),(d)}	Lennard-Jones $V_{ij}(r_{ij}) = \frac{A_{ij}}{r_{ij}^{12}} - \frac{B_{ij}}{r_{ij}^6}$	$A_{ij}(\frac{eV}{\text{\AA}^{12}})=128934.9102$ $B_{ij}(\frac{eV}{\text{\AA}^6})=31.57414 \frac{eV}{\text{\AA}^6}$	Ow-Ow ^{93(a),(b)}	Lennard-Jones $V_{ij}(r_{ij}) = \frac{A_{ij}}{r_{ij}^{12}} - \frac{B_{ij}}{r_{ij}^6}$	$A_{ij}(\frac{eV}{\text{\AA}^{12}})= 27277.653$ $B_{ij}(\frac{eV}{\text{\AA}^6})=27.1118827$
Na - Os ⁸⁷	Buckingham $V_{ij}(r_{ij}) = A_{ij} * e^{-\frac{r_{ij}}{\rho_{ij}}} - (\frac{C_{ij}}{r_{ij}^6})$	$A_{ij}(eV)=1226.84$ $\rho_{ij}(\text{\AA})=0.3065$ $C_{ij}(eV.\text{\AA}^6)=0.0$			

Table 5. Intermolecular interactions - continued

^(a)Conversion from the LJ form mentioned in paper and form used in this work must be done.

^(b)Combining rules were used to calculate constants for LJ potential.

^(c)Octahedral Calcium was used from Ref.⁶⁶

^(d)Values for Na & Cl are obtained from the SPC/E table in Ref.⁹², and values for Ow are obtained from Ref.⁹³

Species	Interaction	Parameters	Cutoff (Å)
Oh - Hh ⁸⁶	Morse Potential $V_{ij}(r_{ij}) = D_{ij} \left\{ \left[1 - e^{(-a_{ij}(r_{ij}-r_{ij0}))} \right]^2 - 1.0 \right\}$	$D_{ij}(\text{eV}) = 7.0525$ $a_{ij}(\text{Å}^{-1}) = 3.1749$ $r_0(\text{Å}) = 0.9485$	NA
Os - Si - Os ⁸⁶	Three-Body Interaction $V_{ijk}(r_{ijk}) = \frac{1}{2} k_{ijk} (\theta_{ijk} - \theta_o)^2$	$K_{ijk}(\text{eV/rad}^2) = 2.0972$ $\Theta_0(\text{rad}) = 109.47$	1.8
Oh - Si - Oh ⁸⁸	Three-Body Interaction $V_{ijk}(r_{ijk}) = \frac{1}{2} k_{ijk} (\theta_{ijk} - \theta_o)^2$	$K_{ijk}(\text{eV/rad}^2) = 2.0972$ $\Theta_0(\text{rad}) = 109.47$	1.8
Os - Si - Oh ⁸⁸	Three-Body Interaction $V_{ijk}(r_{ijk}) = \frac{1}{2} k_{ijk} (\theta_{ijk} - \theta_o)^2$	$K_{ijk}(\text{eV/rad}^2) = 2.0972$ $\Theta_0(\text{rad}) = 109.47$	1.8
Ow - Hw ⁹³	$V_{ij}(r_{ij}) = \frac{1}{2} k_b (r_{ij} - r^o)^2$	$k_b = 45.9296 \frac{\text{eV}}{\text{Å}^2}$ $r^o = 1.012 \text{ Å}$	NA
Hw - Ow - Hw ⁹³	$V_{ijk}(r_{ijk}) = \frac{1}{2} k_a (\theta_{ijk} - \theta_o)^2$	$k_a = 3.2913 \frac{\text{eV}}{\text{rad}^2}$ $\theta_o = 113.24^\circ$	NA

Table 6. Intramolecular (bonded) interactions

3.2.3. ClayFF Parameters

This section describes the ClayFF⁶⁶ parameters used in the benchmarking study to compare the lattice parameters between two force fields. The results of this study are shown in section 3.3.2. It is important to mention that the LJ potential in the original paper is written in the form R_0 and D_0 .⁶⁶ Again, combining rules mentioned in **Table 3** were used to calculate the R_0 and D_0 for each

pair. However, also note that in this section, the LJ potential is present in the form of ϵ and σ . The reason behind this is that the LJ potential implemented in the DLPOLY code is either using the A and B form or the ϵ and σ form.

On the other hand, using partial charges from the original ClayFF force field⁶⁶, and the number of ions in this work dictated by the experimentally determined crystal structure of tobermorite, there exist excess charges of +74.4 e in the case of undoped tobermorite solid and +76.38 in the case of 5% Na-doped tobermorite. These additional charges were distributed as follows: half of the excess charges were distributed and subtracted from the cations: Ca, Si, Na & Hh, and the other half were distributed and subtracted from the anions: Os & Oh. This procedure resulted in very small overall systems charges ($-3.26 \times 10^{-9} e$ in the case of undoped tobermorite and $-1.18 \times 10^{-11} e$ in the case of 5% Na-doped tobermorite). Since the overall charges of the two systems are similar, the same values of species' charges of the undoped tobermorite were used for the 5% Na-doped tobermorite for consistency. **Table 7**, **Table 8**, **Table 9**, and **Table 10** summarize all the parameters and notations of the CLAYFF force field.

Species	Charge (e)	mass (a.m.u.)
Silicate Oxygen (Os)	-1.093055555556	16
Hydroxyl Oxygen (Oh)	-0.993055555556	16
Water Oxygen (Ow)	-0.82	15.966
Water Hydrogen (Hw)	0.41	1.008
Hydroxyl Hydrogen (Hh)	0.36538461538	1.008
Calcium (Ca)	1.30038461538	40.078
Silicon (Si)	2.04038461538	28.085
Sodium (Na)	0.997286325067	22.989769

Table 7. ClayFF species' charges and masses

Species	Interaction	Parameters	Species	Interaction	Parameters
Os - Os ⁶⁶	Lennard-Jones $V_{ij}(r_{ij}) = 4\epsilon \left[\left(\frac{\sigma}{r_{ij}} \right)^{12} - \left(\frac{\sigma}{r_{ij}} \right)^6 \right]$	$\epsilon(\text{eV})=0.0067386$ $\sigma(\text{\AA})=3.165541$	Oh - Ow ⁶⁶	Lennard-Jones $V_{ij}(r_{ij}) = 4\epsilon \left[\left(\frac{\sigma}{r_{ij}} \right)^{12} - \left(\frac{\sigma}{r_{ij}} \right)^6 \right]$	$\epsilon(\text{eV})=0.0067386$ $\sigma(\text{\AA})=3.165541$
Os - Ow ⁶⁶	Lennard-Jones $V_{ij}(r_{ij}) = 4\epsilon \left[\left(\frac{\sigma}{r_{ij}} \right)^{12} - \left(\frac{\sigma}{r_{ij}} \right)^6 \right]$	$\epsilon(\text{eV})=0.0067386$ $\sigma(\text{\AA})=3.165541$	Ca - Os ⁶⁶	Lennard-Jones $V_{ij}(r_{ij}) = 4\epsilon \left[\left(\frac{\sigma}{r_{ij}} \right)^{12} - \left(\frac{\sigma}{r_{ij}} \right)^6 \right]$	$\epsilon(\text{eV})= 3.8337\text{e-}5$ $\sigma(\text{\AA})= 4.3661164378$
Os - Oh ⁶⁶	Lennard-Jones $V_{ij}(r_{ij}) = 4\epsilon \left[\left(\frac{\sigma}{r_{ij}} \right)^{12} - \left(\frac{\sigma}{r_{ij}} \right)^6 \right]$	$\epsilon(\text{eV})=0.0067386$ $\sigma(\text{\AA})=3.165541$	Ca - Oh ⁶⁶	Lennard-Jones $V_{ij}(r_{ij}) = 4\epsilon \left[\left(\frac{\sigma}{r_{ij}} \right)^{12} - \left(\frac{\sigma}{r_{ij}} \right)^6 \right]$	$\epsilon(\text{eV})= 3.8337\text{e-}5$ $\sigma(\text{\AA})= 4.3661164378$
Oh - Oh ⁶⁶	Lennard-Jones $V_{ij}(r_{ij}) = 4\epsilon \left[\left(\frac{\sigma}{r_{ij}} \right)^{12} - \left(\frac{\sigma}{r_{ij}} \right)^6 \right]$	$\epsilon(\text{eV})=0.0067386$ $\sigma(\text{\AA})=3.165541$	Ca - Ow ⁶⁶	Lennard-Jones $V_{ij}(r_{ij}) = 4\epsilon \left[\left(\frac{\sigma}{r_{ij}} \right)^{12} - \left(\frac{\sigma}{r_{ij}} \right)^6 \right]$	$\epsilon(\text{eV})= 3.8337\text{e-}5$ $\sigma(\text{\AA})= 4.3661164378$
Ca - Ca ⁶⁶	Lennard-Jones $V_{ij}(r_{ij}) = 4\epsilon \left[\left(\frac{\sigma}{r_{ij}} \right)^{12} - \left(\frac{\sigma}{r_{ij}} \right)^6 \right]$	$\epsilon(\text{eV})= 2.1811\text{e-}7$ $\sigma(\text{\AA})= 5.56669$	Si - Os ⁶⁶	Lennard-Jones $V_{ij}(r_{ij}) = 4\epsilon \left[\left(\frac{\sigma}{r_{ij}} \right)^{12} - \left(\frac{\sigma}{r_{ij}} \right)^6 \right]$	$\epsilon(\text{eV})= 2.3191\text{e-}5$ $\sigma(\text{\AA})= 3.233784$
Ca - Si ⁶⁶	Lennard-Jones $V_{ij}(r_{ij}) = 4\epsilon \left[\left(\frac{\sigma}{r_{ij}} \right)^{12} - \left(\frac{\sigma}{r_{ij}} \right)^6 \right]$	$\epsilon(\text{eV})= 1.3194\text{e-}7$ $\sigma(\text{\AA})= 4.434359$	Ca - Na ⁶⁶	Lennard-Jones $V_{ij}(r_{ij}) = 4\epsilon \left[\left(\frac{\sigma}{r_{ij}} \right)^{12} - \left(\frac{\sigma}{r_{ij}} \right)^6 \right]$	$\epsilon(\text{eV})= 3.5078\text{e-}5$ $\sigma(\text{\AA})= 3.958352$
Si - Si ⁶⁶	Lennard-Jones $V_{ij}(r_{ij}) = 4\epsilon \left[\left(\frac{\sigma}{r_{ij}} \right)^{12} - \left(\frac{\sigma}{r_{ij}} \right)^6 \right]$	$\epsilon(\text{eV})= 7.9810\text{e-}8$ $\sigma(\text{\AA})= 3.302027$	Si - Na ⁶⁶	Lennard-Jones $V_{ij}(r_{ij}) = 4\epsilon \left[\left(\frac{\sigma}{r_{ij}} \right)^{12} - \left(\frac{\sigma}{r_{ij}} \right)^6 \right]$	$\epsilon(\text{eV})= 2.1219\text{e-}5$ $\sigma(\text{\AA})= 2.826020$

Table 8. ClayFF intermolecular interactions^{(a),(b)}

^(a) Combining rules were used to calculate constants for all intermolecular LJ potential.

^(b) Octahedral Calcium was used from Ref. ⁶⁶.

Species	Interaction	Parameters	Species	Interaction	Parameters
Si - Ow ⁶⁶	Lennard-Jones $V_{ij}(r_{ij}) = 4\epsilon \left[\left(\frac{\sigma}{r_{ij}} \right)^{12} - \left(\frac{\sigma}{r_{ij}} \right)^6 \right]$	$\epsilon(\text{eV}) = 2.3191\text{e-}5$ $\sigma(\text{\AA}) = 3.233784$	Na - Oh ⁶⁶	Lennard-Jones $V_{ij}(r_{ij}) = 4\epsilon \left[\left(\frac{\sigma}{r_{ij}} \right)^{12} - \left(\frac{\sigma}{r_{ij}} \right)^6 \right]$	$\epsilon(\text{eV}) = 0.0061657$ $\sigma(\text{\AA}) = 2.7577770$
Si - Oh ⁶⁶	Lennard-Jones $V_{ij}(r_{ij}) = 4\epsilon \left[\left(\frac{\sigma}{r_{ij}} \right)^{12} - \left(\frac{\sigma}{r_{ij}} \right)^6 \right]$	$\epsilon(\text{eV}) = 2.3191\text{e-}5$ $\sigma(\text{\AA}) = 3.233784$	Ow - Ow ⁶⁶	Lennard-Jones $V_{ij}(r_{ij}) = 4\epsilon \left[\left(\frac{\sigma}{r_{ij}} \right)^{12} - \left(\frac{\sigma}{r_{ij}} \right)^6 \right]$	$\epsilon(\text{eV}) = 0.0067386$ $\sigma(\text{\AA}) = 3.165541$
Na - Na ⁶⁶	Lennard-Jones $V_{ij}(r_{ij}) = 4\epsilon \left[\left(\frac{\sigma}{r_{ij}} \right)^{12} - \left(\frac{\sigma}{r_{ij}} \right)^6 \right]$	$\epsilon(\text{eV}) = 0.0056415$ $\sigma(\text{\AA}) = 2.3500126$	Na - Oh ⁶⁶	Lennard-Jones $V_{ij}(r_{ij}) = 4\epsilon \left[\left(\frac{\sigma}{r_{ij}} \right)^{12} - \left(\frac{\sigma}{r_{ij}} \right)^6 \right]$	$\epsilon(\text{eV}) = 0.0061657$ $\sigma(\text{\AA}) = 2.7577770$
Na - Ow ⁶⁶	Lennard-Jones $V_{ij}(r_{ij}) = 4\epsilon \left[\left(\frac{\sigma}{r_{ij}} \right)^{12} - \left(\frac{\sigma}{r_{ij}} \right)^6 \right]$	$\epsilon(\text{eV}) = 0.0061657$ $\sigma(\text{\AA}) = 2.7577770$	Ow - Ow ⁶⁶	Lennard-Jones $V_{ij}(r_{ij}) = 4\epsilon \left[\left(\frac{\sigma}{r_{ij}} \right)^{12} - \left(\frac{\sigma}{r_{ij}} \right)^6 \right]$	$\epsilon(\text{eV}) = 0.0067386$ $\sigma(\text{\AA}) = 3.165541$
Na - Os ⁶⁶	Lennard-Jones $V_{ij}(r_{ij}) = 4\epsilon \left[\left(\frac{\sigma}{r_{ij}} \right)^{12} - \left(\frac{\sigma}{r_{ij}} \right)^6 \right]$	$\epsilon(\text{eV}) = 0.0061657$ $\sigma(\text{\AA}) = 2.7577770$			

Table 9. ClayFF intermolecular interactions - Continued^{(a),(b)}

^(a) Combining rules were used to calculate constants for all intermolecular LJ potential.

^(b) Octahedral Calcium was used from Ref. ⁶⁶.

Species	Interaction	Parameters	Cutoff (Å)
Oh - Hh ^{94(a)}	Morse Potential $V_{ij}(r_{ij}) = D_{ij} \left\{ \left[1 - e^{(-a_{ij}(r_{ij}-r_{ijo}))} \right]^2 - 1.0 \right\}$	$D_{ij}(\text{eV}) = 5.7347177$ $a_{ij}(\text{Å}^{-1}) = 2.1350$ $r_0(\text{Å}) = 0.9572$	NA
Si - Oh - Hh ^{95(b)}	Three-Body Interaction $V_{ijk}(r_{ijk}) = \frac{1}{2} k_{ijk} (\theta_{ijk} - \theta_o)^2$	$K_{ijk}(\text{eV/rad}^2) = 1.30089$ $\Theta_0(\text{rad}) = 100.00$	1.8
Ca - Oh - Hh ^{95(b),(c)}	Three-Body Interaction $V_{ijk}(r_{ijk}) = \frac{1}{2} k_{ijk} (\theta_{ijk} - \theta_o)^2$	$K_{ijk}(\text{eV/rad}^2) = 0.520356$ $\Theta_0(\text{rad}) = 109.4700$	2.8
Ow - Hw ^{66(b)}	$V_{ij}(r_{ij}) = \frac{1}{2} k_b (r_{ij} - r^o)^2$	$k_b = 48.0546 \frac{\text{eV}}{\text{Å}^2}$ $r^o = 1.0 \text{ Å}$	NA
Hw - Ow - Hw ^{66(b)}	$V_{ijk}(r_{ijk}) = \frac{1}{2} k_a (\theta_{ijk} - \theta_o)^2$	$k_a = 3.96914 \frac{\text{eV}}{\text{rad}^2}$ $\theta_o = 109.47$	NA

Table 10. ClayFF intramolecular (bonded) interactions

^(a) Value from the tri-octahedral clay type was selected.

^(b) The value for K from the paper must be multiplied by 2 to equate the forms of the harmonic potentials (paper vs. DLPOLY).

^(c) K for Ca - Oh - Hh was taken from the values for Mg - Oh - Hh from Ref. ⁹⁵ & Θ_0 is taken from Ref. ⁶⁶.

3.3. Simulation Details

In the next three subsections, we detail the steps followed and the parameters required to run structure optimization and molecular dynamics simulations. The first subsection describes the energy minimization simulation carried out on the (2 x 1 x 1) undoped tobermorite 14Å structure at a temperature of 0K to test and validate the combined interatomic potentials used in this work. This subsection is followed by the details of the long (3 ns) structure relaxation MD simulations done at finite temperature (300K) on both the undoped and the 5% Na doped tobermorite 14Å bulk solid structures. This second structure relaxation was carried out on the (6 x 4 x 1) supercell using both the interatomic interactions described in this work and the rigid partial charge force field ClayFF⁶⁶ to compare the reproduced cell vectors from both models. Finally, in the third subsection, we mention the details of the long (12-17 ns) MD production simulations used to analyze the interfacial systems.

3.3.1. Energy Minimization at 0K.

Before duplicating the tobermorite 14Å into the 6 x 4 x 1 supercell and before doping with Na⁺ ions or running any MD simulations, it is essential to structurally optimize our molecular model, which is the 2 x 1 x 1 supercell with fixed half occupied sites, at a temperature of 0K. Another utility of this structure optimization is to validate the combination of the interatomic potentials used in this work against experimentally known properties of the tobermorite 14Å. This benchmarking study was done using GULP code.⁹⁶ Input files for the GULP code can be found in **Appendix A**.

This structure minimization process is composed of 3 steps: first, the 2 x 1 x 1 supercell lattice parameters were optimized using the default Newton Raphson algorithm implemented in GULP. Then, the rational function optimization (RFO) minimizer was used to accelerate the

minimization when the gradient norm value fell below 0.05. This minimization was done at constant pressure where lattice parameters are free to change independently. The second step was to run a short MD simulation using GULP at 300K using the Nosé-Hoover thermostat and at a constant number of particles, volume, and temperature (NVT) for 15 ps. The first 5 ps are for equilibration without any trajectory recording. The last 10 ps are for production, where ions' trajectories were recorded every 1 ps so that we have 10 snapshots in total. Finally, the third step was to quench and optimize these 10 snapshots again at 0K and zero pressure. Values for lattice parameters and mechanical properties are averaged for each of the 10 minimizations. Final results for this benchmarking study and their corresponding values in literature^{97,98} can be found in **Table 11** and **Table 12**.

The motivation behind taking 10 samples for structural minimization is that there is no unique arrangement for the ultra-confined water molecules in the interlayer regions between the solid calcium-silicate layers. Instead, water molecules can rotate, diffuse and break or form new hydrogen bonds dynamically. Molecular dynamics simulations at finite temperature allow the water molecules to exhibit different arrangements with time. Multiple structures based on different water arrangements can better reproduce the intrinsic properties of the tobermorite 14Å.³⁷ The relaxation time for the thermostat was 1 ps, and all other parameters and interatomic potentials used are the same as the long MD simulations, which are explained thoroughly in the next subsection.

The results in **Table 11** and **Table 12** show that the combination of the interatomic potentials was able to reproduce the lattice vectors of the experimentally determined structure with a relative error ranging from 0.22% to 1.43%, as shown in **Table 11**.³⁷ Moreover, these potentials can reproduce mechanical properties such as the young's modulus, the bulk modulus, the shear

modulus, and basic trends of the elastic constant with a relatively good agreement, as shown in **Table 12.**^{97,98} Besides the mentioned values obtained from experimental and ab initio calculations, the results obtained from this study are very similar to the mechanical properties calculated for tobermorite 14Å from a similar 0K minimization using ReaxFF force field.⁹⁹

2x1x1 supercell	Literature ^{(a)37}	0K Minimization study ^(b)	Absolute Relative Error %
a (Å)	13.47	13.44	0.22
b (Å)	7.43	7.34	1.21
c (Å)	27.99	28.08	0.32
Alpha	90	90.97	1.08
Beta	90	88.71	1.43
Gamma	123.25	122.79	0.38
Volume (Å ³)	2340.86	2325.73	0.65

Table 11. Lattice vectors for the (2 x 1 x 1) undoped tobermorite 14Å supercell compared to that reported in the original paper.³⁷

2x1x1 supercell	Literature	0K Minimization study			Absolute Relative Error %
Young's Modulus (GPa)	51.9 ^{(c),(d)100}	X	Y	Z	6.45 ^(e)
		73.04	78.87	55.25	
Bulk Modulus (GPa)	47±4 ^{(f)98}	45.34 ^(d)			3.53
	35.91 ^{(c),(d)100}				26.26
Shear Modulus (GPa)	20.61 ^{(c),(d)100}	23.94 ^(d)			16.15
Static Dielectric Constant	N/A	XX	YY	ZZ	NA
		4.77	5.07	5.46	
Elastic Constant (C ₁₁)(GPa)	77.6 ^{(c)100}	95.18			22.65
Elastic Constant (C ₂₂)(GPa)	104.5 ^{(c)100}	103.6			0.87
Elastic Constant (C ₃₃)(GPa)	32.05 ^{(c)100}	51.1			59.44
Elastic Constant (C ₄₄)(GPa)	24.5 ^{(c)100}	24.62			0.48
Elastic Constant (C ₅₅)(GPa)	14.65 ^{(c)100}	14.3			2.37
Elastic Constant (C ₆₆)(GPa)	38.1 ^{(c)100}	38.44			0.9

Table 12. Mechanical properties obtained from GULP for the undoped tobermorite 14Å compared to that found in the literature.

^(a) Values are multiplied by 2 in the \vec{a} vector.

^(b) These are average values over 10 samples.

^(c) Values obtained from DFT calculations.

^(d) Reuss–Voigt–Hill Average.

^(e) Error calculated from young's modulus in the z-direction.

^(f) Values obtained from experimental measurements.

3.3.2. Finite Temperature Molecular Structure Equilibration

In this work, long MD simulations at 300K were initially done using DLPOLY 4¹⁰¹. Then we switched to DLPOLY classic¹⁰². Input files for the DLPOLY 4 can be found in **Appendix B**. Regarding the number of particles in our systems; we have 3360 particles (including cores and shells as separate entities) for the undoped tobermorite 14Å and 3384 particles for the 5% Na-doped tobermorite 14Å bulk solids without any additional interfacial water molecules. On the other hand, for systems with additional interfacial water molecules and inserted Na⁺ and Cl⁻ ions, we have 7808 particles for the undoped tobermorite 14Å interface and 7832 particles for the 5% Na-doped tobermorite 14Å interface. MD simulations in this work can be classified into two types: structure equilibration done to the bulk solid tobermorite without cleaving the (001) surface and adding any interfacial water molecules, and production simulations done for both the solid bulk structures and the interfacial structures after cleaving the (001) surface and adding the interfacial water molecules. In this subsection, we only discuss structure equilibration simulations, while in the next subsection, we discuss the production simulations.

Firstly, structure equilibration MD simulations were done for the duplicated (6 x 4 x 1) bulk solid supercells for 3.1 ns using the constant number of particles, stress, and temperature (NST) ensemble. During the first 0.1 ns, the temperature was controlled using the velocity rescaling algorithm in DLPOLY with a scaling frequency of 10 timesteps. For the next 3 ns, the temperature was controlled using the Berendsen thermostat with a relaxation time of 0.5 ps. Additionally, and for the entire 3.1 ns, the stress with controlled through Berendsen barostat with a relaxation time of 0.5 ps. The reason for equilibrating the solid structures using the NST ensemble over the more familiar constant number of particles, pressure, and temperature (NPT) ensemble is that only the lattice dimensions (a, b and c-vectors) are relaxed in the case of the NPT ensemble.

However, in the NST ensemble, both lattice dimensions (a, b, and c-vectors) and angles (α , β , and γ) are flexible to change independently.

The purpose of this study is to calculate the equilibrated lattice vectors for the two solid bulk systems. For this, the lattice vectors for each system were printed every 100 fs for the last 0.5 ns of the 3.1 ns, where the average of each vector was then computed. For comparison, the same procedures were then repeated using the ClayFF force field.^{66,94,95} The full set of the interatomic interactions used in the ClayFF simulations are shown in **Table 7**, **Table 8**, **Table 9**, and **Table 10** in the previous subsection 3.2.3. The final averaged lattice vectors resulting from the two force fields are compared to each other and to those reported in the original paper.³⁷ Results of the undoped tobermorite 14Å are shown in **Table 13**, and those for the 5% Na-doped tobermorite 14Å are shown in **Table 14**.

Results presented in **Table 13** are for the undoped tobermorite 14Å show that the combination of interatomic potentials used in this work produced lattice vectors that are almost identical to those calculated from the ClayFF force field with a less than 1% error. Additionally, calculated lattice vectors from both force fields are almost identical to the duplicated values of the lattice vectors calculated experimentally in the original paper.³⁷

On the other hand, for the 5% Na-doped tobermorite, results in **Table 14** show that the lattice vectors from the two force fields examined in this work predicted similar cell vectors, except for the angle β . Our adopted force field predicted the angle β to be equal to 89.4°, which is similar to the angle β (90°) predicted from the experimental work for the undoped tobermorite 14Å.³⁷ However, the ClayFF force field predicted that the angle β will increase to be 94°. No results found in literature that examined the effect of doping tobermorite 14Å with Na⁺ ions on the final crystal

lattice vectors. The discrepancy of the angle β calculated from the ClayFF force field for the 5% Na-doped system could be because of the partial charge representation of the ions. Upon Na⁺ doping, there was an excess charge that needed to be distributed on the different ions to maintain charge neutrality for the system, which may have affected the accuracy of the predictions of ClayFF. This problem, however, did not exist in our adopted force field since species are represented by the formal oxidation states. We conjecture that the beta angle predicted by the core-shell model is more accurate, but this is to be validated in future research.

6 x 4 x 1 supercell	0% Na literature ^{(a)37}	0% Na core-shell	0% Na ClayFF	Absolute Relative Error % ^(b)
a (Å)	40.41	40.79	40.64	0.38
b (Å)	29.70	29.33	29.52	0.66
c (Å)	27.99	27.42	27.54	0.45
α (°)	90.00	89.87	90.18	0.34
β (°)	90.00	89.88	89.90	0.02
γ (°)	123.25	122.65	123.14	0.41
Volume (Å ³)	28089.60	27619.12	27668.60	0.18
ρ (g/cm ³)	2.23	2.27	2.26	0.18

Table 13. undoped tobermorite 14Å lattice parameters from 3.1 ns relaxation: our combined interatomic potentials vs. ClayFF and original structure

6 x 4 x 1 supercell	5% Na Core-Shell	5% Na ClayFF	Absolute Relative Error % ^(b)
a (Å)	40.76	40.64	0.30
b (Å)	29.30	29.50	0.67
c (Å)	27.90	27.92	0.05
α (°)	90.99	90.54	0.50
β (°)	89.42	94.10	5.23
γ (°)	122.59	123.14	0.45
Volume (Å ³)	28080.11	27912.13	0.60
ρ (g/cm ³)	2.22	2.23	0.60

Table 14. 5% Na doped tobermorite 14Å lattice parameters from the 3.1 ns relaxation MD: our combined interatomic potentials vs. ClayFF

^(a)Values are multiplied by 6 in the \vec{a} vector & 4 in the \vec{b} vector.

^(b)Absolute relative error is calculated between values obtained from simulations by the force field used in this work and by ClayFF.

3.3.3. Production Simulations

In this subsection, we present the production simulation details for both the solid bulk (6 x 4 x 1) undoped and 5% Na-doped tobermorite 14Å structures and their interfacial systems after cleaving, hydrating, and inserting Na⁺ and Cl⁻ ions in the (001) interlayer surface. The reason for running MD simulations for the solid systems in the NVT ensemble is to ensure that these systems are equilibrated and stable enough to be used before cleaving the surface.

Firstly, after the solid structures were relaxed using the NST ensemble, the final averaged cell vectors for solid bulk systems were then used to run production simulations using the Nosé-Hoover NVT thermostat for 2.1 ns. The 1st 0.1 ns is a rescaling period, while the next 2 ns are used for production. During this step, we were able to deduce that increasing Na⁺ ions concentration beyond 5% in the non-defected tobermorite 14Å is not possible to be modeled using classical force field MD simulations, as mentioned earlier. Additionally, properties such as the core-shell analysis (section 3.2.1.) and the vibrational density of states of water molecules in the tobermorite 14Å supercell (section) are calculated from these solid structures simulations.

On the other hand, the primary MD simulations are done after cleaving and hydrating the (001) surface. The two interfacial systems were once again equilibrated using the NVT ensemble and the Berendsen thermostat for 400 ps, out of which 200 ps were temperature rescaling. The next step was to insert the 13 Na⁺ & 13 Cl⁻ ions into the pore and re-equilibrate the system for another 400 ps using the same previous procedure. The reason for equilibrating the interfaces using the NVT ensemble instead of the NST ensemble is that the larger additional water volume is more susceptible to deformation from shear stresses resulting from relaxing the surrounding solid layers using the fixed stress NST ensemble.

Finally, production simulations for the two interfacial systems: the undoped tobermorite 14Å and the 5% Na-doped tobermorite 14Å, were done using the true Nosé-Hoover thermostat and the NVT ensemble. The first production simulations were for 4.1 ns: the 1st 0.1 ns is temperature rescaling, followed by 1 ns production without recording atoms' trajectories for extra structure relaxation, and finally, atoms' trajectories were recorded during the last 3 ns. This was followed by 3 x 3.1 ns production simulations for each system (the 1st 0.1 ns is always a temperature rescaling period). Simulations were done sequentially where the last frame of a certain simulation is the initial configuration of the next one. In addition to these simulations, an additional 5.1 ns production simulation was done for the 5% Na-doped tobermorite 14Å interface. Finally, and in total, 12 ns production simulation trajectories were recorded for the undoped tobermorite 14Å interfacial system and 17 ns for the 5% Na-doped tobermorite 14Å interfacial system.

For MD simulations' details, we used a timestep of 0.1 fs. This small, and hence more computationally expensive, is the only downfall for the core-shell representation. We needed to choose this rigorous timestep to capture the very rapid oscillations of the satellite shell with a relatively small mass. All simulations were done at a 300 K temperature and zero pressure. Trajectories were recorded every 1000 timesteps (100 fs). Moreover, for calculating the electrostatic forces in the reciprocal space, we used an Ewald precision of 1.0×10^{-7} . We also used a cutoff of 11Å for both the electrostatic forces calculations (in the real space) and the short-ranged Van Der Waals interatomic interactions. For the numerical integrator used in the MD codes, we used the Velocity-Verlet algorithm in both the DLPOLY classic and the DLPOLY 4.

On the other hand, in the canonical NVT ensembles, it is expected to have an energy drift. This drift is because systems' energies are allowed to change in this ensemble due to the nature of the external heat bath it is connected to, which controls the temperature of the simulation. Instead,

in the NVT ensemble, the Helmholtz free energy is the parameter to be kept constant.¹⁰³ However, energy drift for MD simulations run using the NVT ensemble should still be calculated. If the drift increased rapidly, this could indicate an intrinsically unstable system, resulting in a simulation crash if the simulation is allowed to run for longer. In all our simulations, the energy drift calculated was in the range of 2.6×10^{-6} to 5.9×10^{-5} eV/ps.atom, which agrees very well with values previously reported in the more rigorous ab initio DFT calculations.¹⁰⁴⁻¹⁰⁶

3.4. Postprocessing Tools

In this subsection, we present the tools used to analyze the structural, energetic, and dynamic properties of the simulated interfacial structures. Firstly, we present the density profiles and contour plots to examine different species' structure properties and adsorption mechanisms on solid surfaces. This is then followed by calculating the adsorption free energy profiles to examine the adsorption and desorption energies. Finally, we present different time correlation functions used to calculate the diffusion coefficient, vibrational density of states (power spectra), and residence time of different species. All properties were calculated separately for each simulation and then averaged.

3.4.1. Density profiles & Contour plots

To understand the structural properties of different solid species near to the interface (such as solid Ca^{2+} ions in both systems and solid Na^+ ions in the 5% Na-doped tobermorite system) and to determine where exactly water and solvated ions (Na^+ and Cl^-) get adsorbed, the 1-D density profiles in the z -direction (c -vector) and perpendicular to the surface were calculated. These profiles were calculated by dividing the length of the c -vector of the simulation cell into bins. Then the number of the examined ions in each bin was calculated and averaged over the total number of ions and the number of examined frames.

Moreover, 2-D contour plots that reflect the density of different solid and solvated species parallel to the surface were also calculated. In this case, however, the area of the xy -plane (same as ab -plane) was divided into 2-D bins, and the number of ions in each bin was similarly computed. The 2-D contour plots were calculated for species near the surface only, which was done by applying a cutoff of 10-12Å in the z -direction. This cutoff is equivalent to the nearest two water layers from the surface, deduced from the 1-D water molecules density profile. An example of the

C++ script used to calculate the 2-D contour plots is provided in **Appendix C**. Moreover, the full description of water layering and the boundaries of each layer are discussed in the results section.

It is also important to mention that the density profiles for water molecules were calculated based on the location of the oxygen ions. Moreover, and while the 1-D and 2-D profiles for all species reflect a number density (arbitrary unit: a.u.), the 1-D density profiles of water molecules were multiplied by the true bulk density of water (1 g/cm³). This representation reflects the evolution of water density away from the influence of the solid surface in a way that is comparable to the true bulk water density.

3.4.2. Adsorption Free-Energy calculations

Calculating the free-energy of adsorption (the potential of mean force) from molecular dynamics trajectories can be done directly from the 1-D density profiles (ρ_z), as shown in **Equation 4**, of ions perpendicular to the surface if all adsorption events are taken into consideration and well sampled.¹⁰⁷ In other words, if the processes of adsorption and desorption of ions near the surface are fast compared to the length of the simulation.¹⁰⁸ Adsorption free energy profiles explain the thermodynamics of the adsorption process and whether there is an energy gain from the adsorption or an energy barrier for the desorption of a specific ion on the examined surfaces. Moreover, these profiles explain if there is preferential adsorption of specific ions on the examined surfaces. In **Equation 4**, K_B is the Boltzmann constant, and T is the temperature in K.

$$W(r) = -K_B T * \ln(\rho_z)$$

Equation 4. Adsorption free energy

3.4.3. Mean Square Displacement & Diffusion Coefficient

The influence of the solid substrate of both the undoped tobermorite 14Å and 5% Na-doped tobermorite 14Å on the dynamics of solvated Na⁺ and Cl⁻ ions and water molecules at different distances from the interface can be investigated by calculating the diffusion coefficient. The 3-D mean square displacement (MSD) (**Equation 5**), where $r_i(t)$ is the position of the ion i at time t , and the Einstein relation (**Equation 6**) are used to calculate the diffusion coefficient for these ions.

Time correlation functions, such as the MSD, are invariant under time conditions. Therefore, it is crucial to sample the calculations using multiple origins as references to improve the statistics of the calculations. One frame was used as an origin for every 100 saved frames (10 ps since our sampling frequency is 100 fs). The MSD was then averaged over the total number of origins, the total number of frames, and the total number of ions in the considered water volume. For example, when calculating the diffusion coefficient of water in a specific water layer at a specific height from the interface, the number of water molecules in this layer was computed for each frame and then averaged over all frames. On the other hand, for Na⁺ and Cl⁻ ions, the diffusion coefficients for these ions were calculated over the entire water volume in the pore, which indicates that the number of ions is always 13 in this case. After calculating the mean square displacement, it was then plotted vs. time and fitted to a linear plot. The slope of the linear fit was calculated and divided by two multiplied by the number of dimensions ($n=3$) and the simulation time used to calculate the diffusion coefficient, **Equation 6**. An example of the C++ script used to calculate the MSD is provided in **Appendix C**.

$$MSD(t) = \langle |r_i(t) - r_i(0)|^2 \rangle$$

Equation 5. 3-D Mean square displacement

$$D = \frac{MSD}{2nt}$$

Equation 6. Einstein diffusion equation

3.4.4. Velocity Autocorrelation Function (VAF) and Vibrational Density of States (VDOS)

The vibrational density of states (VDOS), also known as the power spectra, was calculated for different types of water molecules; bulk liquid, ultra-confined in bulk solid tobermorite 14Å, and at the interface. VDOS was calculated by applying the Fourier transform to the velocity autocorrelation function (VAF).¹⁰⁹ The VAF was calculated using **Equation 7**, where $\vec{V}_i(t)$ is the velocity of the ion i at time t . VAF is another time correlation function calculated based on the multiple origins scheme illustrated earlier. The VDOS was calculated based on **Equation 8**, where ω is the characteristic frequencies' modes of vibration of the water molecule.

VAF and VDOS can be calculated for either the hydrogen or the oxygen ions of water molecules. However, in this work, we calculated the VDOS of water molecules from the velocities of the hydrogen ions because this results in clearer shifts in the O-H stretching range of frequencies, which is the important range for our analysis. More on the physical interpretation of different ranges of frequencies will be explained further in the results section.

It is also important to mention that VAF calculations for water molecules were calculated from separate simulations for bulk liquid water, bulk solid undoped tobermorite 14Å, and both of the interfacial systems: the undoped and the 5% Na-doped tobermorite 14Å without inserting the additional Na⁺ and Cl⁻ ions. The last frames from the already equilibrated structures were simulated for an additional 300 ps (1st 50 ps are rescaling) for these separate simulations. Only the last 250 ps trajectories were recorded with a high printing frequency of 50 timesteps (5 fs). This protocol was

implemented because VAF calculations are more sensitive to the printing frequency and the trajectory evolution than the simulation time for the already equilibrated systems.

$$Z(t) = \frac{\langle \vec{V}_i(t + t_0) \cdot \vec{V}_i(t_0) \rangle}{\langle \vec{V}_i(t_0) \cdot \vec{V}_i(t_0) \rangle}$$

Equation 7. Velocity autocorrelation function (VAF)

$$Z(\omega) = \int_0^{\infty} Z(t) \cos(\omega t) dt$$

Equation 8. Vibrational density of states (VDOS)

3.4.4. Residence Time Correlation Function

The residence time of adsorbed ions near the interface was calculated from the residence time correlation function (TCF) shown in **Equation 9**.¹¹⁰ Again, the same multiple origins scheme discussed earlier was implemented in this calculation. Moreover, an additional criterion was used; if the considered ions left the examined water volume for up to 2 ps and re-entered again, they will still be considered in the calculations as if they never left the examined volume.^{107,110}

In **Equation 9**, N is the total number of ions in the considered water volume. θ_i , on the other hand, is a Heaviside function that takes the value of 1 if the examined atom is within the examined region at time t and 0 if it is elsewhere. Finally, to calculate the residence time, the plot of $R(t)$ vs. t was fitted to an exponential function, shown in **Equation 10**. The residence time was then calculated from the exponential constant ($1/t$). Only the first 100 ps of the TCF were fitted because the statistical error becomes very large at the end of the TCF.

$$\langle R(t) \rangle = \left\langle \frac{1}{N_0} \sum_{i=1}^{N_t} \theta_i(0) \theta_i(t) \right\rangle$$

Equation 9. Residence Time Correlation Function (TCF)

$$y = m * e^{-t*x} + b$$

Equation 10. The exponential function used to fit the TCF

Chapter 4. Results and Discussion

This section presents the results calculated for the undoped and the 5% Na-doped tobermorite 14Å interfacial systems. We first in section 4.1. describe the structural properties of different interfacial species calculated using the 1-D and the 2-D density profiles. Next, in section 4.2., we present the adsorption energetics for the solvated Na⁺ and Cl⁻ ions on both surfaces. Finally, in section 4.3. we thoroughly discuss the dynamics properties of the interfacial water molecules and the solvated Na⁺ and Cl⁻ ions.

4.1. Structural Properties

4.1.1. Water Molecules and Solvated Ions 1-D Density Profiles

The first step to analyze the surface effect of both surfaces on the adsorption characteristics of solvated species is to examine their structural properties near the interface. For that purpose, we plotted the 1-D density profiles for the water molecules (solid red line) and the solvated Na⁺ (dash-dotted orange line) and Cl⁻ (solid black line) ions in the direction perpendicular to the surface (z-direction) of the undoped tobermorite 14Å (**Figure 11a**) and the 5% Na-doped tobermorite 14Å (**Figure 11b**). Moreover, we plotted the 1-D density profiles for the outermost Ca²⁺ ions (dashed blue line) at the surface of the solid structure for the two systems. It is also important to mention that in the case of the 5% Na-doped tobermorite 14Å (**Figure 11b**), the Na⁺ ions (dash-dotted orange line) 1-D density profile includes the three solid Na⁺ ions from each surface that were originally Ca²⁺ ions and existed in the interlayer space before doping and cleaving the (001) surface. This larger number of Na⁺ ions explain the higher Na⁺ and lower Ca⁺ ions' peaks in the case of 5% Na-doped tobermorite 14Å in **Figure 11b** than those in the undoped tobermorite 14Å, as shown in **Figure 11a**.

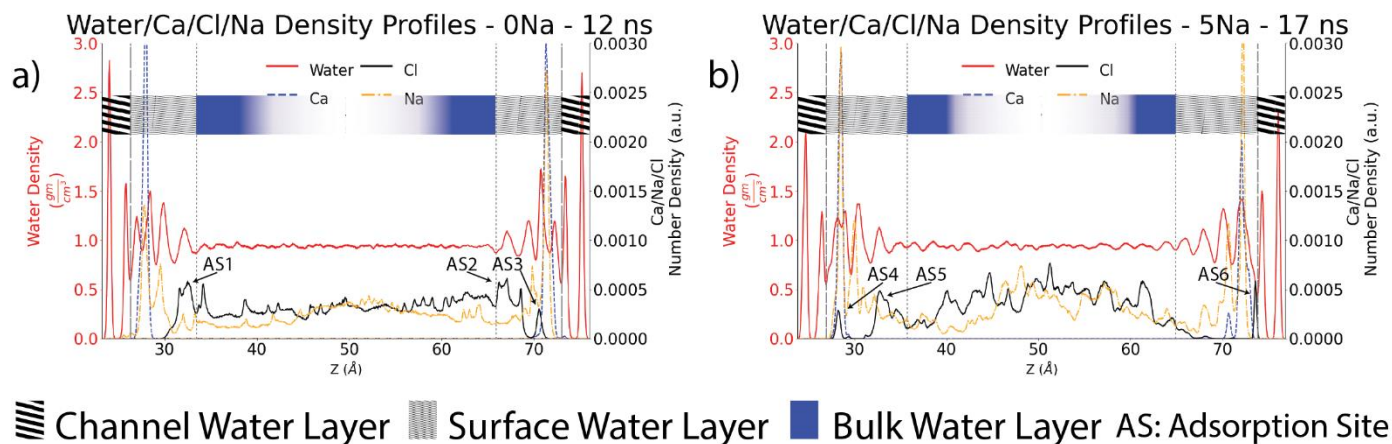


Figure 11. 1-D density profiles for the undoped and the 5% Na-doped interfacial systems. 1-D mass density profiles of water (red) on the left y-axes and number density profiles of Ca (blue), Na (orange) & Cl (black) on the right y-axes. Vertical dashed and dotted lines in (a) & (b) are the upper boundaries of the channel layers (represented by thick tilted black lines) and surface layers (represented by light tilted black lines), respectively. The bulk layer is represented by solid blue color.

From the 1-D density profiles of water molecules of both systems (red lines in **Figure 11a and b**), we were able to divide the volumes of the two pores into three different layers: channel layer, surface layer, and bulk layer based on the change of the 1-D density as a function of the distance from the surface. This variation in water density results from the strong interactions and hydrogen bond network formed between the interfacial water molecules and the different solid species on the surface, such as calcium, sodium, and oxygen ions.

Water molecules closest to the surface in the first layer (channel layer) of both structures have very large oscillations in the calculated density, indicating an almost glass-like ordered structure. Again, this structural arrangement results from the hydrogen bond network being the strongest at the two hydrophilic surfaces examined: the undoped tobermorite 14Å and the 5% Na-doped tobermorite 14Å. This channel water layer in both systems corresponds to the first two water molecules in the pore that exists in the natural grooves formed by the bridging silicates (**Figure 12e**). As the distance from the surface increases, these oscillations in the water density profiles

become more damped, forming the second layer, which is defined as the surface layer. In this layer, the strength of the hydrogen bond network formed at the surface starts to gradually decrease. This layer is defined from the upper boundary of the channel layer to the distance where the oscillations of water density converge to 1 g/cm^3 , and it resembles the transition from the glass-like water structure at the surfaces to the bulk liquid-like water at the middle of the pore. Finally, the bulk layer is defined as the region between the two surface layers where the density of water is almost equal to 1 g/cm^3 . The convergence of the calculated water density indicates that the previously discussed water layers have completely screened the influence of the strong hydrogen bond network formed at the surface and that it is now similar to the one formed between water molecules in liquid water away from the surface influence.^{21,22}

Comparing the two examined structures, the thicknesses of the channel layer, the surface layer, and the bulk layer for the undoped tobermorite 14\AA are 3\AA , 7.1\AA , and 32.5\AA , respectively. For the 5% Na-doped tobermorite 14\AA , the thicknesses for these layers are 3\AA , 8.8\AA , and 29.3\AA , respectively. The discrepancy between the thickness of the surface layer in the two systems indicates a stronger influence for the surface of the 5% Na-doped tobermorite 14\AA on the density and the arrangement of the interfacial water molecules up to a larger distance away from the surface. Another observed characteristic of the water density profile in the 5% Na-doped tobermorite 14\AA (red line in **Figure 11b**) is that there are more fluctuations at the middle of the pore (bulk layer) than in the undoped tobermorite 14\AA system (red line in **Figure 11a**). These larger fluctuations indicate a degree of order and structural arrangement in this system (the 5% Na-doped tobermorite 14\AA) is maintained throughout the long simulation interval. This structural arrangement is the first indication of this system's intrinsic slower dynamics property, examined and explained thoroughly in the dynamics subsection of this thesis.

This larger thickness of the surface layer and maintained larger fluctuations of water density in the 5% Na-doped system could be explained in terms of the different solid species on the surface of this system compared to the undoped system. In the undoped tobermorite 14Å surface, we have 12 Ca²⁺ ions strongly bonded to each surface. However, in the 5% Na-doped tobermorite 14Å, we have 9 Ca²⁺ ions and 3 Na⁺ ions on each surface. These Na⁺ ions are not as strongly bonded to the surface as the Ca²⁺ ions and can diffuse a bit further from the surface, which can be seen from the more numerous and intense peaks of Na⁺ ions and also their presence further from the surface (orange lines in **Figure 11a and b**). Moreover, on the surface of the 5% Na-doped tobermorite 14Å, six additional hydroxyl groups exist resulting from the charge balancing and cleaving mechanisms mentioned in the methods section. These variations indicate the possibility of a stronger bonding scheme formed at the surface of the 5% Na-doped tobermorite 14Å and explain the increase in the surface layer thickness in this system.

As mentioned earlier in the methods section, the additional 13 Na⁺ and 13 Cl⁻ ions were initially positioned at the middle of the pore. However, after running simulations for 12 ns for the undoped tobermorite 14Å interfacial structure and 17 ns for the 5% Na-doped tobermorite 14Å interfacial structure, these Na⁺ and Cl⁻ ions were able to diffuse into the surface of the solid structures. In the undoped tobermorite 14Å shown in **Figure 11a**, we notice that the Na⁺ ions (dash-dotted orange line) can get adsorbed closer to the solid substrate than the Cl⁻ ions (solid black line). This preferential adsorption of Na⁺ ions on the negative surface of the tobermorite 14Å agrees very well with the same observation of the adsorption of positive and negative ions on different tobermorite structures in previous studies.^{20,22,25,29} While the same observation holds for the 5% Na-doped tobermorite 14Å shown in **Figure 11b**; there exists multiple narrow peaks of Cl⁻ ions that are as close as and sometimes closer than the Na⁺ ions peaks near the surface, which

indicates rare but very stable adsorption events that resulted from doping the tobermorite 14 Å with 5% Na⁺ ions.

Additionally, to study and differentiate between the different adsorption sites (AS) and mechanisms for Cl⁻ ions on both systems, the locations of 3 different Cl⁻ peaks nearest to the surfaces of the two systems are labeled to be examined later. It is important to note that these peaks do not necessarily represent one adsorption site; rather, they may originate from one or multiple sites with the same distance from the surface. For the undoped tobermorite 14Å surface shown in **Figure 11a**, the three nearest peaks corresponding to three adsorption sites are labeled AS1, AS2, and AS3. Similarly, for the 5% Na-doped tobermorite 14Å shown in **Figure 11b**, the three nearest peaks from the surface are labeled AS4, AS5, and AS6. These adsorption sites will be examined thoroughly using the 2-D contour plots discussed in the next subsection.

4.1.2. 2-D Contour Plots

In addition to the 1-D density profiles, we generated the 2-D contour plots for different solid and solvated species in both the channel and surface water layers only and not the full pore width. The purpose of this analysis is to have a 2-D representation of the interface in the xy-plane and to know where the solvated Cl⁻ ions get adsorbed on any of the surface cations: Na⁺, Ca²⁺, Si⁴⁺, or H⁺ of the surface OH⁻ groups. The contour plots for the lower and upper surfaces of the undoped tobermorite 14Å are shown in **Figure 12a and b**, respectively, while those for the 5% Na-doped tobermorite 14Å are shown in **Figure 12c and d**, respectively. In each of the four plots, the 2-D contour plots for Cl⁻ ions (solid black lines), Na⁺ ions (solid orange lines), Ca²⁺ ions (solid blue lines), Si⁴⁺ ions (solid green lines), and the H of the hydroxyl groups (H-OH) (solid red lines) are shown. The first thing to notice from the contour plots of all species in the 5% Na-doped tobermorite 14Å is that the lines representing the atomic densities in the xy-plane are more

localized and concentrated than the more dispersed lines of the undoped system. This observation is the second indication of the intrinsic slower dynamics of all examined ions on the surface and ions solvated in the 45Å pore (Na^+ and Cl^-) of the 5% Na-doped tobermorite system when compared to the undoped system. Further, it confirms the same observation of the slow dynamics of water molecules from the 1-D water density profiles discussed in the previous subsection for the 5% Na-doped system.

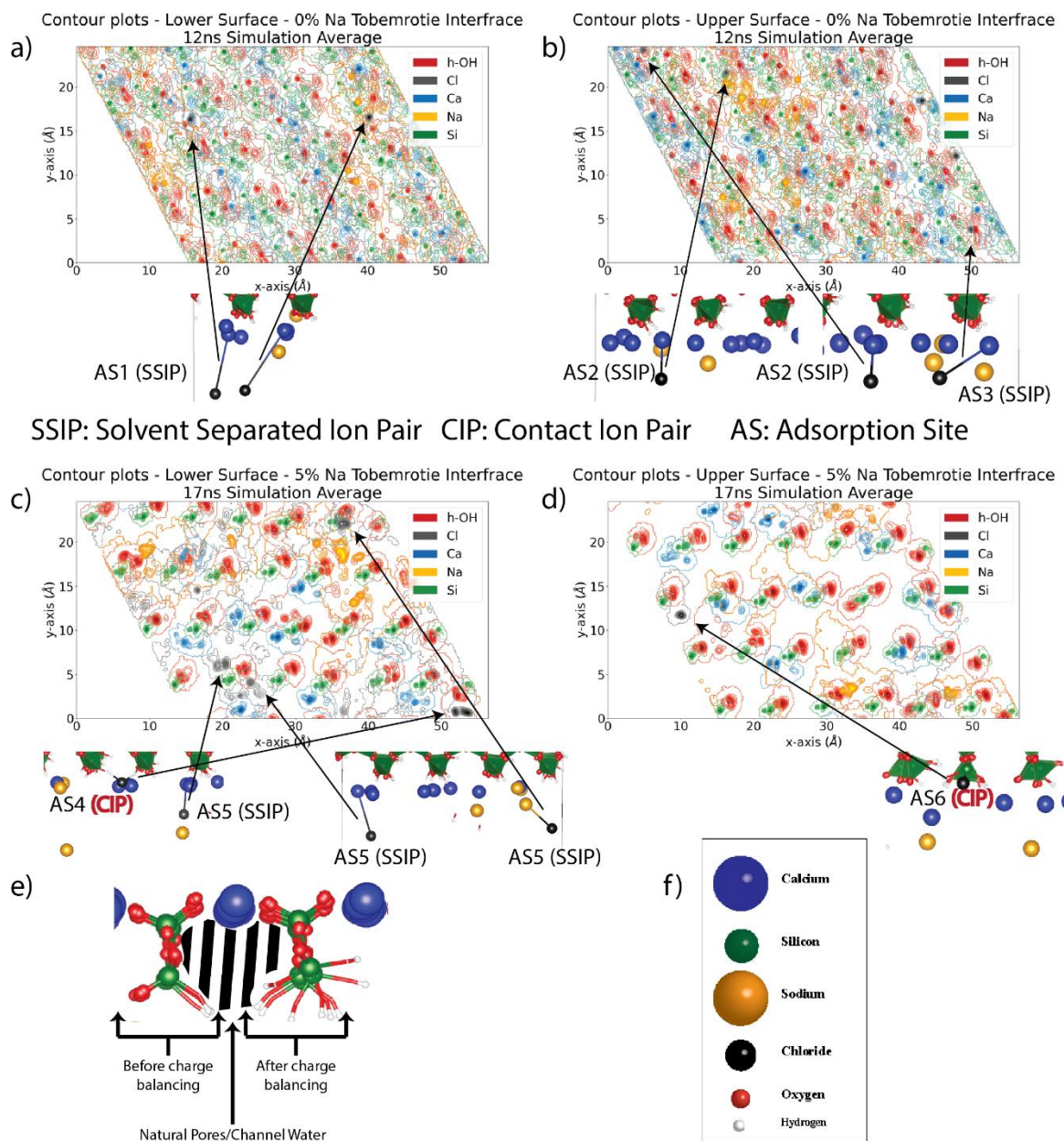


Figure 12. 2-D contours plots for the undoped and the 5% Na-doped interfacial. (a) and (b) 2-D contour plots of the lower and upper surfaces of the undoped system, respectively. (c) and (d) 2-D contour plots of the lower and upper surfaces of the 5% Na-doped system, respectively. Below the contour plots are the atomistic visualizations for different adsorption sites: AS1-6. In each plot, Ca^{2+} is represented by solid blue lines, Si^{4+} is represented by solid green lines, Na^+ is represented by solid orange lines, Cl^- is represented by solid black lines, and H^+ of OH is represented by solid red lines. Arrows from the atomistic visualizations to the contour plots represent the Cl^- ions adsorbed (thick circular black lines). (e) Natural surface pores with channel water represented by the dashed thick black lines and the effect of the charge balancing mechanism on the bridging silicates exposed to the surface and the hydrogenation of dangling oxygens are shown. (f) Color legend for different atomic species. All atomic snapshots are for the cleaved upper surface (water is below and around the shown solid species but removed for figure clarity).

After a detailed inspection of each simulation individually, we matched the adsorption sites labeled in the 1-D density profiles from the previous subsection and the 2-D contours plots for each of the two systems. By doing this, we can examine the adsorption mechanism of Cl^- ions on both surfaces exactly. The adsorption sites AS1, AS2, and AS3, labeled in **Figure 11a**, are shown in **Figure 12a and b** for the undoped tobermorite 14\AA surface. Moreover, the atomistic visualizations for each of these adsorption sites are shown in **Figure 12a and b**. Similarly, the adsorption sites AS4, AS5, and AS6 are also shown in **Figure 12c and d**, along with the atomistic visualizations. In addition to highlighting where Cl^- ions get adsorbed for the two systems, this analysis also enabled us to differentiate between different adsorption mechanisms: either directly coordinated to the surface species in a contact ion pair (CIP) adsorption or separated from the surface species with water molecules in a solvent separated ion pairs (SSIP) adsorption.

For the undoped tobermorite 14\AA interface, we can deduce from **Figure 12a and b** and the atomistic visualizations of the three adsorption sites: AS1, AS2, and AS3, that the Cl^- ions (solid black lines) adsorption mechanism is only SSIP. For these adsorption sites, Cl^- ions were associated with either the Ca^{2+} ions that originally existed on the surface or with the Na^+ ions that are adsorbed from the middle of the pore. However, no Cl^- ions were directly coordinated (CIP adsorption) with any surface cations from the surface for the 12 ns simulation interval. This low binding capacity of Cl^- ions to the surface of the tobermorite 14\AA agrees well with previous studies that computationally examined the adsorption of Cl^- on the surfaces of tobermorite structures.^{20,22,23,25,27} Moreover, this was also noticed experimentally during the work of Yu and Kirkpatrick on jennite, which is a similar crystalline structure to tobermorite.¹¹¹

An additional observation from **Figure 12a and b**, specifically from the concentrated solid orange lines and the atomistic visualizations, is that the Na^+ ions once existed in the middle of the pore and are found to be strongly attracted (CIP adsorption) to the tobermorite 14Å surface. This strong selective adsorption of the solvated positive ions further supports the idea that the surface of the tobermorite 14Å has an overall negative charge with localized positive sites of the Ca^{2+} and the H-OH ions. These strong negative charges originate from the dangling oxygen ions attached to the outermost bridging silicates.

For the 5% Na-doped tobermorite 14Å interface, we can notice from the 2-D contour plots shown in **Figure 12c and d** and the atomistic visualization of AS4, AS5, and AS6 that the adsorption mechanisms for the solvated Cl^- ions are a mixture of both the weak CIP and the strong SSIP mechanism. From the visualizations of the adsorption sites, AS4 represents a Cl^- ion directly bonded to two of the surface H-OH ions. For the adsorption site AS6, a Cl^- ion is directly bonded to the Si^{4+} ion of one of the bridging silicates. Both AS4 and AS6 adsorption sites are considered to be strong and stable CIP bonding. However, these two adsorption sites can be considered as rare events since they only occurred once for each type (two out of 13 solvated Cl^- ions). On the other hand, for AS5, multiple Cl^- ions are associated with the surface positive Ca^{2+} and Na^+ ions in the relatively weaker SSIP bonding scheme, which is similar to the adsorption mechanisms of Cl^- ions on the surface of the undoped tobermorite 14Å.

These new CIP adsorption sites for the Cl^- ions on the surface of the 5% Na-doped tobermorite 14Å can be explained in terms of the charge balancing mechanism done after substituting the Ca^{2+} ions with Na^+ ions and the subsequent process of cleaving the interlayer space. Before introducing the Na^+ ions into the structure of the tobermorite 14Å as dopants, the outermost bridging silicate groups are composed of one silicon ion that is attached to three oxygen

ions and one hydroxyl group, which is shown in the left visualization of **Figure 12e**. Two out of the three oxygen ions are shared with two other silicate groups (pair tetrahedra), while the third oxygen ion protrudes into the interface (dangling oxygen). After introducing the 5% Na⁺ ions into the structure of the tobermorite 14Å, the dangling oxygens of the bridging silicate groups that are nearest to the Na⁺ ions were hydrogenated and transformed into hydroxyl groups, which is shown in the right visualization of **Figure 12e**. These bridging silicate groups are now composed of two hydroxyl groups, in the case of the 5% Na-doped system, instead of one hydroxyl group and a dangling oxygen ion, in the case of the undoped system. Thus, the number of the hydroxyl groups on the surface of the 5% Na-doped tobermorite 14Å is now more than the number of hydroxyl groups on the surface of the undoped tobermorite 14Å, which increased the number of the localized positive sites (H-OH) on the overall negative surface (as in the adsorption site AS4). Moreover, it also reduced the repulsion from the dangling oxygen ions allowing for the adsorption of Cl⁻ ions directly on some of the silicon ions (as in the adsorption site AS6). Experimentally, reaction products from alkalic-activated slag were found to be more capable of adsorbing and binding to solvated Cl⁻ ions compared to the hydration products of OPC¹¹² and other types of AACs such as alkali-activated fly ash.¹¹³ Finally, for the Na⁺ ions (solid orange lines in **Figure 12c and d**), we can observe that the adsorption mechanisms of Na⁺ ions on the surface of the 5% Na-doped system are also a mixture between CIP and SSIP.

4.2. Adsorption Energetics of Solvated Na⁺ and Cl⁻ ions

The adsorption and desorption thermodynamics of the solvated Na⁺ and Cl⁻ ions on the surfaces of the undoped and the 5% Na-doped tobermorite 14Å structures can be examined by plotting the adsorption free-energy profiles for these ions (**Figure 13**). These profiles are calculated from **Equation 4** and from the 1-D density profiles of these ions perpendicular to the

surface. For both examined systems, it is important to notice that the free-energy profiles of both the Na^+ and the Cl^- ions exhibit symmetric features. This symmetry indicates that both surfaces are identical regarding the number of different species, surface structure, and energetic favorability. Moreover, this symmetry also indicates sufficient equilibration time and trajectory sampling.

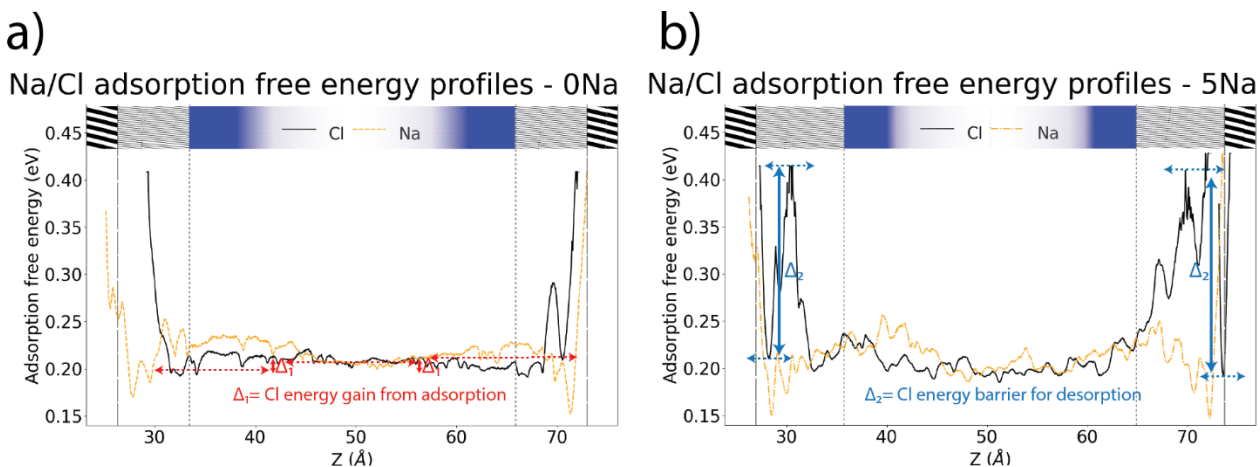


Figure 13. Adsorption free-energy profiles for solvated Na^+ (dash-dotted orange lines) and Cl^- (solid black lines) ions on the surface of the (a) undoped and (b) the 5% Na-doped systems. For illustration, the adsorption free-energy gain for Cl^- ions on the surface of the undoped system is the difference between the energy levels marked by red dashed arrows in (a). The desorption barrier for Cl^- ions on the 5% Na-doped system is the difference between the energy levels marked by blue dashed arrows in (b). For further illustration, the reader is referred back to the text in section 4.2.

	Species	0% Na in Solid	5% Na in Solid
Adsorption energy gain	Na^+	-0.05 eV	-0.05 eV
	Cl^-	$\simeq 0$ eV	$\simeq 0$ eV
Desorption energy barrier	Na^+	0.08	0.1 eV
	Cl^-	0.02 to 0.08 eV	0.2 eV
Adsorption energy barrier	Na^+	0.03 eV	0.05 eV
	Cl^-	0.007 eV	0.2 eV

Table 15. Adsorption energy gain, desorption, and adsorption energy barriers for solvated Na & Cl ions in both the 0% Na & 5% Na systems.

From these profiles, we computed three energies for each adsorbed ion: first, we calculated the energy gain by the system that resulted from the adsorption of this ion. Second, we computed the energy barrier required to desorb it, and finally, we computed the energy barrier required to adsorb it. The magnitude of this energy gain indicates whether the adsorption of these ions is preferred or not. The energy gain from the adsorption of an ion is calculated from the difference between the first energy minimum nearest to the surface and the average energy calculated at the middle of the pore. For illustration, the red dashed arrows shown in **Figure 13a** indicates the different energy level used to calculate the energy gain from the adsorption of Cl^- ions (solid black line) on the surface of the undoped tobermorite 14\AA .

On the other hand, the magnitude of the desorption barrier indicates how stable this adsorption event is and how hard it is for these ions to desorb again into the pore. The desorption barrier for an ion is calculated from the difference between the first energy minimum nearest to the surface and the immediately following energy maximum. Similarly, as shown in **Figure 13b**, blue dashed arrows represent the energy levels used to compute the desorption energy barrier for Cl^- ions (solid black line) on the surface of the 5% Na-doped tobermorite 14\AA system. Finally, and similar to the desorption barriers, the adsorption barriers were calculated based on the difference between the energy at the middle of the pore and the highest peak near the surface. In **Table 15**, we present values for the adsorption energy gain, desorption, and adsorption barriers for each of the Na^+ and Cl^- ions on the surfaces of the undoped and the 5% Na-doped tobermorite 14\AA structures. For both systems, these values are calculated for each simulation separately and then averaged over all simulations.

For the undoped tobermorite 14\AA system, the adsorption energy gain for solvated Na^+ and Cl^- ions are -0.05 eV and 0 eV , respectively. However, the desorption barrier for the Na^+ ions is

0.08 eV, while for Cl^- ions, this value is in the range of 0.02-0.08 eV. For the adsorption barriers, these values are 0.03 eV and 0.007 eV for the Na^+ and Cl^- ions, respectively. For the 5% Na-doped system, the values for the energy gain from the adsorption of solvated Na^+ and Cl^- ions are still the same (-0.05 eV and 0 eV, respectively). On the other hand, the desorption barriers for Na^+ and Cl^- ions have increased to be 0.1 eV and 0.2 eV, respectively. Finally, the adsorption barriers for the two ions are 0.05 eV and 0.2 eV, respectively.

Results from the adsorption energy gain values indicate that, for both systems, Na^+ ions are more preferred to be adsorbed than Cl^- ions (-0.05 eV for Na^+ ions vs. 0 eV for Cl^- ions) on the surfaces of both systems: the undoped and the 5% Na doped tobermorite 14Å. Moreover, it indicates that doping the structure with Na^+ ions did not change this preferential selection or the adsorption thermodynamics of both ions. These results confirm the previous assumption that the surfaces of both the undoped and the Na-doped tobermorite 14Å structures have an overall negative charge that enhances the adsorption of positive ions.

The desorption barriers for Na^+ (0.08 eV) and Cl^- (0.02-0.08 eV) ions on the surface of the undoped tobermorite 14Å further confirms the higher stability of adsorbed Na^+ ions in this system. On the other hand, the increase in the desorption barriers for both the Na^+ (0.1 eV) and Cl^- (0.2 eV) ions on the 5% Na-doped tobermorite 14Å surface indicates that these adsorption sites are more stable than in the case of the undoped surface. Moreover, it also indicates that Cl^- ions adsorption sites, while less preferred, are more stable than Na^+ ions adsorption sites. From the values of the adsorption barriers, the same observation for the more preferential Na^+ ions adsorption can be seen in the 5% Na-doped system when Na^+ ions have a lower barrier (0.05 eV) than Cl^- ions (0.2 eV) and both ions are closely adsorbed on the surface. However, this does not hold for the undoped system where most of the Cl^- ions are still in the middle of the pore and loosely bonded to the

surface. While it seems that the adsorption barrier for the Cl^- ions has increased going from the undoped surface to the 5% Na-doped surface, it is important to note that we are comparing two different adsorption mechanisms: in the undoped system, the dominant adsorption mechanism is the solvent separated ion pair (SSIP), where ions are still relatively far from the surface, while the adsorption mechanism is contact ion pair mechanism (CIP) in the 5% Na-doped system, where Cl^- ions are much closer to the surface.

These results indicate that, while it is still not preferred for the surface of the 5% Na-doped system to adsorb Cl^- ions from the interface, if one of the solvated Cl^- ions get adsorbed during the rare events discussed earlier, it forms a stable bond with the surface cations that is harder to break compared to the bonds formed on the undoped surface. Moreover, these adsorption energetics' results, along with the previous structural results, endorse the idea that alkali-activated cement and the Na^+ ions that are introduced from the alkaline activators may have a very positive effect on the adsorption of solvated corrosive ions such as Cl^- . This effect is represented by the new and very stable adsorption sites created from the charge balancing mechanism of substituting Ca^{2+} with Na^+ ions.

4.3 Dynamic Properties

The next subsections examine the dynamic properties of both the solvated Na^+ and Cl^- ions and the water molecules. Firstly, we discuss the 3-D diffusion coefficient calculated for the different species. We then examine the vibrational density of states and residence time for water molecules.

4.3.1. Diffusion Coefficient

This section discusses the 3-D diffusion coefficients of Na^+ and Cl^- ions and water molecules on the surfaces of both the undoped (red x markers) and the 5% Na-doped (green x markers) tobermorite 14\AA structures and are shown in **Figure 14a**. The diffusion coefficient for all species is calculated based on the 3-D mean square displacement and Einstein equations, as shown in **section 3.4.3**. Again, the diffusion coefficient for each species is calculated from each simulation separately and then averaged over all simulations.

The diffusion coefficients for the Na^+ (orange sphere) and Cl^- (black sphere) ions are calculated based on their locations in the total pore volume. However, the diffusion coefficients of water molecules are calculated based on the location of the oxygen ions and at different distances (layers) from the interfaces: the interlayer space (volume represented by solid black color), the channel layers (volume represented by thick black lines), the surface layers (volume represented by light black lines), and the bulk layer (volume represented by solid blue color). The locations of these different volumes relative to the solid surface are shown in the atomistic visualization of the interface, **Figure 14b**. The channel layer, surface layer, and bulk layer were described earlier in the structural properties subsection. However, the interlayer space represents the volume of ultra-confined water molecules between two calcium-silicate layers. This volume originally existed in

the bulk solid tobermorite structures since we only cleaved one interlayer space out of the original two spaces to produce the interfacial structure.

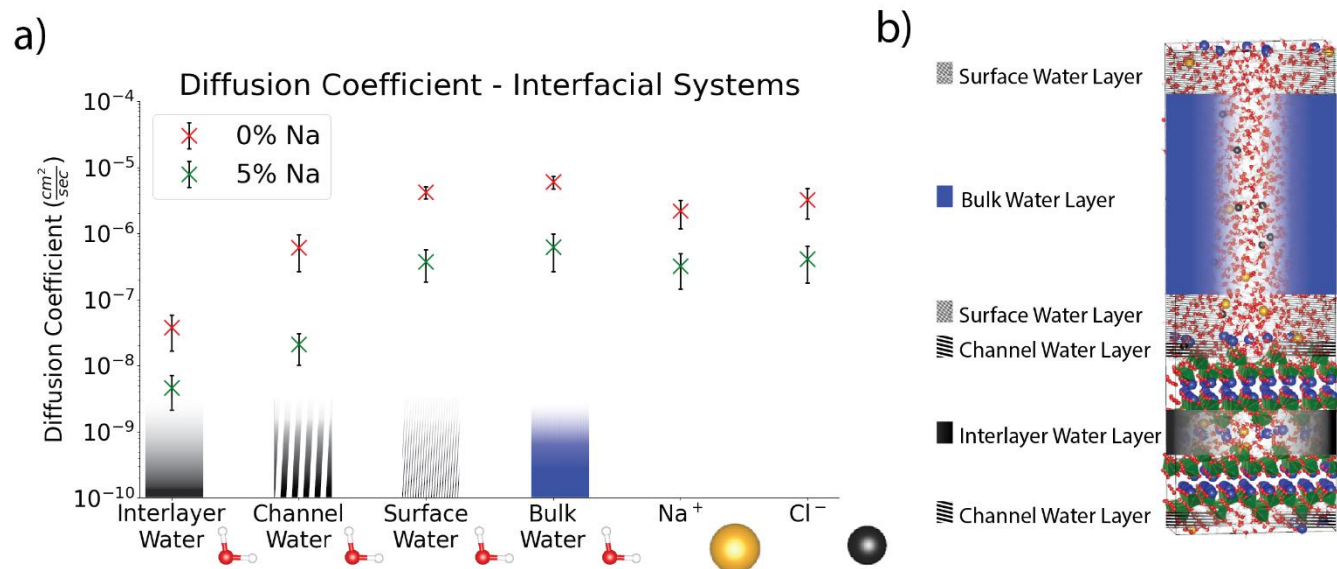


Figure 14. (a) The diffusion coefficients of different species on the surfaces of the undoped (red x markers) and the 5% Na-doped (green x markers) systems. Error bars shown represent the standard deviation calculated from averaging the diffusion coefficient over all simulations. The diffusion coefficients of water molecules at different distances from the surface: the interlayer space (volume represented by solid black color), the channel layers (volume represented by thick and titled black lines), the surface layers (volume represented by light and tilted black lines), and the bulk layer (volume represented by solid blue color) are shown. Moreover, the diffusion coefficients of Na⁺ and Cl⁻ ions in the whole pore volume are also shown. (b) Atomistic visualization of the different examined water layers above and between the solid substrate.

4.3.1.1. Diffusion Coefficient of Water Molecules in Interfacial Systems

The diffusion coefficients of water molecules monotonically decrease as we get closer to the surface for both systems: the undoped and the 5% Na doped tobermorite 14Å structures. The fastest calculated diffusion coefficients for water molecules are at the middle of the pore in the bulk layer: 6.05×10^{-6} cm²/sec and 6.26×10^{-7} cm²/sec for the undoped and 5% Na-doped systems, respectively. These values then decrease to be 4.25×10^{-6} cm²/sec and 3.74×10^{-7} cm²/sec at the surface layers of the two systems, respectively. Moreover, the nearest water volume to the surface (the channel layer) has the slowest diffusion coefficient for water molecules in the entire pore

volume, which are 6.10×10^{-7} cm²/sec and 2.07×10^{-8} cm²/sec for the two systems. Finally, water molecules confined between two solid surfaces in the interlayer space have the slowest dynamics in both systems (less than those in the channel layer) with diffusion coefficients of 3.81×10^{-8} cm²/sec and 4.62×10^{-9} cm²/sec for both systems, respectively.

This systematic decrease in the diffusion coefficients of water molecules as we move towards both the undoped and the 5% Na-doped surfaces (from the bulk layer to the surface layer and then the channel layer) can be explained in terms of the effect of these hydrophilic surfaces and the strong bonding scheme formed between the water molecules and the surface species. This stronger bonding scheme agrees very well with the same observation inferred from the structural properties of water molecules. As a result, water molecules in the channel layer have the slowest dynamics in the pore volume since they are confined from one side by surface species such as the Ca²⁺ ions and the silicate and hydroxyl groups on the surface. Additionally, water molecules dynamics in the interlayer space have the overall slowest water dynamics in the system because they are confined between two solid spaces in a very narrow volume.⁴⁵

Regardless of the examined water volume, we can notice that the diffusion coefficients of the water molecules (also the Na⁺ and Cl⁻ ions) in the 5% Na-doped tobermorite 14Å system are consistently slower than those calculated from the undoped tobermorite 14Å system. These calculations further confirm the same observations of slower dynamics deduced from the 1-D and 2-D density profiles. The explanation for these slow intrinsic dynamics of the 5% Na-doped systems will be discussed in a later subsection.

No studies were found in the literature examine the effect of doping molecular models that are representatives of cementitious materials on the dynamic properties of the interfacial water.

However, Duque-Redondo et al. studied water characteristics near the surface of defective tobermorite 14Å using computational methods.²⁶ They reported diffusion coefficients for water molecules deeply rooted in silicate cavities of 1.2×10^{-8} cm²/sec and at the middle of their 10Å pore of 3.6×10^{-6} cm²/sec. These values are similar to the ones reported for the undoped system in this work for the interlayer space (3.81×10^{-8} cm²/sec) and the bulk layer (6.05×10^{-6} cm²/sec), respectively. Higher values reported in this work can be attributed to the wider pore thickness studied (45Å).

Moreover, multiple computational studies also reported the same immobilization behavior of water and solvated ions near the interfaces of other tobermorite structures.^{21–23,25} This systematic decrease in water dynamics near these ultra-confined hydrophilic surfaces is explained in terms of the glassy nature of water molecules in these environments in a previously examined study.⁴⁵ It must be noted that while the overall trend of decreasing water dynamics near to the surface is consistent with the previously mentioned studies, the absolute value of the diffusion coefficient may vary by orders of magnitude because of multiple parameters such as the used water model and the potentials describing the interatomic interactions, or the number of sampled frames.

From experiments, the diffusion coefficient for water molecules in the C-S-H structure has been determined using Proton Field-Cycling Relaxometry (PFCR) and Quasielastic Neutron Scattering (QENS), which was found to be 2.6×10^{-7} cm²/sec¹¹⁴ and 10^{-6} cm²/sec^{62,115}, respectively. Again, these results agree very well with the computed diffusion coefficients of water located in the silicate channels (channel layer) (6.10×10^{-7} cm²/sec) and at the middle of the pore (6.05×10^{-6} cm²/sec) for the undoped system.

4.3.1.2. Diffusion Coefficient of Water Molecules in Bulk Systems

In addition to this, and to further quantitatively assess the surface effect on decreasing the diffusion coefficient of water molecules, we computed water diffusion coefficient in two additional systems: bulk liquid water without any solid interfaces or solvated salts and bulk liquid water without any solid interfaces but with the same concentration of Na^+ and Cl^- ions used in our interfacial systems (0.5 mol/L). In the former system, the diffusion coefficient for water molecules is calculated to be $2.21 \times 10^{-5} \text{ cm}^2/\text{sec}$ and is almost identical to the diffusion coefficient mentioned in the original paper for the water model ($2.32 \times 10^{-5} \text{ cm}^2/\text{sec}$) and experimentally at room temperature ($2.3 \times 10^{-5} \text{ cm}^2/\text{sec}$).^{72,116} For the latter system, the diffusion coefficient of water has slightly decreased to be $2.12 \times 10^{-5} \text{ cm}^2/\text{sec}$. This decrease in water diffusion coefficient upon adding Na^+ ions in the bulk liquid water is similar to the decrease noted earlier in water diffusion coefficients for the 5% Na-doped system than those in the undoped system.

These values for water diffusion coefficients in bulk liquid systems are almost one order of magnitude faster than the diffusion coefficient of water at the bulk layer of the undoped interfacial system ($6.05 \times 10^{-6} \text{ cm}^2/\text{sec}$). This decrease of water diffusion coefficients near solid interfaces compared to that in bulk liquid systems further confirms the confined nature of water molecules in these environments. On the other hand, we previously noticed from the convergence of the 1-D density profile of water molecules that the influence of the solid surfaces on the water density is diminished beyond the surface layer. However, we can still see that this influence on the dynamics of water molecules is maintained beyond the surface layer.

4.3.1.3. Diffusion Coefficient of Na^+ and Cl^- ions

We have also computed the diffusion coefficients for Na^+ and Cl^- ions on the surfaces of the undoped and the 5% Na-doped tobermorite 14\AA systems. For the Na^+ ions, the diffusion

coefficients are 2.20×10^{-6} cm²/sec and 3.20×10^{-7} cm²/sec for the undoped and the 5% Na-doped, respectively. It is important to note that in the 5% Na-doped system, we have two types of Na⁺ ions: surface Na⁺ ions and solvated Na⁺ ions. For this system, the diffusion coefficient for Na⁺ ions is computed from the positions of the solvated Na⁺ ions only to be consistent with the undoped system, where surface Na⁺ ions do not exist. For the Cl⁻ ions, the diffusion coefficients in the undoped and the 5% Na-doped systems are 3.24×10^{-6} cm²/sec and 4.12×10^{-7} cm²/sec, respectively. Moreover, and for reference, we computed the diffusion coefficients of Na⁺ and Cl⁻ ions in bulk water in separate simulations, which were found to be 0.9×10^{-5} cm²/sec and 1.41×10^{-5} cm²/sec, respectively. These results show the strong effect of the solid surfaces on the immobilization and decreasing the dynamics of the solvated salts, especially in the case of the 5% Na-doped system. Regardless of the examined systems: undoped or doped, we can always note that Na⁺ ions have a slower diffusion coefficient than Cl⁻ ions. This can be interpreted in terms of the overall negative surface of both tobermorite surfaces that prefers to adsorb and immobilize positive Na⁺ ions more than Cl⁻ ions.

Multiple researchers studied, using both computational and experimental methods, the dynamics of solvated Cl⁻ ions near the surface of cementitious materials and computed its diffusion coefficient. For the computational studies, the group of Hou et al. calculated the diffusion coefficient of solvated Cl⁻ ions near the surface of tobermorite 11Å to be 1.73×10^{-5} cm²/sec.²² In another study, They calculated Cl⁻ ions diffusion coefficient near the interface and at the middle of the pore of a defected tobermorite 11Å (varying the C/S ratio) to be 0.3×10^{-5} cm²/sec and 2.3×10^{-5} cm²/sec, respectively.²³ On the other hand, the group of Kalinichev et al. reported a diffusion coefficient for Cl⁻ ions near the surface of tobermorite 9Å to be 3.8×10^{-6} cm²/sec,²¹ which is almost

identical to the one computed in this work for Cl^- ions at the interface of the undoped system ($3.24 \times 10^{-6} \text{ cm}^2/\text{sec}$).

Moreover, using experimental techniques, Pivonka et al. studied Cl^- ions dynamic properties in cement pastes and compared them to those in bulk water.¹¹⁷ They concluded that the Cl^- ions diffusion coefficient in the cement pastes is equal to $1.7 \times 10^{-6} \text{ cm}^2/\text{sec}$ and is one order of magnitude smaller than their calculated Cl^- ions diffusion coefficient in a bulk salt solution system without any interfaces. They argued that this decrease in the dynamics of solvated Cl^- ions near solid interfaces of porous structures results from the stronger hydrogen bond network formed between the surrounding water molecules and the immobilization of water molecules in such ultra-confined environments. All these results agree very well with our findings regarding the slower dynamics of Cl^- ions near the solid interfaces of tobermorite 14\AA , either pristine or doped, compared to the bulk liquid salt solution.

4.1.3.4. The Effect of Doping Tobermorite 14\AA with 5% Na on the System Dynamics

For all examined species: Na^+ ions, Cl^- ions and, water molecules, we notice that the diffusion coefficients are always slower in the 5% Na-doped tobermorite 14\AA system than the undoped system tobermorite 14\AA . We previously noted indications for this from the 1-D density profiles and the 2-D contour plots, and now it has been calculated explicitly using the diffusion coefficients.

The intrinsic slower or faster diffusion coefficients of water molecules in liquid bulk systems containing solvated salts have been previously reported using experimental and computational methods.^{43,44} The two studies explain that some solvated salts are structure-making salts while others are structure-breaking ones.^{43,44} For the former type, the increase in the salt

concentration results in slower dynamics and slower diffusion coefficients for all species in the system. The opposite is true for the structure breaking salts; the system dynamics are faster because of increasing the salt concentration. For the NaCl salt, both experimental and computational studies agree that it is a structure-making salt that results in an overall slower dynamic.^{43,44}

Kim et al. explain that these changes in the dynamics of water molecules are because of two reasons: firstly, the existence of ions distorts the hydrogen bond network between water molecules, which results in faster dynamics, and secondly, the hydration of these ions and the bonds formed between them and water molecules slow down the system's dynamics.⁴⁴ The true diffusion coefficient of water molecules, and hence, the solvated ions, results from these competing and opposite forces. While the two examined systems in our study: the undoped and the 5% Na-doped have the same number (13) of solvated Na⁺ and Cl⁻ ions, the surfaces of the 5% Na-doped tobermorite contribute with additional six Na⁺ ions to the pore. Thus, we believe that the increase in the number of Na⁺ ions in the 5% Na-doped system is the reason for this system's intrinsic overall slower dynamics since its salt (NaCl) is a structure making salt.

It is also important to mention that CaCl₂ salt is also a structure making salt in another study.⁴³ However, while the Cl⁻ salts of both cations (Na⁺ and Ca²⁺) are structure making salts, we believe that substituting Ca²⁺ ions with Na⁺ ions to produce the 5% Na-doped system had a greater influence slowing down the overall dynamics of the system. This is because studies that examined the influence of NaCl and CaCl₂ salts were done using liquid bulk systems with no interfaces. However, in our study with the hydrophilic complex interfaces, Na⁺ ions are less tightly bonded to the surface than Ca⁺ atoms, which was noticed from 1-D density profiles for Na⁺ and Ca²⁺ ions in **Figure 11a and b**. Therefore, Na⁺ ions could coordinate with and decrease the diffusion coefficient of more water molecules than Ca²⁺ ions. This effect is the origin of the decrease in the

diffusion coefficients of water molecules, and hence, Na^+ and Cl^- ions in the 5% Na-doped tobermorite 14Å.

In a very recent interfacial study of cementitious materials, the group of Duque-Redondo et al. studied the effect of doping a defected tobermorite 14Å structure with Al^{3+} ions to produce a C-A-S-H structure on the adsorption characteristics of different solvated cations.¹¹⁸ In their study, and similar to the findings of this thesis, they report an overall decrease in the system dynamics and the introduction of new adsorption sites for the examined species. Moreover, in another study, they also noticed this decrease in the dynamics of the interfacial system above the surface of defected tobermorite 14Å with different C/S ratios.¹¹⁹ They explain these slow dynamics in terms of the increased hydrophilicity of the examined substrates because of the increase in hydrogen bond acceptors. A similar effect also exists in the structure adopted in this work because of the additional hydroxyl groups on the surface that originated from the charge balancing mechanism.

Preventing the ingress and the diffusion of any ions inside porous structures, such as the hydration products of alkali-activated cement, is twofold; first, it is essential to have stable and energetically favorable adsorption sites on the surface, and second, to have overall slower dynamics in the interfacial system. Moreover, it is crucial to have these slower dynamics effect in systems where stable adsorption sites are rare, which is the case for the surface of the tobermorite 14Å.

4.3.2. Vibrational Density of States of Water Molecules

Vibrational Density of States (VODS) of water molecules at different distances from the solid surface is calculated from the Fourier transform of the Velocity Auto Correlation function (VAF) for both the undoped and the 5% Na-doped tobermorite 14Å structures as described in

subsection 3.4.4. **Figure 15** show the VDOS of water molecules (a) in the interlayer region between the two solid surfaces, (b) deeply rooted in the channel layer, (c) in the surface layer, and (d) in the bulk water layer for both systems: 0% Na (solid red lines) % 5% Na (solid green lines). The VDOS of bulk water without any solid interfaces (dotted black line) and water confined in small channels in solid bulk pristine tobermorite (dashed black line) are also shown for reference in the four plots.

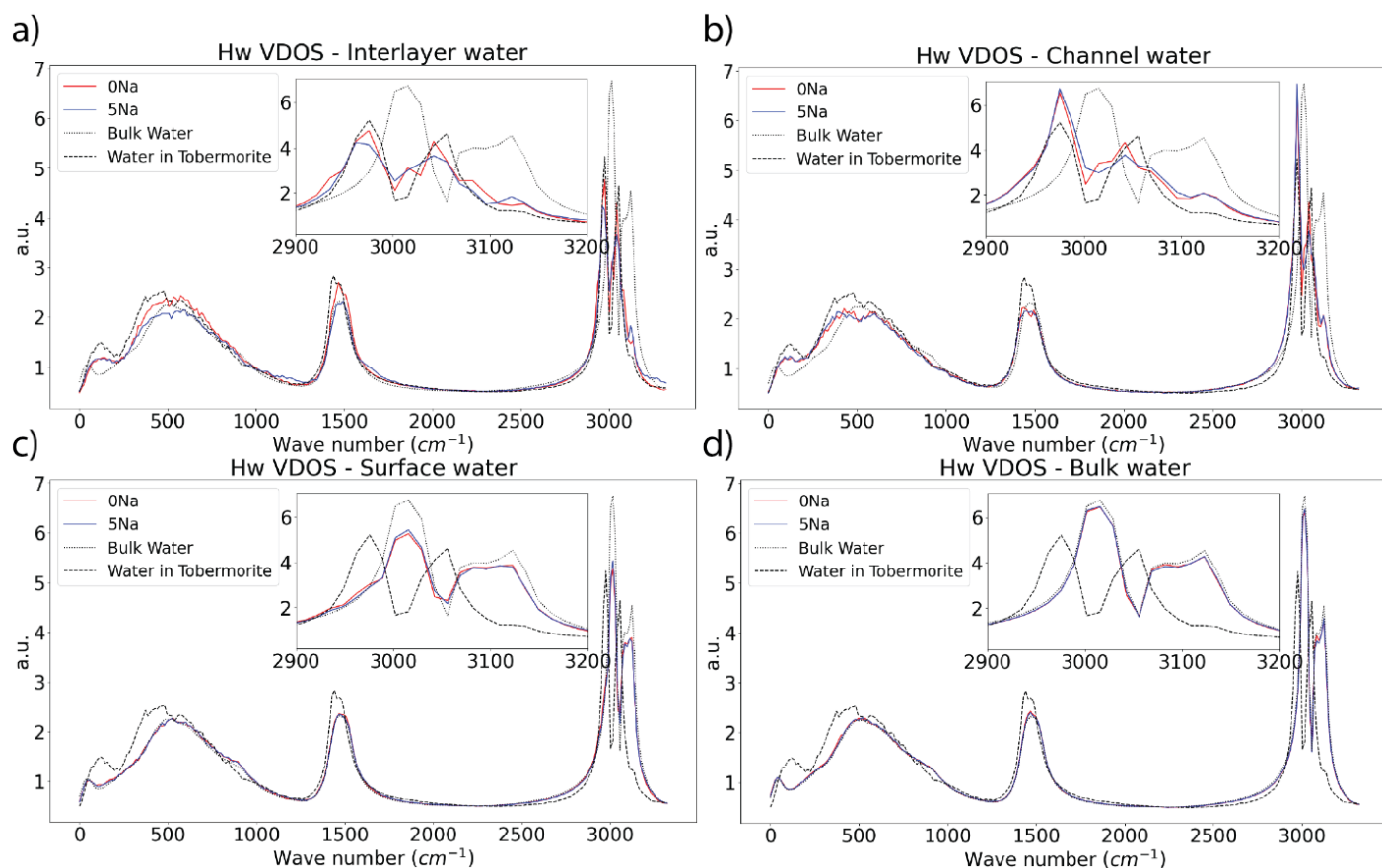


Figure 15. Vibrational Density of States (VDOS) of water molecules, calculated from the hydrogen atoms, at different distances from the surface: a) Interlayer water layer between two solid silicate layers, b) Channel water layer that is confined from one side by surface species, c) Surface water layer at a further distance from the surface, and d) Bulk water layer, which is midway between the two surfaces. VDOS of water in the undoped system (solid red lines) and 5% Na-doped system (solid green lines). For reference, it is also shown VDOS of water in bulk solid tobermorite without any artificial interfaces (dashed black line) and in bulk water without any solid (dotted black line).

VDOS plots of water can be categorized into three regions that correspond to the frequencies of different modes of vibration: the translational motion of water molecules (below 1000 cm^{-1}), the H-O-H angle bending (sharp peak at 1450 cm^{-1}), and the O-H stretching (two peaks around 3000 cm^{-1}).¹²⁰ The shift in the O-H stretching frequencies (intramolecular interactions) indicates the strength of the hydrogen bond network (intermolecular interactions).^{121,122} In other words, a red (blue) shift in the O-H stretching frequencies indicates a stronger (weaker) surrounding hydrogen bond network at the expense of weaker (stronger) intramolecular interactions. The inset plot in each of the four subplots in **Figure 15** represents the O-H stretching frequencies range using a magnified scale.

As shown in the four subplots of **Figure 15**, the dashed black line representing the O-H stretching frequencies for water molecules embedded between the solid layers of bulk solid tobermorite 14\AA shows a red shift compared to the same range of frequencies for bulk water (dotted black line). This shift indicates a stronger hydrogen bond network formed among water molecules and between water molecules and the solid species, which agrees very well with the previous results of slower diffusion coefficients of water molecules near the solid surfaces.

In **Figure 15**, we can also notice the gradual shift of the O-H frequencies of water molecules at different distances from both surfaces of the undoped (solid red lines) and the 5% Na-doped tobermorite 14\AA (solid blue lines) interfacial systems. In the interlayer space of both interfacial systems, **Figure 15a**, the O-H frequencies are almost identical to those for bulk solid tobermorite 14\AA . On the other hand, as shown in **Figure 15d**, the O-H frequencies in the bulk layer for both interfacial systems are almost identical to bulk liquid water with no interfaces. **Figure 15b and c** represent the O-H frequencies of water molecules in the channel and surface layers, respectively. In these layers, the range of O-H frequencies, and hence the strength of the

hydrogen bond network, is intermediate between those confined in the interlayer space and those far away from the surface at the bulk layer.

These results indicate that, for interfacial systems, the hydrogen bond network among water molecules is strongest when surrounded by two solid surfaces in the interlayer water space. This is followed by the hydrogen bond network formed in the channel layer, where water molecules are confined from one side only by the surface species. Then the strength of the hydrogen bond network is further reduced at the surface layer, where water molecules are separated from the surface species by the previously mentioned surface water layer. Finally, the hydrogen bond network is the weakest midway between the two solid surfaces at the bulk layer.

On the other hand, there is no prominent effect of adding Na^+ ions in bulk tobermorite 14\AA to produce the 5% Na-doped structure on the strength of the hydrogen bond network formed at the interface. This observation confirms that, as discussed in the previous section, the intrinsic slower dynamics of water near the 5% Na-doped system's surface results from the hydration of the extra Na^+ ions in this system and not from the hydrogen bond network.

4.3.3. Ions' residence time

In this section, we report the calculated residence time (**Equation 10**) from the time correlation function (TCF) (**Equation 9**) of water molecules in the entire volume of the channel and the surface water layers for both the undoped and the 5% Na-doped systems. For the undoped system, water molecules have a residence time of 70.5 ps (± 0.96). In comparison, for the 5% Na-doped system, water molecules' residence time equals 86.4 ps (± 12.39). These values are calculated separately for each simulation and averaged over the 12 ns and the 17 ns simulations done for the undoped and the 5% Na-doped systems. This increase in water molecules' residence time in the 5% Na-doped system agrees very well with the previous structural and dynamic results for water regarding the intrinsic slower dynamics of this system. In other words, water molecules spend, on average, more time near the surface of the 5% Na-doped system because of the structure-making effect resulting from the additional Na^+ ions.

On the other hand, we could not calculate the residence times of solvated Na^+ and Cl^- near the interfaces of the two systems for multiple reasons. Firstly, there are fewer Na^+ and Cl^- ions than water molecules in the system, making it statistically unreliable to report such values. In addition to the number of examined ions in the system, TCF (**Equation 9**) is also sensitive to the number of events where the examined criterion is satisfied and is failed to be satisfied. In other words, ions have to exit and re-enter the considered water volume multiple times to result in statistically reliable results. The second condition is specifically problematic for the 5% Na-doped system for two reasons. The first reason is that the intrinsically slow dynamics of this system are hindering the ions from exiting and re-entering the examined volume near the surface multiple times. Secondly, the stable CIP bonding for the Na^+ ions in the two systems and the Cl^- ions in the 5% Na-doped system further reduced the number of free ions to exit and re-enter the examined

water volume. This indicates that a careful analysis for different types of bonding is crucial when examining the residence time of ions at solid-liquid interfaces.

For these problems, a solution can be increasing the system size and the number of examined ions or running much longer simulations than those carried out in this thesis. Another solution will be examining the residence between ion-ion pairs and not for ions in a specific volume as done in previous studies,^{25,26} all of which are beyond the scope of this work and the available computational resources.

Chapter 5. Conclusions and Future Work

5.1. Conclusions

Alkali-activated cement (AAC) represents a less harmful to the environment substitute for the OPC used in construction projects. However, an assessment for the durability of the reaction products of AAC, known as the C-N-A-S-H structure, in environments where corrosive ions such as Cl^- ions exist in abundance is still missing. In this study, we built interfacial structures based on an undoped and a 5% Na-doped tobermorite 14\AA as molecular models for the reaction products of AAC, and specifically to enable isolation of the effects of sodium on the behavior of C-S-H-type gels. Moreover, we combined, adopted, and carefully examined a force field composed of a polarizable core-shell representation for the oxygen ions embedded in the solid structure and a flexible non-polarizable model representation for water molecules. Finally, and using molecular dynamics simulations, we examined the effect of doping the tobermorite 14\AA with 5% Na^+ ions on the structural, energetic, and dynamic properties of interfacial water molecules and adsorbed Na^+ and Cl^- ions. The main findings are summarized below.

5.1.1. Force field Benchmarking Studies

- i. For the undoped tobermorite 14\AA ($2 \times 1 \times 1$) supercell, and using structure optimization calculations at 0K, the adopted force field was able to reproduce experimental lattice parameters reported in the original experimental paper with very high accuracy.
- ii. For this system and with the same calculations, the force field was able to reproduce mechanical properties obtained from experimental work and ab initio calculations such as the young's modulus, the bulk modulus, the shear modulus, and basic trends of the elastic constant with a relatively good agreement.

- iii. For the undoped tobermorite 14\AA ($6 \times 4 \times 1$) supercell, and using molecular dynamics structure relaxation at 300K, our adopted force field predicted lattice parameters that are very similar to those predicted from the well-known ClayFF force field and those mentioned in the original experimental paper.
- iv. For the 5% Na-doped tobermorite 14\AA ($6 \times 4 \times 1$) supercell, and using molecular dynamics structure relaxation at 300K, again, our adopted force field predicted structure parameters similar to those calculated from ClayFF. Except for the beta angle (β), our adopted force field predicted the angles to have a similar value to the undoped structure, while ClayFF predicted it to increase by around 5%.

5.1.2. Characteristics of Interfacial Water Molecules

From the 1-D density profiles of water in both the undoped and the 5% Na-doped systems, we divided the interfacial water into three volumes: channel layer, surface layer, and bulk layer. In addition to those, the interlayer water region represents water molecules that are ultra-confined between the solid calcium-silicate layers in tobermorite 14\AA . The channel layer represents water molecules deeply rooted between the silicate chains with the highest structural order and direct contact with the surface species for both systems. The surface layer represents the intermediate transition between water molecules in the channel layer and in the bulk layer, wherein the bulk layer the water density is similar to liquid water. The main findings for water molecules at the surfaces of the undoped and the 5% Na-doped structures are summarized below.

- i. From the larger thickness of the surface layer and the larger number of Na^+ ions on the surface of the 5% Na-doped system, we concluded that this doped system influences the structural arrangement of water molecules further into the pore than the undoped system.

- ii. The diffusion coefficients of water molecules in both systems monotonically decreased as the distance from the surface decreased. Water molecules in the bulk layer had the largest diffusion coefficient, followed by the surface layers and then the channel layers. The slowest diffusion computed for water molecules was in the interlayer region, where water molecules are confined between two solid surfaces in a very narrow pore. This decrease in water dynamics is attributed to the influence of the surface and the strong hydrogen bond network formed between water molecules and the hydrophilic surfaces of tobermorite.
- iii. The largest value for water diffusion coefficient in the interfacial systems (in the bulk layer of the undoped system) is still less than the value calculated for bulk water without any solid interfaces, indicating an incomplete recovery from the influence of the solid surfaces in the interfacial system, even for such large pores (45Å).
- iv. For both systems, the influence of the solid surfaces on the strength of the hydrogen bond network formed at proximity from the surface was confirmed using the vibrational density of states (VDOS) calculations. This observation was concluded from the O-H stretching frequencies' systematic red shift for layers near the solid surfaces.
- v. For the 5% Na-doped tobermorite 14Å interfacial system, the introduction of Na⁺ ions as a dopant resulted in overall slower dynamics in the system compared to the undoped structure. These slower dynamics were firstly observed from the 1-D density profiles and the 2-D contours plots. However, the explicit diffusion coefficients calculations for different species of both systems confirmed these observations.
- vi. This intrinsic slower dynamic property of the 5% Na-doped systems is explained in terms of the excess number of Na⁺ ions in this system, which comes from the additional Na⁺ ions

doped in the solid structure, and that the NaCl salt is a structure-making salt that decreases the overall solvent-solute system dynamics as its concentration increases.

- vii. While no significant influence for doping the bulk solid structures on the VDOS of interfacial water molecules was noticed, doping the bulk structure with 5% Na had a prominent influence on the residence time of water molecules. Water molecules spent, on average, more time in the channel and surface layers of the 5% Na-doped system than the undoped system.

5.1.3. Characteristics of Adsorbed Na^+ and Cl^- Ions

- i. From the 1-D density profiles and the 2-D contour plots, more Na^+ ions are adsorbed than Cl^- ions on the surface of both undoped the 5% Na-doped tobermorite 14Å structures. This is because Cl^- ions are more repelled than Na^+ ions from the overall negative charge on both surfaces, originating from the dangling oxygen ions on the surface of tobermorite.
- ii. The adsorption mechanism of Na^+ ions on both surfaces is a mixture of the strong and stable contact ion pair (CIP), and the relatively weaker solvent separated ion pairs (SSIP) mechanisms.
- iii. For Cl^- ions on the surface of the undoped tobermorite, the adsorption mechanism is mainly SSIP, and ions are loosely attached to the surface.
- iv. Doping the tobermorite structure with Na^+ ions to produce the 5% Na-doped structure introduced two new rare but energetically stable CIP adsorption sites for Cl^- ions; one Cl^- ion is directly attached to one surface Si^{4+} ion, and the other Cl^- ion is attached to two H-OH ions. These new adsorption sites are resultant from the mechanism taking place to charge balance the structure after substituting Ca^{2+} ions with Na^+ ions.

- v. Adsorption free-energy profiles indicate that for the two systems: the undoped and the 5% Na-doped, it is more preferential to adsorb Na^+ ions than Cl^- ions. However, for the 5% Na-doped system, if Cl^- ions are adsorbed in one of the two CIP bonding schemes, it is more energetically difficult to desorb again into the pore.
- vi. Due to the surrounding solid surfaces and the strong hydrogen bond network formed among water molecules and between the water molecules and the solid surface, diffusion coefficients of Na^+ and Cl^- ions are much slower than those computed in bulk liquid water with no interfaces.
- vii. The diffusion coefficient of Na^+ ions is always slower than the diffusion coefficient of Cl^- ions. This is possible because a larger number of Na^+ ions are more strongly attached to the surfaces of both systems than Cl^- ions, excluding the two energetically stable adsorbed Cl^- ions.

These results conclude that doping the structure of the tobermorite 14\AA with 5% Na ions as a representative model for the C-N-S-H structure had a positive impact on the structural, energetic, and dynamic properties of the binding of interfacial Cl^- ions. This impact is described in the new energetically stable adsorption sites introduced from the charge balancing mechanism. Moreover, these new stable sites are enhanced by the overall slower dynamics from the excess concentration of the structure-making cations.

5.2. Recommendations and Future Work

- i. Studying the effect of other Na-doped molecular models, such 11\AA tobermorite, clinotobermorite, and jennite, on the adsorption characteristics of Na^+ and Cl^- ions.

- ii. Doping tobermorite 14\AA , and other molecular models, with aluminum ions (Al^{3+}) only and Al^{3+} ions combined with Na^+ ions or different monovalent alkaline ions such potassium (K^+).
- iii. The ionic bonding scheme found between the surface Si^{4+} and the solvated Cl^- ions needs further examination and validation using ab initio calculations to confirm the mechanism, the strength, and how frequent this type of bonding is likely to occur.
- iv. To test the hypothesis mentioned in the thesis and literature that increasing the Na^+ ions concentration requires causes more defected silicate chains. This analysis can be done by the random removal of bridging silicate groups only or the removal of pair silicate tetrahedra. This analysis will also test the effect of varying the C/S ratio on the adsorption characteristics of solvated ions.
- v. Instead of NaCl salt, other solvated anions such as sulfate (SO_4^{2-}) and carbonate (CO_3^{2-}) ions can have different adsorption characteristics because of the more complex structure and the increased number of species per ion. Moreover, they also exist in the same environments where Cl^- ions exist in abundance.
- vi. All these recommended studies can be done using similar molecular dynamics simulations or using more expensive DFT calculations. More recently developed machine learning algorithms can further enhance these calculations and enlarge the examined systems to a greater extent.
- vii. The relation between the pH of the alkali-activated slag and the volume of adsorbed Cl^- ions should also be further examined. This is because the charge balancing mechanism

used in this study and resulted from the substitution of Ca^{2+} ions with Na^+ ions is most likely to occur only when the AACs are synthesized at mild pH. However, alkali-activated slag has a higher pH (around 13), which will result in a fewer number of hydroxyl groups on the C-N-A-S-H surface.

- viii. Finally, experiments and atomistic simulations should confirm the local structure of the C-N-A-S-H structure predicted by the force field in this work by measuring quantities such as the radial distribution function ($g(r)$) for pairs such as Ca-O and Si-O for the 5% Na-doped tobermorite.

References

1. van Ruijven BJ, van Vuuren DP, Boskaljon W, Neelis ML, Saygin D, Patel MK. Long-term model-based projections of energy use and CO₂ emissions from the global steel and cement industries. *Resour Conserv Recycl.* 2016 Sep;112:15–36.
2. Scrivener KL, Kirkpatrick RJ. Innovation in use and research on cementitious material. *Cem Concr Res.* 2008 Feb 1;38(2):128–36.
3. Griffin PW, Hammond GP, Norman JB. Industrial energy use and carbon emissions reduction: a UK perspective. *WIREs Energy Environ.* 2016;5(6):684–714.
4. Pacheco-Torgal F, Castro-Gomes J, Jalali S. Alkali-activated binders: A review: Part 1. Historical background, terminology, reaction mechanisms and hydration products. *Constr Build Mater.* 2008 Jul 1;22(7):1305–14.
5. Pacheco-Torgal F, Castro-Gomes J, Jalali S. Alkali-activated binders: A review. Part 2. About materials and binders manufacture. *Constr Build Mater.* 2008 Jul 1;22(7):1315–22.
6. Yang K-H, Song J-K, Song K-I. Assessment of CO₂ reduction of alkali-activated concrete. *J Clean Prod.* 2013 Jan 1;39:265–72.
7. Duxson P, Provis JL, Lukey GC, van Deventer JSJ. The role of inorganic polymer technology in the development of ‘green concrete.’ *Cem Concr Res.* 2007 Dec 1;37(12):1590–7.
8. Allen AJ, Thomas JJ, Jennings HM. Composition and density of nanoscale calcium-silicate-hydrate in cement. *Nat Mater.* 2007 Apr;6(4):311–6.
9. Abdolhosseini Qomi MJ, Krakowiak KJ, Bauchy M, Stewart KL, Shahsavari R, Jagannathan D, et al. Combinatorial molecular optimization of cement hydrates. *Nat Commun.* 2014 Sep 24;5:4960.
10. Richardson IG. The nature of C-S-H in hardened cements. *Cem Concr Res.* 1999 Aug 1;29(8):1131–47.
11. Özçelik VO, White CE. Nanoscale Charge-Balancing Mechanism in Alkali-Substituted Calcium–Silicate–Hydrate Gels. *J Phys Chem Lett.* 2016 Dec 15;7(24):5266–72.

12. Özçelik VO, Garg N, White CE. Symmetry-Induced Stability in Alkali-Doped Calcium Silicate Hydrate. *J Phys Chem C*. 2019 Jun 6;123(22):14081–8.
13. Yaphary YL, Lau D, Sanchez F, Poon CS. Effects of sodium/calcium cation exchange on the mechanical properties of calcium silicate hydrate (C-S-H). *Constr Build Mater*. 2020 May 20;243:118283.
14. Le Losq C, Neuville DR, Chen W, Florian P, Massiot D, Zhou Z, et al. Percolation channels: a universal idea to describe the atomic structure and dynamics of glasses and melts. *Sci Rep*. 2017 Nov 28;7(1):16490.
15. P. Kumar Mehta PD, Paulo J. M. Monteiro PD. *Concrete: Microstructure, Properties, and Materials, Fourth Edition*. McGraw-Hill Education; 2014
16. Kumar A, Walder BJ, Kunhi Mohamed A, Hofstetter A, Srinivasan B, Rossini AJ, et al. The Atomic-Level Structure of Cementitious Calcium Silicate Hydrate. *J Phys Chem C*. 2017 Aug 17;121(32):17188–96.
17. Garg N, Özçelik VO, Skibsted J, White CE. Nanoscale Ordering and Depolymerization of Calcium Silicate Hydrates in the Presence of Alkalis. *J Phys Chem C*. 2019 Oct 10;123(40):24873–83.
18. Soyer-Uzun S, Chae SR, Benmore CJ, Wenk H-R, Monteiro PJM. Compositional Evolution of Calcium Silicate Hydrate (C–S–H) Structures by Total X-Ray Scattering. *J Am Ceram Soc*. 2012;95(2):793–8.
19. Kovačević G, Persson B, Nicoleau L, Nonat A, Veryazov V. Atomistic modeling of crystal structure of $\text{Ca}_{1.67}\text{SiH}_x$. *Cem Concr Res*. 2015 Jan 1;67:197–203.
20. Kalinichev AG, Kirkpatrick RJ. Molecular Dynamics Modeling of Chloride Binding to the Surfaces of Calcium Hydroxide, Hydrated Calcium Aluminate, and Calcium Silicate Phases. *Chem Mater*. 2002 Aug 1;14(8):3539–49.
21. Kalinichev AG, Wang J, Kirkpatrick RJ. Molecular dynamics modeling of the structure, dynamics and energetics of mineral–water interfaces: Application to cement materials. *Cem Concr Res*. 2007 Mar 1;37(3):337–47.

22. Hou D, Li Z. Molecular dynamics study of water and ions transport in nano-pore of layered structure: A case study of tobermorite. *Microporous Mesoporous Mater.* 2014 Sep 1;195:9–20.
23. Zhou Y, Hou D, Jiang J, Liu L, She W, Yu J. Experimental and molecular dynamics studies on the transport and adsorption of chloride ions in the nano-pores of calcium silicate phase: The influence of calcium to silicate ratios. *Microporous Mesoporous Mater.* 2018 Jan 1;255:23–35.
24. Zhou Y, Hou D, Jiang J, She W, Li J. Molecular dynamics study of solvated aniline and ethylene glycol monomers confined in calcium silicate nanochannels: a case study of tobermorite. *Phys Chem Chem Phys.* 2017;19(23):15145–59.
25. Jiang J, Wang P, Hou D. The mechanism of cesium ions immobilization in the nanometer channel of calcium silicate hydrate: a molecular dynamics study. *Phys Chem Chem Phys.* 2017 Oct 25;19(41):27974–86.
26. Duque-Redondo E, Kazuo Y, López-Arbeloa I, Manzano H. Cs-137 immobilization in C-S-H gel nanopores. *Phys Chem Chem Phys.* 2018 Apr 4;20(14):9289–97.
27. Pan T, Xia K, Wang L. Chloride binding to calcium silicate hydrates (C-S-H) in cement paste: a molecular dynamics analysis. *Int J Pavement Eng.* 2010 Oct 1;11(5):367–79.
28. Bu J, Gonzalez Teresa R, Brown KG, Sanchez F. Adsorption mechanisms of cesium at calcium-silicate-hydrate surfaces using molecular dynamics simulations. *J Nucl Mater.* 2019 Mar 1;515:35–51.
29. Liu Z, Xu D, Gao S, Zhang Y, Jiang J. Assessing the Adsorption and Diffusion Behavior of Multicomponent Ions in Saturated Calcium Silicate Hydrate Gel Pores Using Molecular Dynamics. *ACS Sustain Chem Eng.* 2020 Mar 9;8(9):3718–27.
30. Hajilar S, Shafei B. Structure, orientation, and dynamics of water-soluble ions adsorbed to basal surfaces of calcium monosulfoaluminate hydrates. *Phys Chem Chem Phys.* 2018 Oct 3;20(38):24681–94.
31. Hou D, Li T, Han Q, Zhang J. Insight on the sodium and chloride ions adsorption mechanism on the ettringite crystal: Structure, dynamics and interfacial interaction. *Comput Mater Sci.* 2018 Oct 1;153:479–92.

32. Wang P, Jia Y, Li T, Hou D, Zheng Q. Molecular dynamics study on ions and water confined in the nanometer channel of Friedel's salt: structure, dynamics and interfacial interaction. *Phys Chem Chem Phys*. 2018;20(42):27049–58.
33. Wang L, Hou D, Shang H, Zhao T. Molecular dynamics study on the Tri-calcium silicate hydration in sodium sulfate solution: Interface structure, dynamics and dissolution mechanism. *Constr Build Mater*. 2018 May 10;170:402–17.
34. Merlino S, Bonaccorsi E, Armbruster T. The real structures of clinotobermorite and tobermorite 9 Å: OD character, polytypes, and structural relationships. *Eur J Mineral*. 2000 Mar 29;411–29.
35. Hamid SA. The crystal structure of the 11 Å natural tobermorite $\text{Ca}_{2.25}[\text{Si}_3\text{O}_7.5(\text{OH})_{1.5}] \cdot 1\text{H}_2\text{O}$. *Z Für Krist - Cryst Mater*. 2015;154(1–4):189–98.
36. Merlino S, Bonaccorsi E, Armbruster T. The real structure of tobermorite 11 Å normal and anomalous forms, OD character and polytypic modifications. *Eur J Mineral*. 2001 May 1;13(3):577–90.
37. Bonaccorsi E, Merlino S, Kampf AR. The Crystal Structure of Tobermorite 14 Å (Plombierite), a C–S–H Phase. *J Am Ceram Soc*. 2005 Mar 1;88(3):505–12.
38. Hoffmann C, Armbruster T. Clinotobermorite, $\text{Ca}_5[\text{Si}_3\text{O}_8(\text{OH})_2] \cdot 4\text{H}_2\text{O}$ - $\text{Ca}_5[\text{Si}_6\text{O}_{17}] \cdot 5\text{H}_2\text{O}$, a natural C-S-H(I) type cement mineral: determination of the substructure. *Z Für Krist - Cryst Mater*. 2010;212(12):864–73.
39. Bonaccorsi E, Merlino S, Taylor HFW. The crystal structure of jennite, $\text{Ca}_9\text{Si}_6\text{O}_{18}(\text{OH})_6 \cdot 8\text{H}_2\text{O}$. *Cem Concr Res*. 2004 Sep 1;34(9):1481–8.
40. Wang S-D, Scrivener KL. Hydration products of alkali activated slag cement. *Cem Concr Res*. 1995 Apr 1;25(3):561–71.
41. Escalante-García JI, Fuentes AF, Gorokhovskiy A, Fraire-Luna PE, Mendoza-Suarez G. Hydration Products and Reactivity of Blast-Furnace Slag Activated by Various Alkalis. *J Am Ceram Soc*. 2003 Dec 1;86(12):2148–53.

42. Ben Haha M, Le Saout G, Winnefeld F, Lothenbach B. Influence of activator type on hydration kinetics, hydrate assemblage and microstructural development of alkali activated blast-furnace slags. *Cem Concr Res.* 2011 Mar 1;41(3):301–10.
43. Müller KJ, Hertz HG. A Parameter as an Indicator for Water–Water Association in Solutions of Strong Electrolytes. *J Phys Chem.* 1996 Jan 1;100(4):1256–65.
44. Kim JS, Wu Z, Morrow AR, Yethiraj A, Yethiraj A. Self-Diffusion and Viscosity in Electrolyte Solutions. *J Phys Chem B.* 2012 Oct 4;116(39):12007–13.
45. Youssef M, Pellenq RJ-M, Yildiz B. Glassy Nature of Water in an Ultraconfining Disordered Material: The Case of Calcium–Silicate–Hydrate. *J Am Chem Soc.* 2011 Mar 2;133(8):2499–510.
46. Mindess S, Young JF. *Concrete.* Englewood Cliffs, NJ: Prentice-Hall; 1981.
47. Bullard JW, Jennings HM, Livingston RA, Nonat A, Scherer GW, Schweitzer JS, et al. Mechanisms of cement hydration. *Cem Concr Res.* 2011 Dec 1;41(12):1208–23.
48. ²⁹Si MAS NMR study of the structure of calcium silicate hydrate. *Adv Cem Based Mater.* 1996 Apr 1;3(3–4):144–56.
49. Kunhi Mohamed A, Parker SC, Bowen P, Galmarini S. An atomistic building block description of C-S-H - Towards a realistic C-S-H model. *Cem Concr Res.* 2018 May 1;107:221–35.
50. Thomas JJ, Chen JJ, Jennings HM, Neumann DA. Ca-OH bonding in the C-S-H gel phase of tricalcium silicate and white portland cement pastes measured by inelastic neutron scattering. *Chem Mater.* 2003;15(20):3813–7.
51. Yu P, Kirkpatrick RJ, Poe B, McMillan PF, Cong X. Structure of Calcium Silicate Hydrate (C-S-H): Near-, Mid-, and Far-Infrared Spectroscopy. *J Am Ceram Soc.* 1999;82(3):742–8.
52. Kirkpatrick RJ, Yarger JL, McMillan PF, Ping Y, Cong X. Raman spectroscopy of C-S-H, tobermorite, and jennite. *Adv Cem Based Mater.* 1997;5(3):93–9.
53. Nonat A. The structure and stoichiometry of C-S-H. *Cem Concr Res.* 2004 Sep 1;34(9):1521–8.

54. Pellenq RJ-M, Kushima A, Shahsavari R, Vliet KJV, Buehler MJ, Yip S, et al. A realistic molecular model of cement hydrates. *Proc Natl Acad Sci*. 2009 Sep 22;106(38):16102–7.
55. van Duin ACT, Dasgupta S, Lorant F, Goddard WA. ReaxFF: A Reactive Force Field for Hydrocarbons. *J Phys Chem A*. 2001 Oct 1;105(41):9396–409.
56. Licht S, Wu H, Hettige C, Wang B, Asercion J, Lau J, et al. STEP cement: Solar Thermal Electrochemical Production of CaO without CO₂ emission. *Chem Commun*. 2012 May 21;48(48):6019–21.
57. Shi C, Wu X, Tang M. Hydration of alkali-slag cements at 150°C. *Cem Concr Res*. 1991 Jan 1;21(1):91–100.
58. Wang J, Kalinichev AG, Kirkpatrick RJ. Effects of substrate structure and composition on the structure, dynamics, and energetics of water at mineral surfaces: A molecular dynamics modeling study. *Geochim Cosmochim Acta*. 2006 Feb 1;70(3):562–82.
59. Schlaich A, Knapp EW, Netz RR. Water Dielectric Effects in Planar Confinement. *Phys Rev Lett*. 2016 Jul 19;117(4):048001.
60. Sato T, Sasaki T, Ohnuki J, Umezawa K, Takano M. Hydrophobic Surface Enhances Electrostatic Interaction in Water. *Phys Rev Lett*. 2018 Nov 15;121(20):206002.
61. Varghese S, Kannam SK, Hansen JS, Sathian SP. Effect of Hydrogen Bonds on the Dielectric Properties of Interfacial Water. *Langmuir*. 2019 Jun 18;35(24):8159–66.
62. Bordallo HN, Aldridge LP, Desmedt A. Water Dynamics in Hardened Ordinary Portland Cement Paste or Concrete: From Quasielastic Neutron Scattering. *J Phys Chem B*. 2006 Sep 1;110(36):17966–76.
63. Romero-Vargas Castrillón S, Giovambattista N, Aksay IA, Debenedetti PG. Effect of Surface Polarity on the Structure and Dynamics of Water in Nanoscale Confinement. *J Phys Chem B*. 2009 Feb 5;113(5):1438–46.
64. Lombardo TG, Giovambattista N, Debenedetti PG. Structural and mechanical properties of glassy water in nanoscale confinement. *Faraday Discuss*. 2008 Nov 25;141(0):359–76.

65. Yoon S, Ha J, Chae SR, Kilcoyne DA, Monteiro PJM. X-ray spectromicroscopic study of interactions between NaCl and calcium silicate hydrates. *Mag Concr Res.* 2014 Feb 1;66(3):141–9.
66. Cygan RT, Liang J-J, Kalinichev AG. Molecular Models of Hydroxide, Oxyhydroxide, and Clay Phases and the Development of a General Force Field. *J Phys Chem B.* 2004 Jan 1;108(4):1255–66.
67. Shahsavari R, Pellenq RJ-M, Ulm F-J. Empirical force fields for complex hydrated calcio-silicate layered materials. *Phys Chem Chem Phys.* 2010 Dec 22;13(3):1002–11.
68. Galmarini SC. Atomistic Simulation of Cementitious Systems. 2013 [cited 2018 Sep 22]; Available from: <https://infoscience.epfl.ch/record/186587/usage>
69. Lewis GV, Catlow CRA. Potential models for ionic oxides. *J Phys C Solid State Phys.* 1985 Feb 1;18:1149–61.
70. Abascal JLF, Vega C. A general purpose model for the condensed phases of water: TIP4P/2005. *J Chem Phys.* 2005 Dec 15;123(23):234505.
71. Dick BG, Overhauser AW. Theory of the Dielectric Constants of Alkali Halide Crystals. *Phys Rev.* 1958 Oct 1;112(1):90–103.
72. Wu Y, Tepper HL, Voth GA. Flexible simple point-charge water model with improved liquid-state properties. *J Chem Phys.* 2006 Jan 10;124(2):024503.
73. Kobayashi K, Nakamura H, Yamaguchi A, Itakura M, Machida M, Okumura M. Machine learning potentials for tobermorite minerals. *Comput Mater Sci.* 2021 Feb 15;188:110173.
74. Soyer-Uzun S, Chae SR, Benmore CJ, Wenk H-R, Monteiro PJM. Compositional Evolution of Calcium Silicate Hydrate (C–S–H) Structures by Total X-Ray Scattering. *J Am Ceram Soc.* 2012;95(2):793–8.
75. Skinner LB, Chae SR, Benmore CJ, Wenk HR, Monteiro PJM. Nanostructure of Calcium Silicate Hydrates in Cements. *Phys Rev Lett.* 2010 May 11;104(19):195502.
76. Gallucci E, Zhang X, Scrivener KL. Effect of temperature on the microstructure of calcium silicate hydrate (C-S-H). *Cem Concr Res.* 2013 Nov 1;53:185–95.

77. Cong X, Kirkpatrick R. Effects of the temperature and relative humidity on the structure of CSH gel. 1995;
78. Crystallography Open Database [Internet]. [cited 2021 Jun 21]. Available from: <http://www.crystallography.net/cod/index.php>
79. Momma K, Izumi F. VESTA 3 for three-dimensional visualization of crystal, volumetric and morphology data. *J Appl Crystallogr*. 2011 Dec 1;44(6):1272–6.
80. Sidney Mindess JFY and David Darwin. Concrete 2nd Edition. Tech Doc. 2003 Jan 1;
81. Taylor H f. w. Cement chemistry [Internet]. Thomas Telford Publishing; 1997 [cited 2021 Apr 16]. 1. Available from: <https://www.icevirtuallibrary.com/doi/book/10.1680/cc.25929>
82. Lin F-Y, MacKerell AD. Force fields for small molecules. *Methods Mol Biol Clifton NJ*. 2019;2022:21–54.
83. Joung IS, Cheatham TE. Determination of alkali and halide monovalent ion parameters for use in explicitly solvated biomolecular simulations. *J Phys Chem B*. 2008 Jul 31;112(30):9020–41.
84. Kerisit S, Parker SC, Harding JH. Atomistic Simulation of the Dissociative Adsorption of Water on Calcite Surfaces. *J Phys Chem B*. 2003 Aug 1;107(31):7676–82.
85. Allen JP, Parker SC, Price DW. Atomistic Simulation of the Surface Carbonation of Calcium and Magnesium Oxide Surfaces. *J Phys Chem C*. 2009 May 14;113(19):8320–8.
86. Baram PS, Parker SC. Atomistic simulation of hydroxide ions in inorganic solids. *Philos Mag B*. 1996 Jan 1;73(1):49–58.
87. Kerisit S, Ilton ES, Parker SC. Molecular Dynamics Simulations of Electrolyte Solutions at the (100) Goethite Surface. *J Phys Chem B*. 2006 Oct 1;110(41):20491–501.
88. Kundu TK, Rao KH, Parker SC. Competitive Adsorption on Wollastonite: An Atomistic Simulation Approach. *J Phys Chem B*. 2005 Jun 1;109(22):11286–95.
89. Raiteri P, Gale JD. Water Is the Key to Nonclassical Nucleation of Amorphous Calcium Carbonate. *J Am Chem Soc*. 2010 Dec 15;132(49):17623–34.

90. Lorentz HA. Ueber die Anwendung des Satzes vom Virial in der kinetischen Theorie der Gase. *Ann Phys.* 1881;248(1):127–36.
91. Allen JP, Parker SC, Price DW. Atomistic Simulation of the Surface Carbonation of Calcium and Magnesium Oxide Surfaces. *J Phys Chem C.* 2009 May 14;113(19):8320–8.
92. Joung IS, Cheatham TE. Determination of Alkali and Halide Monovalent Ion Parameters for Use in Explicitly Solvated Biomolecular Simulations. *J Phys Chem B.* 2008 Jul 1;112(30):9020–41.
93. Wu Y, Tepper HL, Voth GA. Flexible simple point-charge water model with improved liquid-state properties. *J Chem Phys.* 2006 Jan 10;124(2):024503.
94. Greathouse JA, Durkin JS, Larentzos JP, Cygan RT. Implementation of a Morse potential to model hydroxyl behavior in phyllosilicates. *J Chem Phys.* 2009 Apr 7;130(13):134713.
95. Pouvreau M, Greathouse JA, Cygan RT, Kalinichev AG. Structure of Hydrated Kaolinite Edge Surfaces: DFT Results and Further Development of the ClayFF Classical Force Field with Metal–O–H Angle Bending Terms. *J Phys Chem C.* 2019 May 9;123(18):11628–38.
96. Gale JD, Rohl AL. The General Utility Lattice Program (GULP). *Mol Simul.* 2003 May 1;29(5):291–341.
97. Shahsavari R, Buehler MJ, Pellenq RJ-M, Ulm F-J. First-Principles Study of Elastic Constants and Interlayer Interactions of Complex Hydrated Oxides: Case Study of Tobermorite and Jennite. *J Am Ceram Soc.* 2009 Oct 1;92(10):2323–30.
98. Oh JE, Clark SM, Wenk H-R, Monteiro PJM. Experimental determination of bulk modulus of 14Å tobermorite using high pressure synchrotron X-ray diffraction. *Cem Concr Res.* 2012 Feb 1;42(2):397–403.
99. Manzano H, Masoero E, Lopez-Arbeloa I, Jennings HM. Shear deformations in calcium silicate hydrates. *Soft Matter.* 2013 Jul 11;9(30):7333–41.
100. Shahsavari R, Buehler MJ, Pellenq RJ-M, Ulm F-J. First-Principles Study of Elastic Constants and Interlayer Interactions of Complex Hydrated Oxides: Case Study of Tobermorite and Jennite. *J Am Ceram Soc.* 2009;92(10):2323–30.

101. T. Todorov I, Smith W, Trachenko K, T. Dove M. DL_POLY_3: new dimensions in molecular dynamics simulations via massive parallelism. *J Mater Chem*. 2006;16(20):1911–8.
102. Smith W. The DL-POLY Classic User Manual. :305.
103. Frenkel D, Smit B. *Understanding Molecular Simulation: From Algorithms to Applications*. Academic Press; 1996. 443 p.
104. Sahoo SK, Nair NN. Interfacing the Core-Shell or the Drude Polarizable Force Field With Car–Parrinello Molecular Dynamics for QM/MM Simulations. *Front Chem* [Internet]. 2018 [cited 2020 Sep 9];6. Available from: <https://www.frontiersin.org/articles/10.3389/fchem.2018.00275/full>
105. VandeVondele J, Mohamed F, Krack M, Hutter J, Sprik M, Parrinello M. The influence of temperature and density functional models in ab initio molecular dynamics simulation of liquid water. *J Chem Phys*. 2004 Dec 15;122(1):014515.
106. Steneteg P, Abrikosov IA, Weber V, Niklasson AMN. Wave function extended Lagrangian Born-Oppenheimer molecular dynamics. *Phys Rev B*. 2010 Aug 9;82(7):075110.
107. Kerisit S, Parker SC. Free Energy of Adsorption of Water and Metal Ions on the {1014} Calcite Surface. *J Am Chem Soc*. 2004 Aug 1;126(32):10152–61.
108. Hill TL. *Statistical Mechanics: Principles and Selected Applications*. Courier Corporation; 1956. 466 p.
109. Allen MP, Tildesley DJ, Banavar JR. Computer Simulation of Liquids. *Phys Today*. 1989 Mar 1;42(3):105–6.
110. Impey RW, Madden PA, McDonald IR. Hydration and mobility of ions in solution. *J Phys Chem*. 1983 Dec 1;87(25):5071–83.
111. Yu P, Kirkpatrick RJ. ³⁵Cl NMR relaxation study of cement hydrate suspensions. *Cem Concr Res*. 2001 Oct 1;31(10):1479–85.
112. Ye H, Huang L, Chen Z. Influence of activator composition on the chloride binding capacity of alkali-activated slag. *Cem Concr Compos*. 2019 Nov 1;104:103368.

113. Jun Y, Yoon S, Oh JE. A Comparison Study for Chloride-Binding Capacity between Alkali-Activated Fly Ash and Slag in the Use of Seawater. *Appl Sci*. 2017 Oct;7(10):971.
114. Korb J-P, McDonald PJ, Monteilhet L, Kalinichev AG, Kirkpatrick RJ. Comparison of proton field-cycling relaxometry and molecular dynamics simulations for proton–water surface dynamics in cement-based materials. *Cem Concr Res*. 2007 Mar;37(3):348–50.
115. Fratini E, Faraone A, Ridi F, Chen S-H, Baglioni P. Hydration Water Dynamics in Tricalcium Silicate Pastes by Time-Resolved Incoherent Elastic Neutron Scattering. *J Phys Chem C*. 2013 Apr 11;117(14):7358–64.
116. Krynicky K, Green CD, Sawyer DW. Pressure and temperature dependence of self-diffusion in water. *Faraday Discuss Chem Soc*. 1978 Jan 1;66(0):199–208.
117. Pivonka P, Hellmich C, Smith D. Microscopic effects on chloride diffusivity of cement pastes—a scale-transition analysis. *Cem Concr Res*. 2004 Dec 1;34(12):2251–60.
118. Duque-Redondo E, Yamada K, Dolado JS, Manzano H. Microscopic mechanism of radionuclide Cs retention in Al containing C-S-H nanopores. *Comput Mater Sci*. 2021 Apr 1;190:110312.
119. Duque-Redondo E, Yamada K, Manzano H. Cs retention and diffusion in C-S-H at different Ca/Si ratio. *Cem Concr Res*. 2021 Feb 1;140:106294.
120. Martinez-Gonzalez JA, English NJ, Gowen AA. Understanding the interface between silicon-based materials and water: Molecular-dynamics exploration of infrared spectra. *AIP Adv*. 2017 Nov 1;7(11):115105.
121. Seki T, Chiang K-Y, Yu C-C, Yu X, Okuno M, Hunger J, et al. The Bending Mode of Water: A Powerful Probe for Hydrogen Bond Structure of Aqueous Systems. *J Phys Chem Lett*. 2020 Oct 1;11(19):8459–69.
122. Ojha D, Karhan K, Kühne TD. On the Hydrogen Bond Strength and Vibrational Spectroscopy of Liquid Water. *Sci Rep*. 2018 Nov 15;8(1):16888.

Appendix A: GULP Input File

This section presents a sample input file for the GULP⁹⁶ code used in the structure optimization calculations. This was done only to the (2 x 1 x 1) supercell for the undoped solid bulk tobermorite 14Å. Atoms' coordinates are also included.

GULP INPUT FILE

```
opti conp molecule nosym prop
name Tobermorite14A
element
symbol 69 Ow
mass Ow 15.996
covalent Ow 0.73
vdw Ow 1.36
ionic Ow 1.26
symbol 74 Hw
mass Hw 1.008
covalent Hw 0.37
vdw Hw 1.17
ionic Hw -0.24
symbol 71 Oh
mass Oh 16.00
covalent Oh 0.73
vdw Oh 1.36
ionic Oh 1.26
symbol 72 Hh
mass Hh 1.008
covalent Hh 0.37
vdw Hh 1.17
ionic Hh -0.24
symbol 20 Ca
covalent Ca 0.00
symbol 14 Si
covalent Si 0.0
covalent O 0.0
vdw O 1.36
ionic O 1.26
end
cell
  13.366183 7.386403 28.624956 89.992406 90.002836 123.515144
fractional
Ca core 0.3684999 0.4250000 0.2851999 2.00000000 1.00000 1.00000
Ca core 0.3711705 0.9202840 0.7110651 2.00000000 1.00000 1.00000
```

Ca core 0.6228256 0.4222712 0.7882039 2.0000000 1.00000 1.00000
Ca core 0.6203462 0.9209455 0.2154172 2.0000000 1.00000 1.00000
Ca core 0.8697163 0.4211637 0.2901438 2.0000000 1.00000 1.00000
Ca core 0.8719090 0.9214200 0.7171937 2.0000000 1.00000 1.00000
Ca core 0.1212571 0.4202578 0.7860003 2.0000000 1.00000 1.00000
Ca core 0.1220192 0.9232746 0.2131260 2.0000000 1.00000 1.00000
Ca core 0.1408119 0.4423057 0.2080421 2.0000000 1.00000 1.00000
Ca core 0.1385467 0.9393563 0.7875574 2.0000000 1.00000 1.00000
Ca core 0.3913310 0.4403929 0.7084688 2.0000000 1.00000 1.00000
Ca core 0.3874424 0.9433705 0.2884642 2.0000000 1.00000 1.00000
Ca core 0.6373937 0.4402577 0.2138064 2.0000000 1.00000 1.00000
Ca core 0.6417583 0.9411714 0.7931196 2.0000000 1.00000 1.00000
Ca core 0.8883976 0.4398712 0.7129295 2.0000000 1.00000 1.00000
Ca core 0.8900149 0.9412518 0.2927118 2.0000000 1.00000 1.00000
Ca core 0.4375539 0.0004246 0.0042245 2.0000000 1.00000 1.00000
Ca core 0.6876714 0.9999804 0.5060797 2.0000000 1.00000 1.00000
Ca core 0.9375218 0.5004563 0.9971399 2.0000000 1.00000 1.00000
Ca core 0.1872906 0.5000082 0.4953180 2.0000000 1.00000 1.00000
Si core 0.3831025 0.3914896 0.1718035 4.0000000 1.00000 1.00000
Si core 0.3802353 0.8916741 0.8240737 4.0000000 1.00000 1.00000
Si core 0.6349200 0.3926356 0.6738334 4.0000000 1.00000 1.00000
Si core 0.6274055 0.8899836 0.3270569 4.0000000 1.00000 1.00000
Si core 0.8794108 0.3921975 0.1771889 4.0000000 1.00000 1.00000
Si core 0.8839280 0.8903236 0.8299515 4.0000000 1.00000 1.00000
Si core 0.1284015 0.3887575 0.6743705 4.0000000 1.00000 1.00000
Si core 0.1333508 0.8937769 0.3275458 4.0000000 1.00000 1.00000
Si core 0.4636368 0.7614851 0.1019979 4.0000000 1.00000 1.00000
Si core 0.4433105 0.2415416 0.8997606 4.0000000 1.00000 1.00000
Si core 0.7159790 0.7621063 0.6037393 4.0000000 1.00000 1.00000
Si core 0.6907898 0.2421816 0.4020330 4.0000000 1.00000 1.00000
Si core 0.9428167 0.7420823 0.1014735 4.0000000 1.00000 1.00000
Si core 0.9643267 0.2609417 0.8995075 4.0000000 1.00000 1.00000
Si core 0.1912091 0.7408107 0.5993608 4.0000000 1.00000 1.00000
Si core 0.2145637 0.2627683 0.3976353 4.0000000 1.00000 1.00000
Si core 0.3837670 0.9745997 0.1737217 4.0000000 1.00000 1.00000
Si core 0.3804971 0.4713996 0.8261526 4.0000000 1.00000 1.00000
Si core 0.6346706 0.9723614 0.6759931 4.0000000 1.00000 1.00000
Si core 0.6281840 0.4732338 0.3287919 4.0000000 1.00000 1.00000
Si core 0.8797330 0.9719652 0.1750576 4.0000000 1.00000 1.00000
Si core 0.8844878 0.4735893 0.8276898 4.0000000 1.00000 1.00000
Si core 0.1294488 0.9721945 0.6726538 4.0000000 1.00000 1.00000
Si core 0.1330319 0.4739444 0.3255323 4.0000000 1.00000 1.00000
O core 0.3912761 0.5131251 0.1218726 0.8480000 1.00000 1.00000
O core 0.3730313 0.0071957 0.8718275 0.8480000 1.00000 1.00000
O core 0.6440373 0.5132582 0.6236113 0.8480000 1.00000 1.00000
O core 0.6209554 0.0075333 0.3744651 0.8480000 1.00000 1.00000
O core 0.8723166 0.5077116 0.1294040 0.8480000 1.00000 1.00000
O core 0.8923061 0.0122367 0.8797925 0.8480000 1.00000 1.00000

O core 0.1212804 0.5061533 0.6269851 0.8480000 1.00000 1.00000
O core 0.1420429 0.0142249 0.3777050 0.8480000 1.00000 1.00000
O core 0.3937427 0.1922011 0.1531508 0.8480000 1.00000 1.00000
O core 0.3857763 0.6888427 0.8448392 0.8480000 1.00000 1.00000
O core 0.6497392 0.1962136 0.6563522 0.8480000 1.00000 1.00000
O core 0.6298912 0.6854018 0.3485493 0.8480000 1.00000 1.00000
O core 0.8851312 0.1895454 0.1563896 0.8480000 1.00000 1.00000
O core 0.8944389 0.6908326 0.8484981 0.8480000 1.00000 1.00000
O core 0.1302981 0.1835765 0.6528978 0.8480000 1.00000 1.00000
O core 0.1480905 0.6975516 0.3452211 0.8480000 1.00000 1.00000
O core 0.4895495 0.5412772 0.2073330 0.8480000 1.00000 1.00000
O core 0.4950654 0.0448578 0.7926587 0.8480000 1.00000 1.00000
O core 0.7404673 0.5444199 0.7096650 0.8480000 1.00000 1.00000
O core 0.7421049 0.0397656 0.2953197 0.8480000 1.00000 1.00000
O core 0.9942599 0.5454220 0.2086091 0.8480000 1.00000 1.00000
O core 0.9903644 0.0396980 0.7943089 0.8480000 1.00000 1.00000
O core 0.2435527 0.5391195 0.7057989 0.8480000 1.00000 1.00000
O core 0.2391343 0.0462895 0.2918708 0.8480000 1.00000 1.00000
O core 0.2590323 0.2986307 0.1981529 0.8480000 1.00000 1.00000
O core 0.2614262 0.8016274 0.7940185 0.8480000 1.00000 1.00000
O core 0.5095701 0.2972237 0.6990282 0.8480000 1.00000 1.00000
O core 0.5091711 0.8021614 0.2966186 0.8480000 1.00000 1.00000
O core 0.7606299 0.3022657 0.2072464 0.8480000 1.00000 1.00000
O core 0.7600425 0.7975026 0.8034973 0.8480000 1.00000 1.00000
O core 0.0106652 0.3006390 0.7051841 0.8480000 1.00000 1.00000
O core 0.0082235 0.7981502 0.3021643 0.8480000 1.00000 1.00000
O core 0.4137980 0.1955211 0.9525075 0.8480000 1.00000 1.00000
O core 0.4617932 0.7799520 0.0478609 0.8480000 1.00000 1.00000
O core 0.6624675 0.1962881 0.4548447 0.8480000 1.00000 1.00000
O core 0.7128924 0.7802085 0.5495922 0.8480000 1.00000 1.00000
O core 0.9623543 0.2800347 0.9536316 0.8480000 1.00000 1.00000
O core 0.9135140 0.6958634 0.0487218 0.8480000 1.00000 1.00000
O core 0.2119396 0.2804348 0.4517845 0.8480000 1.00000 1.00000
O core 0.1624241 0.6953565 0.5465895 0.8480000 1.00000 1.00000
O core 0.3962310 0.8655916 0.1259974 0.8480000 1.00000 1.00000
O core 0.3870317 0.3667672 0.8759885 0.8480000 1.00000 1.00000
O core 0.6496208 0.8674845 0.6279994 0.8480000 1.00000 1.00000
O core 0.6316885 0.3626429 0.3781797 0.8480000 1.00000 1.00000
O core 0.8866741 0.8676240 0.1252069 0.8480000 1.00000 1.00000
O core 0.8965472 0.3638861 0.8753418 0.8480000 1.00000 1.00000
O core 0.1324160 0.8616639 0.6232311 0.8480000 1.00000 1.00000
O core 0.1489587 0.3695536 0.3733925 0.8480000 1.00000 1.00000
O core 0.2584915 0.8194958 0.1986172 0.8480000 1.00000 1.00000
O core 0.2565601 0.3133477 0.8006157 0.8480000 1.00000 1.00000
O core 0.5065843 0.8152902 0.6982852 0.8480000 1.00000 1.00000
O core 0.5070983 0.3188863 0.3009806 0.8480000 1.00000 1.00000
O core 0.7557665 0.8138581 0.2005439 0.8480000 1.00000 1.00000
O core 0.7593378 0.3187210 0.8027075 0.8480000 1.00000 1.00000

O core 0.0088520 0.8173375 0.7008088 0.84800000 1.00000 1.00000
O core 0.0049316 0.3161848 0.3033624 0.84800000 1.00000 1.00000
O core 0.4903446 0.0455267 0.2101225 0.84800000 1.00000 1.00000
O core 0.4903956 0.5410842 0.7917918 0.84800000 1.00000 1.00000
O core 0.7391422 0.0379814 0.7131266 0.84800000 1.00000 1.00000
O core 0.7398801 0.5473740 0.2951262 0.84800000 1.00000 1.00000
O core 0.9895190 0.0417529 0.2095256 0.84800000 1.00000 1.00000
O core 0.9912234 0.5447881 0.7913707 0.84800000 1.00000 1.00000
O core 0.2415046 0.0470490 0.7061076 0.84800000 1.00000 1.00000
O core 0.2374101 0.5402064 0.2883077 0.84800000 1.00000 1.00000
Oh core 0.0873815 0.8759926 0.1135407 0.90000000 1.00000 1.00000
Oh core 0.1052236 0.3899780 0.8808668 0.90000000 1.00000 1.00000
Oh core 0.3356983 0.8774980 0.6116227 0.90000000 1.00000 1.00000
Oh core 0.3555783 0.3908892 0.3792846 0.90000000 1.00000 1.00000
Oh core 0.6045617 0.8903474 0.1206075 0.90000000 1.00000 1.00000
Oh core 0.5879091 0.3756836 0.8877518 0.90000000 1.00000 1.00000
Oh core 0.8569420 0.8906878 0.6220104 0.90000000 1.00000 1.00000
Oh core 0.8352082 0.3790152 0.3895716 0.90000000 1.00000 1.00000
Hh core 0.1572603 0.9485796 0.1088974 0.40000000 1.00000 1.00000
Hh core 0.1756807 0.4429481 0.8828921 0.40000000 1.00000 1.00000
Hh core 0.4053953 0.9506852 0.6065439 0.40000000 1.00000 1.00000
Hh core 0.4260720 0.4452920 0.3812284 0.40000000 1.00000 1.00000
Hh core 0.6749983 0.9431010 0.1186081 0.40000000 1.00000 1.00000
Hh core 0.6577657 0.4484382 0.8923965 0.40000000 1.00000 1.00000
Hh core 0.9275351 0.9464023 0.6202621 0.40000000 1.00000 1.00000
Hh core 0.9049383 0.4520246 0.3945599 0.40000000 1.00000 1.00000
Ow core 0.1675688 0.4578113 0.1279016 -0.8200000 1.00000 1.00000
Hw core 0.2137452 0.3977449 0.1135035 0.41000000 1.00000 1.00000
Hw core 0.2030440 0.6087229 0.1140577 0.41000000 1.00000 1.00000
Ow core 0.1622939 0.9676823 0.8683016 -0.8200000 1.00000 1.00000
Hw core 0.2197833 0.9221749 0.8766128 0.41000000 1.00000 1.00000
Hw core 0.2039109 0.1275839 0.8775289 0.41000000 1.00000 1.00000
Ow core 0.4191826 0.4573995 0.6282648 -0.8200000 1.00000 1.00000
Hw core 0.4653846 0.3974269 0.6138961 0.41000000 1.00000 1.00000
Hw core 0.4583141 0.6126500 0.6163635 0.41000000 1.00000 1.00000
Ow core 0.4108535 0.9695829 0.3690855 -0.8200000 1.00000 1.00000
Hw core 0.4666708 0.9206270 0.3776506 0.41000000 1.00000 1.00000
Hw core 0.4523669 0.1272087 0.3800321 0.41000000 1.00000 1.00000
Ow core 0.6615742 0.4680536 0.1330831 -0.8200000 1.00000 1.00000
Hw core 0.7190122 0.4224424 0.1247735 0.41000000 1.00000 1.00000
Hw core 0.7032402 0.6279269 0.1238141 0.41000000 1.00000 1.00000
Ow core 0.6680456 0.9573872 0.8733037 -0.8200000 1.00000 1.00000
Hw core 0.7140161 0.8973686 0.8879152 0.41000000 1.00000 1.00000
Hw core 0.7036560 0.1087239 0.8869456 0.41000000 1.00000 1.00000
Ow core 0.9115812 0.4689548 0.6323173 -0.8200000 1.00000 1.00000
Hw core 0.9674713 0.4205262 0.6234831 0.41000000 1.00000 1.00000
Hw core 0.9524601 0.6264142 0.6213096 0.41000000 1.00000 1.00000
Ow core 0.9179622 0.9577684 0.3728966 -0.8200000 1.00000 1.00000

Hw core 0.9641943 0.8980835 0.3873888 0.4100000 1.00000 1.00000
Hw core 0.9566184 0.1128107 0.3848375 0.4100000 1.00000 1.00000
Ow core 0.9647967 0.7486163 0.9421380 -0.8200000 1.00000 1.00000
Hw core 0.9805968 0.7739792 0.9067784 0.4100000 1.00000 1.00000
Hw core 0.9223374 0.8254780 0.9515681 0.4100000 1.00000 1.00000
Ow core 0.9618151 0.3305835 0.0592055 -0.8200000 1.00000 1.00000
Hw core 0.9414138 0.2805615 0.0933788 0.4100000 1.00000 1.00000
Hw core 0.0223677 0.2914381 0.0483481 0.4100000 1.00000 1.00000
Ow core 0.2112103 0.7453008 0.4402988 -0.8200000 1.00000 1.00000
Hw core 0.2281381 0.7725020 0.4050224 0.4100000 1.00000 1.00000
Hw core 0.1698614 0.8239436 0.4499210 0.4100000 1.00000 1.00000
Ow core 0.2125891 0.3324668 0.5575245 -0.8200000 1.00000 1.00000
Hw core 0.1908340 0.2796015 0.5914652 0.4100000 1.00000 1.00000
Hw core 0.2726906 0.2923233 0.5465628 0.4100000 1.00000 1.00000
Ow core 0.4619437 0.8306668 0.9421008 -0.8200000 1.00000 1.00000
Hw core 0.4416667 0.7804813 0.9079326 0.4100000 1.00000 1.00000
Hw core 0.5224631 0.7916089 0.9530530 0.4100000 1.00000 1.00000
Ow core 0.4645411 0.2486724 0.0591432 -0.8200000 1.00000 1.00000
Hw core 0.4800004 0.2743799 0.0945121 0.4100000 1.00000 1.00000
Hw core 0.4221726 0.3254556 0.0494762 0.4100000 1.00000 1.00000
Ow core 0.7124810 0.8326600 0.4437209 -0.8200000 1.00000 1.00000
Hw core 0.6906476 0.7805116 0.4097362 0.4100000 1.00000 1.00000
Hw core 0.7726285 0.7923725 0.4545137 0.4100000 1.00000 1.00000
Ow core 0.7115204 0.2452750 0.5610536 -0.8200000 1.00000 1.00000
Hw core 0.7285159 0.2721474 0.5963301 0.4100000 1.00000 1.00000
Hw core 0.6701967 0.3241154 0.5515503 0.4100000 1.00000 1.00000
Ow core 0.2379195 0.8273982 0.9759001 -0.8200000 1.00000 1.00000
Hw core 0.2385341 0.7580174 0.9450736 0.4100000 1.00000 1.00000
Hw core 0.2500582 0.9734503 0.9671612 0.4100000 1.00000 1.00000
Ow core 0.4884225 0.8268797 0.4768701 -0.8200000 1.00000 1.00000
Hw core 0.4902641 0.7583979 0.4460803 0.4100000 1.00000 1.00000
Hw core 0.5028965 0.9749176 0.4682683 0.4100000 1.00000 1.00000
Ow core 0.7377879 0.3273978 0.0253253 -0.8200000 1.00000 1.00000
Hw core 0.7381007 0.2578447 0.0561740 0.4100000 1.00000 1.00000
Hw core 0.7500044 0.4735203 0.0340610 0.4100000 1.00000 1.00000
Ow core 0.9878829 0.3267183 0.5243727 -0.8200000 1.00000 1.00000
Hw core 0.9895292 0.2576515 0.5551020 0.4100000 1.00000 1.00000
Hw core 0.0024790 0.4747556 0.5330640 0.4100000 1.00000 1.00000
Ow core 0.1149735 0.2739186 0.0152873 -0.8200000 1.00000 1.00000
Hw core 0.2003174 0.3039545 0.0124812 0.4100000 1.00000 1.00000
Hw core 0.0835256 0.2794042 0.9830743 0.4100000 1.00000 1.00000
Ow core 0.3631260 0.2701080 0.5136812 -0.8200000 1.00000 1.00000
Hw core 0.4493828 0.3033481 0.5119354 0.4100000 1.00000 1.00000
Hw core 0.3338643 0.2784224 0.4812137 0.4100000 1.00000 1.00000
Ow core 0.6147850 0.7740433 0.9862522 -0.8200000 1.00000 1.00000
Hw core 0.7001208 0.8039627 0.9889504 0.4100000 1.00000 1.00000
Hw core 0.5834641 0.7793829 0.0185023 0.4100000 1.00000 1.00000
Ow core 0.8634029 0.7703785 0.4872947 -0.8200000 1.00000 1.00000

Hw core 0.9495676 0.8033601 0.4891497 0.4100000 1.00000 1.00000
Hw core 0.8338640 0.7779839 0.5197584 0.4100000 1.00000 1.00000
Ow core 0.3419967 0.3821181 0.0085980 -0.8200000 1.00000 1.00000
Hw core 0.3836328 0.3604304 0.9810622 0.4100000 1.00000 1.00000
Hw core 0.3921889 0.5427083 0.0179386 0.4100000 1.00000 1.00000
Ow core 0.5909998 0.3834651 0.5106329 -0.8200000 1.00000 1.00000
Hw core 0.6331652 0.3610868 0.4834473 0.4100000 1.00000 1.00000
Hw core 0.6419492 0.5437993 0.5201044 0.4100000 1.00000 1.00000
Ow core 0.8417732 0.8819321 0.9925659 -0.8200000 1.00000 1.00000
Hw core 0.8833763 0.8599771 0.0200659 0.4100000 1.00000 1.00000
Hw core 0.8920924 0.0426474 0.9833387 0.4100000 1.00000 1.00000
Ow core 0.0911835 0.8834107 0.4908435 -0.8200000 1.00000 1.00000
Hw core 0.1333037 0.8612023 0.5180789 0.4100000 1.00000 1.00000
Hw core 0.1418975 0.0438293 0.4814034 0.4100000 1.00000 1.00000
O shel 0.3972086 0.5258706 0.1243275 -2.8479999 1.00000 1.00000
O shel 0.3791793 0.0170054 0.8699919 -2.8479999 1.00000 1.00000
O shel 0.6497985 0.5259994 0.6260856 -2.8479999 1.00000 1.00000
O shel 0.6270839 0.0172606 0.3725927 -2.8479999 1.00000 1.00000
O shel 0.8784741 0.5175393 0.1312619 -2.8479999 1.00000 1.00000
O shel 0.8981883 0.0249258 0.8773334 -2.8479999 1.00000 1.00000
O shel 0.1274580 0.5158591 0.6288552 -2.8479999 1.00000 1.00000
O shel 0.1479177 0.0270382 0.3752603 -2.8479999 1.00000 1.00000
O shel 0.3921425 0.1909132 0.1565719 -2.8479999 1.00000 1.00000
O shel 0.3849798 0.6881946 0.8415298 -2.8479999 1.00000 1.00000
O shel 0.6474376 0.1943461 0.6595581 -2.8479999 1.00000 1.00000
O shel 0.6296091 0.6852597 0.3450871 -2.8479999 1.00000 1.00000
O shel 0.8843216 0.1888684 0.1596949 -2.8479999 1.00000 1.00000
O shel 0.8928544 0.6896746 0.8450656 -2.8479999 1.00000 1.00000
O shel 0.1301183 0.1835168 0.6563515 -2.8479999 1.00000 1.00000
O shel 0.1457819 0.6956138 0.3419759 -2.8479999 1.00000 1.00000
O shel 0.4806514 0.5288038 0.2042631 -2.8479999 1.00000 1.00000
O shel 0.4853278 0.0321078 0.7955429 -2.8479999 1.00000 1.00000
O shel 0.7317989 0.5320414 0.7065849 -2.8479999 1.00000 1.00000
O shel 0.7322342 0.0270141 0.2981714 -2.8479999 1.00000 1.00000
O shel 0.9845352 0.5326649 0.2057075 -2.8479999 1.00000 1.00000
O shel 0.9814478 0.0272170 0.7973124 -2.8479999 1.00000 1.00000
O shel 0.2336392 0.5263179 0.7029443 -2.8479999 1.00000 1.00000
O shel 0.2303947 0.0337500 0.2949336 -2.8479999 1.00000 1.00000
O shel 0.2694983 0.3062174 0.1959785 -2.8479999 1.00000 1.00000
O shel 0.2713527 0.8090114 0.7965841 -2.8479999 1.00000 1.00000
O shel 0.5202343 0.3051095 0.6968611 -2.8479999 1.00000 1.00000
O shel 0.5189926 0.8091707 0.2991234 -2.8479999 1.00000 1.00000
O shel 0.7705817 0.3096436 0.2046655 -2.8479999 1.00000 1.00000
O shel 0.7705179 0.8050786 0.8056579 -2.8479999 1.00000 1.00000
O shel 0.0204916 0.3078002 0.7026418 -2.8479999 1.00000 1.00000
O shel 0.0188705 0.8060552 0.3043364 -2.8479999 1.00000 1.00000
O shel 0.4171355 0.1979748 0.9472604 -2.8479999 1.00000 1.00000
O shel 0.4618004 0.7804594 0.0531737 -2.8479999 1.00000 1.00000

O shel 0.6656350 0.1987218 0.4495613 -2.8479999 1.00000 1.00000
O shel 0.7129899 0.7807064 0.5548937 -2.8479999 1.00000 1.00000
O shel 0.9623712 0.2804462 0.9483087 -2.8479999 1.00000 1.00000
O shel 0.9168247 0.6983467 0.0539700 -2.8479999 1.00000 1.00000
O shel 0.2119993 0.2810329 0.4464689 -2.8479999 1.00000 1.00000
O shel 0.1656602 0.6976944 0.5518671 -2.8479999 1.00000 1.00000
O shel 0.4013990 0.8653069 0.1280602 -2.8479999 1.00000 1.00000
O shel 0.3915225 0.3638071 0.8737685 -2.8479999 1.00000 1.00000
O shel 0.6544902 0.8666117 0.6300219 -2.8479999 1.00000 1.00000
O shel 0.6366546 0.3607121 0.3759785 -2.8479999 1.00000 1.00000
O shel 0.8911175 0.8646199 0.1274452 -2.8479999 1.00000 1.00000
O shel 0.9017935 0.3637598 0.8733189 -2.8479999 1.00000 1.00000
O shel 0.1374086 0.8597009 0.6254727 -2.8479999 1.00000 1.00000
O shel 0.1536927 0.3684980 0.3714029 -2.8479999 1.00000 1.00000
O shel 0.2693298 0.8330576 0.1963961 -2.8479999 1.00000 1.00000
O shel 0.2671910 0.3271357 0.8028744 -2.8479999 1.00000 1.00000
O shel 0.5177659 0.8291155 0.6962404 -2.8479999 1.00000 1.00000
O shel 0.5175249 0.3321636 0.3033993 -2.8479999 1.00000 1.00000
O shel 0.7664147 0.8276519 0.1982742 -2.8479999 1.00000 1.00000
O shel 0.7701728 0.3322842 0.8049238 -2.8479999 1.00000 1.00000
O shel 0.0191287 0.8307686 0.6983718 -2.8479999 1.00000 1.00000
O shel 0.0161536 0.3301467 0.3053781 -2.8479999 1.00000 1.00000
O shel 0.4816084 0.0397044 0.2071170 -2.8479999 1.00000 1.00000
O shel 0.4813641 0.5352870 0.7947744 -2.8479999 1.00000 1.00000
O shel 0.7306548 0.0324655 0.7100078 -2.8479999 1.00000 1.00000
O shel 0.7306110 0.5412476 0.2979743 -2.8479999 1.00000 1.00000
O shel 0.9804955 0.0359475 0.2065168 -2.8479999 1.00000 1.00000
O shel 0.9824659 0.5389105 0.7943517 -2.8479999 1.00000 1.00000
O shel 0.2321819 0.0408709 0.7032446 -2.8479999 1.00000 1.00000
O shel 0.2290297 0.5344818 0.2914249 -2.8479999 1.00000 1.00000
Oh shel 0.0733654 0.8628792 0.1128677 -2.2999999 1.00000 1.00000
Oh shel 0.0920697 0.3783365 0.8820495 -2.2999999 1.00000 1.00000
Oh shel 0.3216731 0.8641113 0.6109551 -2.2999999 1.00000 1.00000
Oh shel 0.3423095 0.3792350 0.3804332 -2.2999999 1.00000 1.00000
Oh shel 0.5914080 0.8787297 0.1194447 -2.2999999 1.00000 1.00000
Oh shel 0.5738824 0.3625432 0.8884323 -2.2999999 1.00000 1.00000
Oh shel 0.8436457 0.8789009 0.6208441 -2.2999999 1.00000 1.00000
Oh shel 0.8211878 0.3656358 0.3902744 -2.2999999 1.00000 1.00000

species 9

Ca core 2.000000
Si core 4.000000
O core 0.848000
O shel -2.848000
Oh core 0.900000
Oh shel -2.300000
Hh core 0.400000
Ow core -0.820000
Hw core 0.410000

buck inter
 Ca core O shel 1090.40000 0.343700 0.000000 0.00 11.00
 buck inter
 Ca core Oh shel 2170.00000 0.297000 0.000000 0.00 11.00
 lennard inter
 Ca core Ow core 7591.3896 5.3709660 0.000 11.000
 buck inter
 Si core O shel 1283.90700 0.320520 10.66200 0.00 11.00
 buck inter
 Si core Oh shel 983.556000 0.320530 10.66160 0.00 11.00
 buck inter
 Si core Ow core 1283.90700 0.320520 10.66200 0.00 11.00
 buck inter
 O shel O shel 22764.0000 0.149000 27.88000 0.00 11.00
 buck inter
 Hh core O shel 311.970000 0.250000 0.000000 0.00 11.00
 buck inter
 Hw core O shel 311.970000 0.250000 0.000000 0.00 11.00
 buck inter
 O shel Oh shel 22764.0000 0.149000 13.94000 0.00 11.00
 buck inter
 Ow core O shel 22764.0000 0.149000 15.46000 0.00 11.00
 buck inter
 Oh shel Oh shel 22764.0000 0.149000 6.970000 0.00 11.00
 buck inter
 Hh core Oh shel 436.760000 0.250000 2.500000 0.00 11.00
 lennard inter
 Ow core Oh shel 27290.8535 27.12246 0.00 11.00
 lennard inter
 Ow core Ow core 27277.653 27.111883 0.000 11.000
 harmonic intra bond
 Ow core Hw core 45.9296 1.012
 morse intra
 Oh shel Hh core 7.0525 3.1749 0.9485 0.000 0.000 1.20000
 spring
 O 74.920380
 spring
 Oh 74.920000
 three inter
 Si core O shel O shel 2.09724 109.47 0.0 1.8 0.0 1.8 0.0 3.2
 three inter
 Si core Oh shel Oh shel 2.09724 109.47 0.0 1.8 0.0 1.8 0.0 3.2
 three inter
 Si core Oh shel O shel 2.09724 109.47 0.0 1.8 0.0 1.8 0.0 3.2
 three intra bond
 Ow core Hw core Hw core 3.2913 113.24
 cutp 11.00000 1.00000
 cutd 3.6000

```
shellmass  
O 0.012500  
accuracy 5  
#switch_min rfo gnorm 1.00  
dump tob.restart  
output cif Tobermorite341.cif
```

Appendix B: DLPOLY 4 Input Files

All molecular dynamics simulations were done using DLPOLY 4¹⁰¹ and DLPOLY classic¹⁰², which require three input files: CONTROL, FIELD, and CONFIG. CONTROL file has all the simulation details and controlling parameters. The FIELD file is composed of the full description of the number of the examined species, their charges and masses, and the interatomic and intramolecular interactions between them. Finally, the CONFIG file is composed of the spatial coordinates of each particle in the examined structure. It can also contain their velocities and forces. In the following, and for the DLPOLY 4, we represent a CONTROL file from one of the production simulations for the interfacial system done in the NVT ensemble. We then present a FIELD file using the adopted force field to examine the interfacial 5% Na-doped structure with Na⁺ and Cl⁻ ions inserted in the pore. Finally, we present a FIELD file for the ClayFF force field used in the undoped bulk solid system simulations.

DLPOLY 4 CONTROL File

```
CONTROL file
ensemble nvt hoover 0.5 #relaxation time 0.5 ps
temperature 300.0
pressure 0.0
timestep 1.0E-4 #time step 0.1 fs
steps 4100.0E4
equilibration 100.0E4 #velocity rescaling 1st 100 ps
print 500 #printing stats every 50 fs
stack 500
stats 500
scale 10 #scaling every 10 fs in 1st 100 ps
traj 1100.0E4 1000 1 #trajectory recording after 1.1 ns
ewald precision 1.0E-7
dump 1000
cutoff 11.0
rvdw cutoff 11.0
job time 1.00E10
delr width 1.0
close time 1000
finish
```

DLPOLY4 Core-Shell FIELD File for Interfacial System

```
#FIELD FILE
UNITS eV
MOLECULES 7
Ca CORE
NUMMOL 228
atoms 1
Ca 40.078 2.000
finish
Si CORE
NUMMOL 288
atoms 1
Si 28.085 4.000
finish
Na
NUMMOL 25
atoms 1
Na 22.989769 1.00
finish
Cl
NUMMOL 13
atoms 1
Cl 35.453 -1.00
finish
OS CORE
NUMMOL 744
atoms 2
Osc 15.800 0.8480
Oss 0.2000 -2.848
shell 1
1 2 74.92038
finish
HYDROXYL
NUMMOL 132
atoms 3
Ohc 15.800 0.900
Ohs 0.2000 -2.30
Hh 1.008 0.400
shell 1
1 2 74.92038
bonds 1
mors 2 3 7.052500 0.9485 3.174900
finish
WATER
NUMMOL 1798
atoms 3
Ow 15.966 -0.820
```

Hw 1.0080 0.4100
Hw 1.0080 0.4100
bonds 2
harm 1 2 45.9296 1.012
harm 1 3 45.9296 1.012
angles 1
harm 2 1 3 3.2913 113.24
finish
VDW 27
Ca Oss buck 1090.4 0.343700 0.00000
Ca Ohs buck 2170.00 0.297 0.00000
Ca Ow 12-6 7591.38961 5.370966
Si Oss buck 1283.907 0.32052 10.6620
Si Ohs buck 983.5560 0.32052 10.6616
Si Ow buck 1283.907 0.32052 10.6620
Oss Oss buck 22764.0 0.1490 27.8800
Oss Ohs buck 22764.00 0.14900 13.9400
Oss Ow buck 22764.00 0.14900 15.4600
Oss Hh buck 311.9700 0.25000 0.00000
Oss Hw buck 311.9700 0.25000 0.00000
Ohs Ohs buck 22764.0 0.149 6.97000
Ohs Ow 12-6 27290.8535 27.12246
Ohs Hh buck 436.760 0.250 2.50000
Ow Ow 12-6 27277.653 27.1118827
Na Na 12-6 629.28451 6.20414
Na Cl 12-6 38686.4449 21.22653
Cl Cl 12-6 357879.44529 28.171481
Na Ow 12-6 5153.64755 14.46646
Cl Ow 12-6 128934.91023 31.57414
Na Oss buck 1226.84 0.3065 0.0
Na Ohs buck 858.79 0.3065 0.0
Cl Oss buck 1272.25 0.2352 28.46
Cl Ohs buck 1272.25 0.2352 14.23
Cl Ca 12-6 28867.62853 1.88492
Cl Si 12-6 792.040526 0.242832
Cl Hh nm 0.03001596 9 6 2.379861112
tbp 3
Oss Si Oss harm 2.09724 109.47 0 0 1.8
Ohs Si Ohs harm 2.09724 109.47 0 0 1.8
Ohs Si Oss harm 2.09724 109.47 0 0 1.8
CLOSE

DLPOLY4 ClayFF FIELD File for Bulk Solid System

```
#FIELD FILE
Tobermorite
UNITS eV
MOLECULES 5
Ca CORE
NUMMOL 240
atoms 1
Ca 40.078 1.30038461538
finish
Si CORE
NUMMOL 288
atoms 1
Si 28.085 2.04038461538
finish
OS CORE
NUMMOL 768
atoms 1
Osc 16.0000 -1.093055555556
finish
HYDROXYL
NUMMOL 96
atoms 2
Ohc 16.0000 -0.993055555556
Hh 1.008 0.36538461538
bonds 1
mors 1 2 5.7347177 0.9572 2.1350
finish
WATER
NUMMOL 336
atoms 3
Ow 15.966 -0.820
Hw 1.0080 0.410
Hw 1.0080 0.410
bonds 2
harm 1 2 48.054600 1.0
harm 1 3 48.054600 1.0
angles 1
harm 2 1 3 3.96914 109.47
finish
VDW 15
Ca Osc lj 3.8337e-5 4.3661164378
Ca Ohc lj 3.8337e-5 4.3661164378
Ca Ow lj 3.8337e-5 4.3661164378
Ca Ca lj 2.1811e-7 5.56669
Ca Si lj 1.3194e-7 4.434359
Si Osc lj 2.3191e-5 3.233784
```

Si Ohc lj 2.3191e-5 3.233784
Si Ow lj 2.3191e-5 3.233784
Si Si lj 7.9810e-8 3.302027
Osc Osc lj 0.0067386 3.165541
Osc Ohc lj 0.0067386 3.165541
Osc Ow lj 0.0067386 3.165541
Ohc Ohc lj 0.0067386 3.165541
Ohc Ow lj 0.0067386 3.165541
Ow Ow lj 0.0067386 3.165541
tbp 2
Si Ohc Hh harm 1.30089 100.00 0.0 0.0 1.8
Ca Ohc Hh harm 0.520356 109.47 0.0 0.0 2.8
CLOSE

Appendix C: C++ Code for Output Processing

After the simulations were done, coded post-processing tools were used to analyze the atoms' trajectories produced. In the following, we present two scripts written using C++: firstly, to calculate the MSD, which is then used to calculate the diffusion coefficient of the ions, and secondly, to calculate the 2-D contour plots of the surface species. This MSD code is for Cl⁻ ions on the surface of the undoped tobermorite interface in the 1st 4.1 ns simulation (out of the total 12 ns simulations). The output of this was then fitted to a straight line using python, and the slope of the line was used to calculate the diffusion coefficient of the examined species. Secondly, we show the C++ code used to calculate the 2-D density of species on the surface of the interfacial structure. Similarly, the output of this code was written in a way that is readable by the python programming language to plot the 2-D contour plots shown in **Figure 12**.

MSD C++ CODE

```
#include <iostream>
#include <fstream>
#include <cmath>
#include <math.h>
#include <ctime>
#include <sstream>
#include <string>
#include <vector>
#include <omp.h>
#include <stdio.h>
#include <cstdlib>
#include <string>
#include <ctime>
#include <numeric>
#include <thread>
#include <chrono>
#include <mutex>
using namespace std;
////////////////////////////////////
Variables that are specific to the tested case
```



```

void msd (double coor_t[test_atoms][3], double coor_p[test_atoms][3], double
coor_abs[test_atoms][3]){
    for(i=0; i<test_atoms; i++){
        swapd[0]=coor_t[i][0];
        swapd[1]=coor_t[i][1];
        swapd[2]=coor_t[i][2];

    check: dd[0]=int((coor_t[i][0]-coor_p[i][0])/(lx/2.0));
        dd[1]=int((coor_t[i][1]-coor_p[i][1])/(ly/2.0));
        dd[2]=int((coor_t[i][2]-coor_p[i][2])/(lz/2.0));
        for(j=0; j<3; j++){
            if(dd[j] > 1){
                dd[j]=1;
            }else if(dd[j]<-1){
                dd[j]=-1;
            }
        }
        if(dd[2] < 0){
            coor_t[i][2]+=lz;
            coor_t[i][1]+=zy;
            coor_t[i][0]+=zx;
            goto check;
        } else if(dd[2] > 0){
            coor_t[i][2]-=lz;
            coor_t[i][1]-=zy;
            coor_t[i][0]-=zx;
            goto check;
        }
        if(dd[1] < 0){
            coor_t[i][1]+=ly;
            coor_t[i][0]+=yx;
            goto check;
        } else if(dd[1] > 0){
            coor_t[i][1]-=ly;
            coor_t[i][0]-=yx;
            goto check;
        }
        if(dd[0] < 0){
            coor_t[i][0]+=lx;
            goto check;
        } else if(dd[0] > 0){
            coor_t[i][0]-=lx;
            goto check;
        }
        for(j=0; j<3; j++){
            del[j]=coor_t[i][j]-coor_p[i][j];
            coor_abs[i][j]=coor_abs[i][j]+del[j];
            coor_p[i][j]=swapd[j];
        }
    }
}

```



```
        outfile << r2t[k] << endl;
    }
else{
    r2t[k]=(r2t[k])/(atom_count_ave*time[k]);
    outfile << r2t[k] << endl;
}
}
infile.close();
outfile.close();
////////////////////////////////////
////////////////////////////////////
tend = time(0);
cout << "It took "<< difftime(tend, tstart) <<" second(s)." << endl;

return 0;
}
```

2-D CONTOUR PLOT C++ CODE

```
#include <iostream>
#include <fstream>
#include <cmath>
#include <math.h>
#include <ctime>
#include <sstream>
#include <string>
#include <vector>
#include <omp.h>
#include <stdio.h>
#include <cstdlib>
#include <string>
#include <ctime>
#include <numeric>
#include <thread>
#include <chrono>
#include <mutex>
using namespace std;
vector <vector<double>> den;
/////////////////////////////////////////////////////////////////
// Variables that are specific to the tested case
/////////////////////////////////////////////////////////////////
const int frames=30001; // no. of frames
const int atoms=7808;
const double bin_width=0.2; //bin width
const double lower_limit=23;
const double upper_limit=30;
const int ca=240, si= 288, na=13, cl=13, os=768*2, oh=96*3, ow=1820*3;
const double lx = 40.7936000000;
const double yx = -15.815400000, ly = 24.696000000;
const double zx = 0.05805800000, zy = 0.1098640000, lz = 71.91290000;
/////////////////////////////////////////////////////////////////
// constants to the code
/////////////////////////////////////////////////////////////////
const int N=3;
const int rows=2;
const int columns=3;
const double one=1.0;
const double PI=3.14159265;
const double fract=1.3333;
const double ang=180.0;
int lpf=(atoms*3+4); //lines per frame
string line; //string that will contain imported lines
int count=0; //read lines counter
int first=0; //start of file counter
```

```

int last=lpf-1; //end of file counter
double atoms_coor[atoms][3]; //array that will contain atoms
coordinates of each frame
int i=0; //counter of lines in each frame to skip
dimensions and velocities
int l=0; // atoms counter in the array that contains only
coordinates
int s=1; //no. of frames counter
int bin_nox, bin_noy; //bin number while binning
double bin_volume=0;
double dist=0; //distance between two atoms
////////////////////////////////////////////////////////////////////////////////////////////////////////////////////////////////
////////////////////////////////////////////////////////////////////////////////////////////////////////////////////////////////
void geomtry(double atoms, double bin_width, double *volume, double *rho, double *length, int
*binsx, int *binsy){
    double a=lx;
    double b=sqrt(yx*yx+ly*ly);
    double c=sqrt(zx*zx+zy*zy+lz*lz);
    double alpha= acos((yx*zx+ly*zy)/(b*c)) *ang/PI;
    double beta= acos((lx*zx)/(a*c)) *ang/PI;
    double gamma= acos((lx*yx)/(a*b)) *ang/PI;
    *volume= a*b*c*sqrt(1-pow(cos(alpha*PI/ang),2)-pow(cos(beta*PI/ang),2)-
pow(cos(gamma*PI/ang),2)+2*cos(alpha*PI/ang)*cos(beta*PI/ang)*cos(gamma*PI/ang));
    /*rho=(ox_atoms)/(*volume); // Calculating cell uniform density
    /*length=0.5*smallest_dimension; //maximum search is 50% of smallest dimension
    *binsx=ceil((a-yx)/bin_width);
    *binsy=ceil(ly/bin_width);
    cout << "binsx " << *binsx << " binsy " << *binsy << endl;
    bin_volume= bin_width*bin_width*c*sqrt(1-pow(cos(alpha*PI/ang),2)-
pow(cos(beta*PI/ang),2)-
pow(cos(gamma*PI/ang),2)+2*cos(alpha*PI/ang)*cos(beta*PI/ang)*cos(gamma*PI/ang));
}
////////////////////////////////////////////////////////////////////////////////////////////////////////////////////////////////
////////////////////////////////////////////////////////////////////////////////////////////////////////////////////////////////
void binning(int binsx, int binsy, double bin_width, double rho, int atoms, int frames){
    ofstream outfile;
    outfile.open("2d_den_Ow.py");
    for(int x=0; x<binsx; x++){
        for(int y=0; y<binsy; y++){
            den[x][y]=den[x][y]/frames;
            den[x][y]=den[x][y]/bin_volume;
            outfile << x*bin_width << " " << y*bin_width << " " << den[x][y] << endl;
        }
    }
    outfile.close();
}
////////////////////////////////////////////////////////////////////////////////////////////////////////////////////////////////
////////////////////////////////////////////////////////////////////////////////////////////////////////////////////////////////

```



```

        if(atoms_coor[i][2]>80){
            atoms_coor[i][2] -= lz;
        }
        if(atoms_coor[i][2]< upper_limit && atoms_coor[i][2] > lower_limit){
            bin_nox=floor((atoms_coor[i][0])/bin_width);
            bin_noy=floor((atoms_coor[i][1])/bin_width);
            if(bin_nox < binsx && bin_noy < binsy){
                den[bin_nox][bin_noy] += 1.0;
            }
        }
    }

    //////////////////////////////////////
        atoms_coor[atoms][3]={0};
        l=0;
        i=0;
        first=first+(lpf);
        last=last+(lpf);
        s+=1;
    }
    count++;
}
inFile.close();
////////////////////////////////////
    binning(binsx, binsy, bin_width, rho, atoms, frames);
////////////////////////////////////
////////////////////////////////////
    tend = time(0);
    cout << "It took " << difftime(tend, tstart) << " second(s)." << endl;
    return 0;
}

```

Appendix D: Mean Square Displacement Plots

In this section, we present the mean square displacement plots and the fitted straight lines used to calculate the 3-D diffusion coefficient of water molecules in different volumes at different distances from the surface of both systems: the undoped tobermorite 14Å and the 5% Na-doped tobermorite 14Å, which are shown in **Figure 16** and **Figure 17**, respectively. These plots represent the 1st 4 ns simulations only (with trajectories for only the last 3 ns are recorded). The same calculations are repeated for the remaining simulations, and the diffusion coefficients are averaged over all values for the corresponding water volume. Following the same mentioned procedure, the diffusion coefficients of Na⁺ and Cl⁻ ions are calculated.

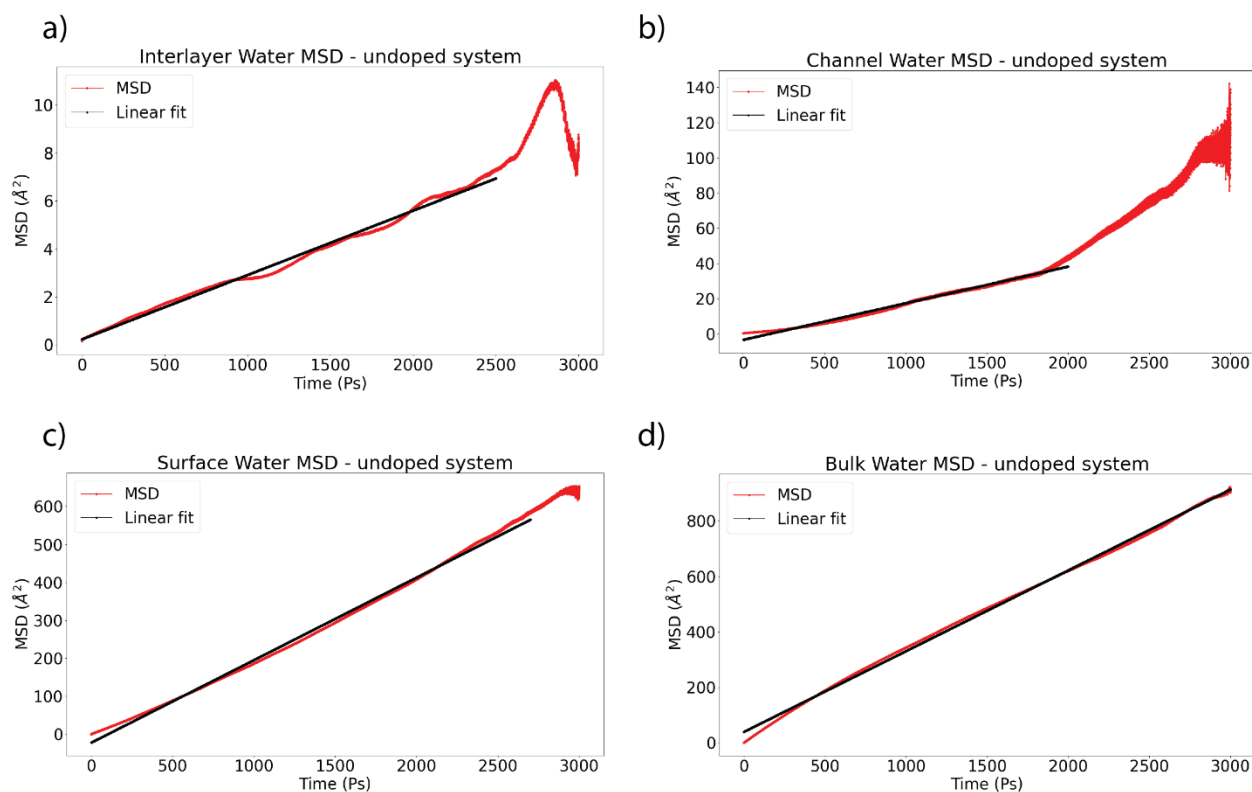


Figure 16. (a), (b), (c), and (d) represent the mean square displacement plots (red curves) for the interlayer water, channel water, surface water, and bulk water layers, respectively. These results are for the undoped tobermorite pore system, specifically, the 1st 4 ns production simulation, where trajectories are recorded only for the last 3 ns. Shown also straight fitted black lines used to calculate the diffusion coefficient from the Einstein equation.

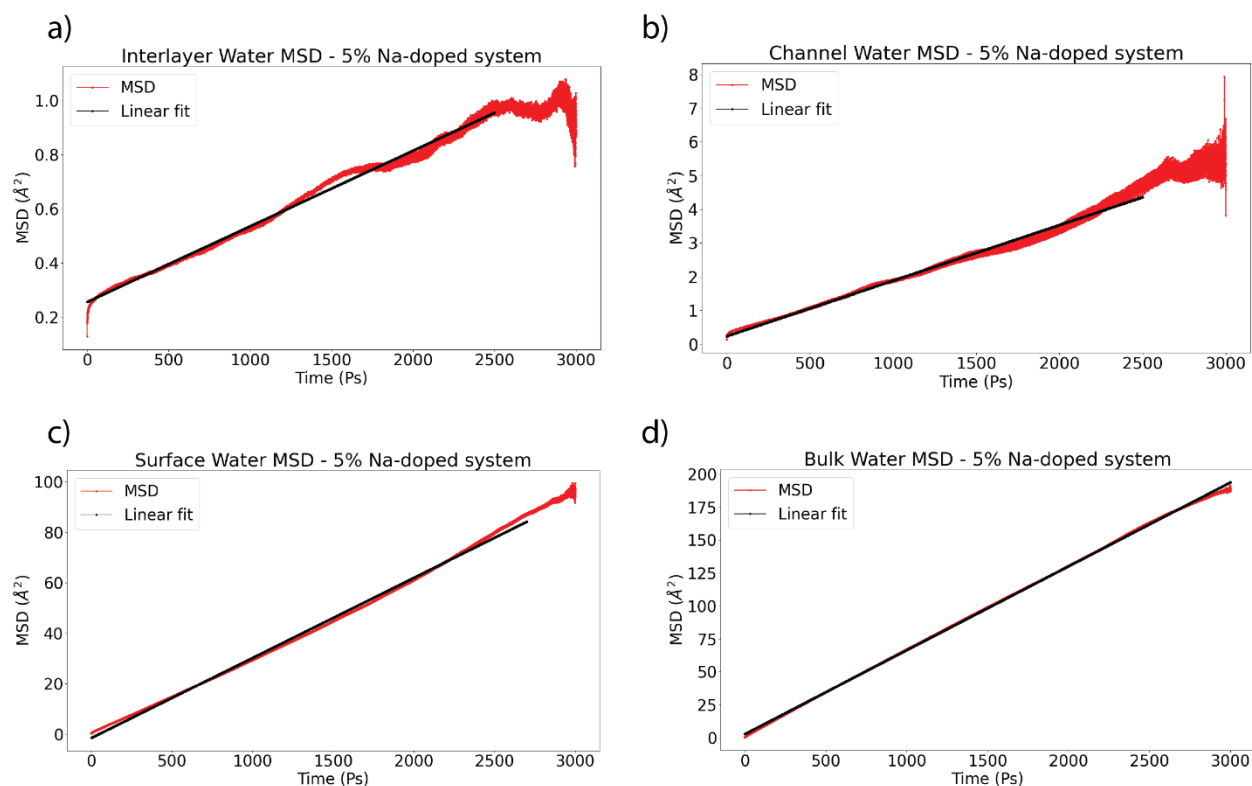


Figure 17. (a), (b), (c), and (d) represent the mean square displacement plots (red curves) for the interlayer water, channel water, surface water, and bulk water layers, respectively. These results are for the 5% Na-doped tobermorite pore system, specifically, the 1st 4 ns production simulation, where trajectories are recorded only for the last 3 ns. Shown also straight fitted black lines used to calculate the diffusion coefficient from the Einstein equation.